Università degli Studi di Padova
Dipartimento di Fisica "G. Galilei"

Scuola di Dottorato di Ricerca in Fisica
XXIII ciclo

Local doping of lithium niobate by iron diffusion: a study of photorefractive properties

Direttore della Scuola: Ch.mo Prof. Attilio Stella

Supervisore: Dr.ssa Cinzia Sada

Dottoranda: Dr.ssa Annamaria Zaltron

Contents

Introduction

In the last decades the electronic data transmission technology has progressively reached its performance limits and it is nowadays evident that further advances can be achieved only by all-optical signal processing systems, since they could allow to obtain devices working at higher speed, with low optical power and more compact sizes. Therefore, the research in nonlinear optics have been rapidly expanding in the last twenty years, developing many applications of photonics which are now relevant for industrial and consumer markets. In particular, in electo-optic materials the phenomena based on the photorefractive effect are doubtless playing a major role in the building up of optoelectronic signal transmission and processing devices. The photorefractive effect consists in the change of the refractive index of a material under inhomogeneous illumination, as a consequence of the charge distribution between darker and brighter regions that gives rise to a local space-charge electric field, which in turn modulates the refractive index of the crystal via the electrooptic effect. At the beginning of its study, about 45 years ago, the photorefractive effect was considered detrimental and for this reason named as "optical damage", but soon after its potential for optical device was recognized and it was proposed for applications in holographic data storage technology, with huge storage capability.

Among the photorefractive material lithium niobate ($LiNbO_3$, LN) receives special attentions thanks to its excellent electro-optical and nonlinear optical properties, which make it a promising material for applications in photorefractive optical devices. Although the photorefractive effect already occurs in $LiNbO_3$ pure crystals, it is well known that by doping the material with transition metals its photorefractive properties are significatively enhanced[1, 2]. In particular, for photorefractive applications the most diffused dopant of lithium niobate is iron, which in this material can exists in two possible valence states, Fe^{2+} and Fe^{3+}, acting respectively as donors and acceptor of free charge carriers. The iron doping of $LiNbO_3$ therefore allows to enhance the photorefractive properties, leading to a creation of holographic gratings with an induced refractive index change which is an order of magnitude larger than those obtained in undoped crystals: for this reason this material is currently under intense investigation for applications such as narrow-band interference filters, wavelength demultiplexer and holographic data storage, stimulating basic research in solid-state physics. Moreover, lithium niobate offers incredible versatility as substrate for integrated optics, allowing to realize on the same crystal optical elements with different functions, by exploiting various microstructural technologies. In this way it is possible to create on a single lithium niobate crystal an all-optical system, where they are present both stages to properly process an optical signal and all the necessary waveguides to transmit the signal from an optical component to another one of the device. This kind of devices requires the capability to locally modify the physical and structural properties of the lithium niobate substrate, by doping several regions of the same matrix with different dopant concentrations and, sometime, also with different elements, according to the special functions of each optical stage. In particular, a lithium niobate integrated optical circuit with a photorefractive stage requires to perform an iron local doping, in order to improve the photorefractive properties of the substrate only in the desired limited area. A good candidate to fulfill the mentioned requirements is the thermal diffusion process by thin films, which, if combined with a standard masking technique[3, 4], allows to realize iron local doping with reasonably accuracy. However, in spite of the potential of this doping technique, only few works are devoted to the study of Fe-diffused $LiNbO_3$ crystals and, in any case, the are performed in a channel waveguide configuration[5], obtaining values of photorefractive parameters which are averaged over the depth of the waveguiding layer. Thus, even if bulk Fe:LN samples grown by Czochralski technique have been widely investigated[1, 2], a detailed and depth-resolved study of the photorefractive properties of iron diffused layer in lithium niobate is still lacking. Indeed, bulk samples have the advantage that they can be easily characterized by mean of optical techniques, since the dopant concentration is the same over the entire volume of the crystal and, therefore, there are not strong restrictions on the size of the incident beam or on the area of the sample where realize the measurements. On the contrary, the diffused samples present an in-depth dopant concentration profile, thus also their photorefractive properties have an in-depth dependence and, to be correctly characterized, they require depth-resolved investigations. Moreover, since the thermal diffusion is a non-equilibrium process where the dopant has to find a place in an already establish crystalline structure, it is not obvious that the resulting iron doped layer presents the same physical properties of the bulk Fe:$LiNbO_3$ samples, where, on the contrary, the iron atoms accommodates in the lithium niobate crystal at the melting temperature, assuming the most stable configuration during the growth of the crystal. Therefore,a local characterization of the photorefractive properties of the diffused layer appears mandatory, in order to be able in the future to exploit the thermal diffusion as doping process to create the desired photorefractive stage on an optical integrated device.

This work is mainly focused on both the structural characterization of the prepared doped crystals and the investigation of photorefractive properties of Fe-diffused lithium niobate crystals and a new optical set-up is presented, which is able for the first time to realize in-depth characterizations of the photorefractive effect along the iron concentration profile. This innovative optical characterization technique allows to investigate only a limited area of the doped layer, thus relating at each depth the corresponding iron concentration with the photorefractive response of the material. In this way it is possible to realize in depth-profiles of the main physical photorefractive parameters (such as the photoconductivity, the refractive index change and so on), which are also useful to achieve a better understanding of the thermal annealing processes used to realized the investigated samples, giving the possibility to investigate physical mechanisms never studied before.

After a brief presentation of the main physical properties of lithium niobate (chapter 1), in the second chapter the experimental techniques used to prepare and characterize Fe-diffused $LiNbO_3$ samples are described and discussed. In chapter 3 it is discussed the structural evolution of the doped layer during the thermal diffusion of iron into the lithium niobate substrate. Moreover, by means of Proton-Induced X-ray Emission (PIXE), Rutherford Backscattering Spectrometry (RBS), Nuclear Reaction Analysis (NRA), micro Raman spectroscopy and polaron luminescence, it is investigated the final iron lattice site inside the host matrix, discussing as its location affects the native defect structure of the material. Then the High-Resolution X-Rays Diffraction (HRXRD) technique is exploited to study the effect of iron incorporation on the surface structural properties of the material, taking into account also the influence of the dopant valence state. Chapter 4 begins with a theoretical introduction to the photorefractive effect, with major attention to the band transport model with one photorefractive center, then the new optical set-up mentioned above is described, discussing in details its experimental and computational characterization. Finally, in chapter 5 all the holographic measurements performed on nominally pure and iron doped lithium niobate crystals are shown and discussed, revealing new insights on the reduction mechanism of these iron diffused samples.

In this work the author has personally dealt with: the development and the building up of the above mentioned new optical set-up, as well as all the holographic measurements with relative analysis and the preparation and characterization, by means of UV and IR Optical Absorption technique, of the investigated samples; all the measurements and relative data analysis concerning the HR-XRD technique; the RBS, NRA and PIXE acquisition data and subsequent analysis, in collaboration with dr. N. Argiolas and dr. D. De Salvador. The micro raman and polaron luminescence have been performed by dr.ssa S. Mignoni and prof. M.Fontana, while all the Secondary Ions Mass Spectrometry (SIMS) measurements present in this work and the Optical Absorption ones discussed in chapter 3 have been realized by dr.ssa M.V Ciampolillo.

The work here presented was firstly supported by a project financed by the University of Padova (Progetto di Ateneo, 2009-2010) and is actually a part of a PRIN project financed by Italian Minister of University and Research (MIUR) (2010-2012).

Chapter 1

Lithium niobate

In this chapter the main properties of lithium niobate are described, which are necessary to achieve better understandings of the structural and optical investigations presented in the following chapters.

1.1 Chemical composition

Lithium niobate crystals can not be found in nature and they were synthesized for the first time in 1928 by Zachariasen and, in the sixties, widely investigated at Bell Laboratories by Nassau and Abrahams. Lithium niobate ($LiNbO_3$, also labeled as LN) is one of the four compounds of the pseudobinary system Li_2O - Nb_2O_5, besides $Li_2Nb_{28}O_{71}$, Li_3NbO_4 and the lithium triniobate $LiNb_3O_8$, and it is colorless and insoluble in water and organic solvents. As seen from the phase diagram reported in fig. 1.1, $LiNbO_3$ is a material with variable composition, having a large solid solution range of about 6% at $T > 1150°C$. The liquid-solid curve reveals a maximum at a chemical composition which is characterized by a lithium deficiency, differing from the stoichiometric formula (50 mol% Li_2O): the composition corresponding to this point is defined as *congruent composition* and the relative percentage of Li_2O was found to be 48.38 mol%. At the congruent composition the melt and the growing crystal are identical with respect to the composition, so these crystals show the highest uniformity of the their chemical and physical properties. On the contrary, in other case, as the stoichiometric material, the composition of the melt and the crystal are slightly varying during the growth and the crystal becomes non-uniform, particularly along the growth axis. In this work commercial congruent $LiNbO_3$ crystals, grown by Czochralsky technique, will be investigated.

1.2 Crystallographic properties

At room temperature a $LiNbO_3$ crystal exhibits a mirror symmetry about three planes that are 60° apart and intersect forming an axis, with respect to which the material present a three-fold rotation symmetry. These symmetry operations classify the

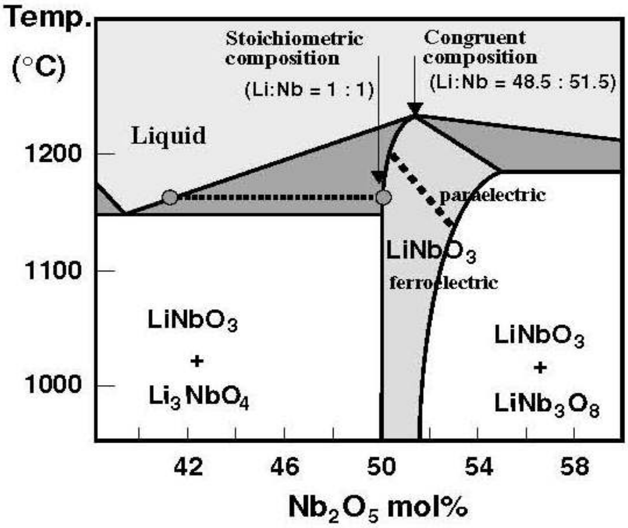

Figure 1.1: *Schematic phase diagram of* Li_2O-Nb_2O_5 *pseudobinary system.*

lithium niobate as a member of the space group *R3c*, with point group *3m*. There are three choices of axis for $LiNbO_3$, namely rhombohedral, hexagonal and orthohexagonal cells: the former two are convenient for crystallographic aim and structural investigations, but for most applications the orthohexagonal setting is preferred and the tensor components of the material properties are usually given with respect to its x, y and z axes, which are all orthogonal. Concerning the hexagonal unit cell, the c axis, which corresponds to the z-axis of the orthohexagonal cell, is defined as that one about which the crystal exhibits three-fold rotation symmetry and its positive end points toward the crystal face where a positive charge appears on cooling the material. Moreover the three equivalent axes of the conventional hexagonal cell (a_1, a_2 and a_3) are 120° apart, lie in a plane normal to the c axis and are chosen to be perpendicular to the three mirror planes of symmetry.

The lithium niobate structure at temperatures below its ferroelectric Curie temperature ($T_c \simeq 1140$°C) consists of planar sheets of oxygen atoms in a slightly distorted hexagonal close-packed configuration. The octahedral interstices formed by this oxygen structure are one-third filled by lithium atoms, one-third by niobium and one-third is vacant, following, along the c axis, the order Li-Nb-vacancy. In the paraelectric phase, above the Curie temperature, the lithium atoms lie in oxygen planes, while niobium ions are located at the center of oxygen octahedrals (see fig. 1.2), making this phase non-polar. On the contrary, as the temperature decreases below T_c lithium and niobium atoms are forced into new positions: the Li ions are shift with respect to the O planes by about 44 pm, and the Nb ions by 27 pm from the center of the octahedra. These shifts cause the arising of a spontaneous polarization, thus $LiNbO_3$ belongs to the class of the displacement ferroelectric materials.

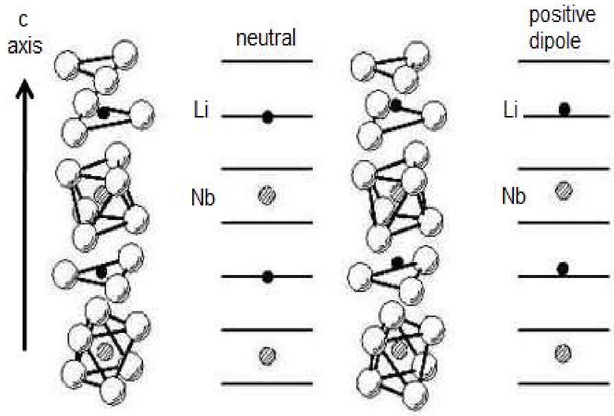

Figure 1.2: *Position of Li and Nb atoms with respect to the O planes in the paraelectric (left) and ferroelectric (right) phase.*

1.3 Some physical properties

1.3.1 Pyroelectric effect

Lithium niobate is a pyroelectric solid which exhibits a change in the spontaneous polarization as a function of the temperature. The relation between the change in temperature, ΔT, and the change in the spontaneous polarization, ΔP, is linear and can be written as $\Delta P = \hat{p}\,\Delta T$, where $\hat{p}$ is the pyroelectric tensor. In lithium niobate this effect is due to the movement of Li and Nb ions relative to the oxygen planes and, since they move only in the direction parallel to the c-axis, the pyroelectric tensor has the form

$$p = \begin{bmatrix} 0 \\ 0 \\ p_3 \end{bmatrix} \tag{1.1}$$

where $p_3 = \text{-}4\,\text{x}\,10^{-5}$ C/m^{2}K [6] and the negative sign indicates that upon cooling the +c crystal face will become positively charge, as previously mentioned.

1.3.2 Permittivity and refractive indices

The relationship between the electric displacement **D** and the electric field **E** is linear and can be written as $\mathbf{D} = \hat{\epsilon}\,\mathbf{E}$, where $\hat{\epsilon}$ is the second-rank permittivity tensor. Due to the crystallographic structure and the symmetry properties of lithium niobate, its permittivity tensor, in the orthohexagonal cell, can be represented by a 3 x 3 matrix with the form

$$\hat{\epsilon} = \begin{pmatrix} \epsilon_{11} & 0 & 0 \\ 0 & \epsilon_{11} & 0 \\ 0 & 0 & \epsilon_{33} \end{pmatrix} \tag{1.2}$$

where it is possible to notice that only the diagonal elements are not-zero and that the permittivity has the same value for any electric direction perpendicular to the c-axis. Permittivity is often given in terms of the permittivity of the vacuum (ϵ_0), obtaining the so called relative permittivity or dielectric constant (ϵ^r), whose values are reported in table 1.1.
At optical frequencies the permittivity of a material is usually described in terms of its refractive index. In particular the lithium niobate presents two refractive indices, an extraordinary one (n_e) and an ordinary one (n_o), which refer respectively to the z axis and to the x and y axes of the crystal. The dependence of the refractive indices on the temperature, the light wavelength and the composition of the material is taken into account in the relation proposed by Schlarb and Betzeler in their paper[7], where the Sellmeier equations are further generalized. In particular the Schlarb's approach is valid not only for pure $LiNbO_3$ crystals, but also in the case of doping with optical-damage-resistant ions, allowing to exploit the refractive indices as a sensitive method to determine the composition of the material.

1.3.3 The electro-optic effect

As other electro-optic crystals, also the lithium niobate exhibits a change of the its refractive indices if subjected to an electric field, a phenomenon which is named *electro-optic effect.* Usually this effect is discussed in terms of the optical indicatrix, an ellipsoidal surface whose major and minor axes of the central section normal to the light propagation direction represent the principal refractive indices of the material. The behavior of the indicatrix can be represented as a power series of the electric field E

$$\Delta\left(\frac{1}{n^2}\right)_{ij} = \sum_k r_{ijk}E_k + \sum_{k,l} s_{ijkl}E_k\,E_l + ... \tag{1.3}$$

where r_{ijk} and s_{ijkl} are the coefficients relative to the linear and quadratic electro-optic effects, usually named respectively *Pockel effect* and *Kerr effect.* Although lithium niobate presents high linear electro-optic effect, higher-order terms can be neglected, because in this material no quadratic electrooptical effect can be significatively observed for applied electric fields up to 65kV/mm[8]. Due to the symmetry of the lithium niobate, its linear electro-optic tensor $\hat{r}$ results

$$\hat{r} = \begin{bmatrix} 0 & -r_{22} & r_{13} \\ 0 & r_{22} & r_{13} \\ 0 & 0 & r_{33} \\ 0 & r_{42} & 0 \\ r_{42} & 0 & 0 \\ -r_{22} & 0 & 0 \end{bmatrix} \tag{1.4}$$

Thus, the electro-optic effect in $LiNbO_3$ can be described by only four independent

a_{Hex}(Å) c_{Hex}(Å)	5.1489 [9, 10] 13.8631
$\epsilon^r_{11}, \epsilon^r_{33}$	84.1, 28.1 [9]
$r_{13}, r_{22}, r_{33}, r_{51}$ (x 10^{-12} m/V)	8.6, 3.4, 30.8, 28.0 [11]
n_e, n_0	2.23, 2.31 [12]

Table 1.1: *Main properties of congruent lithium niobate. The values are relative to the wavelength of 532 nm.*

coefficients, whose values are reported in table 1.1. In particular for an electric field aligned along the optical axis of the material, that is the z one, the change in the refraction index is provided by the following relation

$$\Delta n_{o,e} = -\frac{1}{2} n_{o,e}^3 \, r_{13,33} \, E_z \qquad (1.5)$$

Moreover, as it will be better described in chapter 4, the electro-optic effect plays a key role in the formation of refractive index grating.

1.3.4 The photorefractive effect

The electro-optic materials exhibit an interesting phenomenon, known as *photorefractive effect*, which consists in a light-induced modification of the refractive index of the material. As it is commonly known, this effect was originally considered undesirable, and for this reason named *optical damage*, because the change of the refractive index under illumination limited the usefulness of such crystals, giving rise to decollimation and scattering of laser beams in devices such as modulators and frequency doublers. Subsequently the capability of such effect was recognized and the $LiNbO_3$ started to be widely investigated for holographic data storage, interference filters, image processing applications and so on. Briefly, a non-homogeneous illumination of the material causes a charge redistribution between dark and bright regions and, as a consequence, a local electric field builds up, modulating the refractive index of the crystal by means of the electro-optic effect mentioned above. This effect can be significatively enhanced by doping the material with dopants which act as photorefractive centers, such as the iron, that with its two possible valence states (Fe^{2+} and Fe^{3+}) can behave as donor and acceptor for the free charge carriers. Since the photorefractive effect in Fe:$LiNbO_3$ crystals is the main subject of study of this work, it will be widely discussed in the fourth chapter, where also the role of intrinsic defects will be deeply explained.

1.4 Defects structure of congruent lithium niobate

Since the first studies of the photorefractive effect in $LiNbO_3$, a great effort have gone into the understanding of the role of defects in the physical properties of the material, above all in the photorefractive ones. Therefore, in this section an overview on intrinsic and extrinsic defects in lithium niobate is given, focusing the attention on the congruent $LiNbO_3$.

Before proceeding with the discussion on the defect structure of $LiNbO_3$, it has to recall the polaron concept. The *polaron* is the coupling of photoinduced electrons with the host ions of the material and can be distinguished between *small* and *large polaron*: in the former case the disturbed host region of the crystal exceeds significantly the lattice constant, whereas in the latter case the polaron radius is within a single lattice site, due to the higher coupling between the charge carrier and the host phonon. The transport of large polarons may be regarded as a band movement of free electrons with an effective mass, whereas the movement of a small polaron occurs by hopping. Moreover, as it will be discussed in the following, if the material contains defects, the polaron energy is decreased and polarons localize at defect sites, forming the bound small polaron.

1.4.1 Intrinsic defects and absorption spectrum of pure crystals.

As already mentioned, the most employed composition of lithium niobate is the congruent one, which is characterized by a Li fraction $x = [Li]/([Li]+[Nb]) = 0.484$, corresponding to about 6% empty Li sites in the lattice. Charge compensation for such deficiency can be described by several possible processes of Li_2O outdiffusion

$$(LiNbO_3) \rightarrow Li_2O + 2V_{Li} + V_O \tag{1.6}$$

$$(LiNbO_3) \rightarrow 3Li_2O + 4V_{Li} + Nb_{Li} \tag{1.7}$$

$$(LiNbO_3) \rightarrow 3Li_2O + 4V_{Nb} + 5Nb_{Li} \tag{1.8}$$

which are respectively known as *Oxygen vacancy model*, *Lithium vacancy model* and *Niobium vacancy model.* The eq. 1.6 assumes that the lithium vacancies are compensated by oxygen vacancies, as it usually occurs in the oxides perovskites. On the contrary the eq. 1.7 implies that some V_{Li} are filled by Nb ions, forming the so called *niobium antisites* Nb_{Li}, whereas the eq. 1.8 states that *all* the lithium vacancy are filled with niobium antisites, leading to the formation of niobium vacancy, V_{Nb}. However, density measurements[13] have rather early discarded the first model, because they have showed an increase in the density of $LiNbO_3$ with decreasing Li_2O content, which is inconsistent with the oxygen vacancy model, whereas it can be justified by assuming the presence of niobium antisites. Evidently the formation of Nb_{Li} costs less energy than that of V_O and, therefore, only the two latter compensation mechanisms (shown in fig.1.3) can be taken into account. Several measurements have been performed to clarify which model is the correct one, but they have been found results

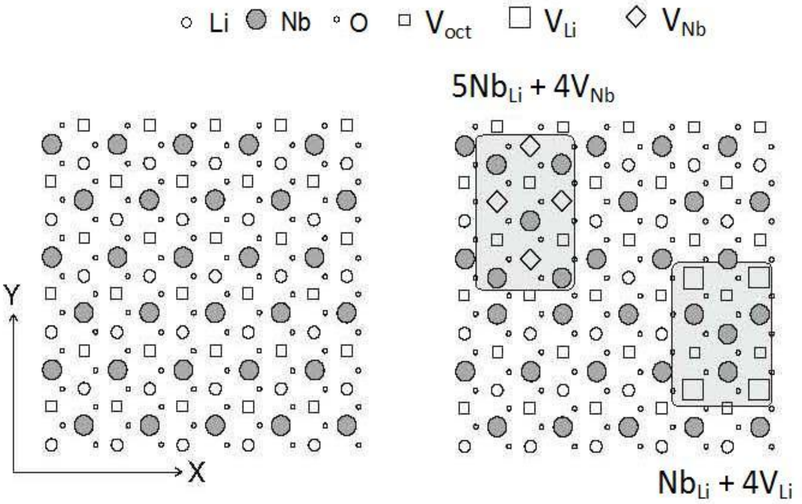

Figure 1.3: *Projections onto the plane (001) of the ideal lithium niobate structure (left) and of the two defect structures with Li and Nb vacancies (right).*

in support of both the proposed processes and the controversy remains. Moreover, recently Abdi et al.[14] have proposed a further model based upon the coexistence of both Nb and Li vacancies, whose amounts were calculated as a function of crystal composition. In any case, regardless to the model considered, the cornerstone of the lithium niobate defect structure is the existence of niobium antisites, which plays a key role in the optical and photorefractive properties of the material, as it will be discussed in the following and in chapter 4.

Among the defects present in the lithium niobate structure only the Nb_{Li} has been identified definitely, using Electron Paramagnetic Resonance (EPR) technique and related studies. In the ground state of a congruent crystal, Nb_{Li} is present in the diamagnetic charge state Nb_{Li}^{5+} ($4\mathrm{d}^0$), but after a two-photons or X-ray irradiation or the reduction and subsequent illumination of the crystal the paramagnetic configuration, Nb_{Li}^{4+} ($4\mathrm{d}^1$), can be observed. Thanks to optical absorption measurements, it has been possible to achieve a better understanding of role of Nb_{Li} in the lithium niobate crystals, developing also the polaron model. Indeed, although LiNbO_3 is transparent between about 320 - 5000 nm, if a reduced crystal is illuminated two absorption bands at 2.5 eV (496 nm) and 1.6 eV (762 nmn) are observed, whose presence can be explained by considering the reduction mechanism proposed by Donnerberg et al[15] for congruent composition and Nb_{Li} structure

$$1LiNbO_3 + 2V_{Li} \rightarrow \frac{3}{2}O_2 + Li_{Li} + Nb_{Li}^{4+} + 6e^- \tag{1.9}$$

According to this model three oxygen atoms evaporate form the surface of the crystal, leaving back the cations Li^+ and Nb^{5+}, which recombine with the two V_{Li} creating an additional Nb_{Li} defect, and six electrons, which can be trapped by the Nb ions.

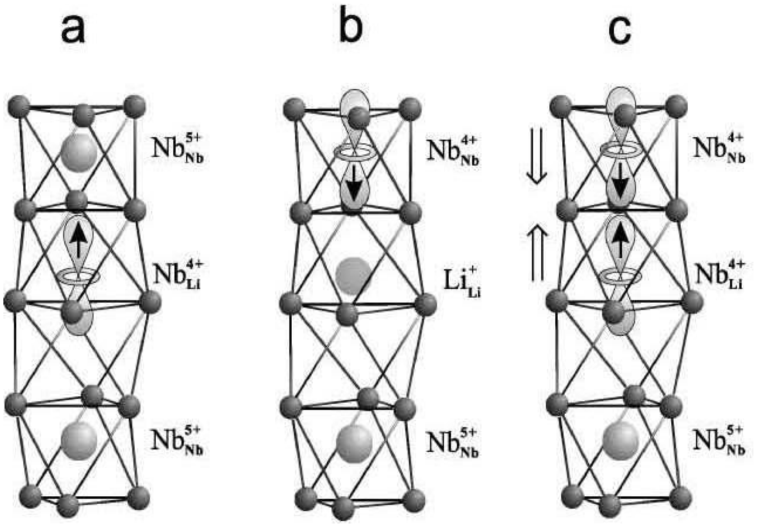

Figure 1.4: *Schematic representation of the bound polaron (a), of the free polaron (b) and the bipolaron (c).*

However, even if the bound small polarons Nb^{4+}_{Li} are responsible for the wide absorption band peaked at 1.6 eV, they can not explain all the features of the absorption spectra of the material. Indeed, the reduced crystal is diamagnetic, so the absorption band at 2.5 eV can not be assigned to an electron capture by Nb_{Li} forming the paramagnetic state Nb^{4+}_{Li}. Schirmer et al., on the basis of various evidences[16], assigned the mentioned absorption band to a *bipolaron*, a diamagnetic electron pair bound state where two electrons with antiparallel spins are capture by two neighboring Nb ions, one replacing V_{Li} and the other in the regular lattice site, forming the complex Nb^{4+}_{Li} - Nb^{4+}_{Nb}, as illustrated in fig.1.4. Taking into account the high density[1] of Nb_{Li} in congruent $LiNbO_3$, there are many such preformed pairs of Nb_{Li} and Nb_{Nb}, which capture the electrons with an higher probability than an isolated niobium antisite, since the formation of a bipolaron is energetically favorable with respect to the small polaron. Hence the broad band present in the absorption spectrum at 2.5 eV is attributed to the optical dissociation of the bipolaron and the electron ionized from Nb^{4+}_{Nb} is rapidly trapped at a further empty Nb_{Li} defect. Finally, the bipolaron dissociation is metastable at room temperature, but already at 200K the thermal dissociation of bipolarons occurs, with the consequent formation of isolated polarons. The change in the relative concentrations of bipolarons and polarons leads to a variation of the intensities of their corresponding absorption bands: with increasing temperature the 2.5 eV band decreases, whereas 1.6 eV one increases, and from their temperature dependence the bipolaron dissociation energy has been determined to be about 0.3 eV.

---

[1] The density of niobium antisite in congruent lithium niobate is about 1% of the Li sites, that means that there is about one Nb_{Li} defect in each fiftieth unit cell.

1.4.2 Extrinsic defects

As it is well known, lithium niobate can be properly doped to modify its physical properties, above all the protorefractive ones. Concerning the photrefractive effect, the dopants usually employed can be divided into two categories: on the one hand the materials which increase the resistance to the optical damage, as Mg, Zr, Zn and Hf, on the other on the dopants which enhance the photorefractive properties of the crystal, among which Fe is the most widely used. In particular in this work diffused Fe:$LiNbO_3$ crystals are investigated, so in the following chapters all the optical, structural and photorefractive properties of this system will be widely discussed throughout the thesis. On the contrary in the following the attention will be focused on the most common extrinsic defect of lithium niobate: the hydrogen.

As the defect treated before, also Hydrogen plays an important role in the photorefractive process in $LiNbO_3$, affecting mainly the decay of an holographic grating in the dark[2]. It is widely accepted that hydrogen enters the lithium niobate lattice from the ambient atmosphere during or after the growth process, reaching in as-grown crystals concentrations of about 10^{18} - 10^{19} cm^{-3}. Usually hydrogen is bonded to an oxygen ion and performs a vibration, referred to as OH^- stretch mode, with an energy between 3200 and 3700 cm^{-1}. Besides basic studies of the spectroscopic properties of the OH^- stretch mode, it has served very often as a tool to investigate properties of the host matrix, due to its easy observation by absorption spectroscopy, which allows to obtain a qualitative estimation of its content in the material. In congruent lithium niobate, the OH^- ions presents a strong absorption peak at 3.482 cm^{-1} (2.87 μm) and a weaker one at 3.467 cm^{-1} (2.88 μm) and from Raman scattering measurements it was derived that the hydrogen stretching vibration occurs in the plane perpendicular to the polar c-axis[17]. Moreover it was found that both the shape and the position of the IR absorption band noticeably depend on the [Li]/[Nb] ratio: with increasing Li content the peak position is slightly shifted at higher wavelength and the band width appears narrower, due to the disappearance of intrinsic defects which leads to a more homogeneous environment. Finally, the hydrogen content can be tuned by performing properly thermal treatments. To increase the amount of hydrogen the lithium niobate crystal can be annealed at temperatures between 400-700°C in a water-vapour-rich atmosphere[17]. On the contrary a dehydration of the material can be achieved by vacuum annealing the crystal at temperature of about 400°C[18].

---

[2] For further details see section 4.3.2

Chapter 2

Samples preparation and characterization techniques

This chapter is devoted to the presentation of the experimental procedures used to prepare and characterize Fe in-diffused samples.
In the first part of the chapter they are presented the main steps involved in the preparation of a diffused Fe:LN sample, then the usual techniques exploited to characterize the compositional and structural properties of each realized sample are briefly discussed. Finally they are summarized the best experimental conditions to realize good-quality diffused Fe:LN crystals.

2.1 Fe-diffused lithium niobate samples preparation

In this first section they are briefly discussed the experimental techniques used to realize the diffused iron doped lithium niobate samples investigated in this work, starting from the cutting and the cleaning of the lithium niobate substrate to arrive to the diffusion of the deposited iron thin film into the substrate by means of a thermal treatment, with the final polishing of the obtained samples.

2.1.1 Sample cutting and cleaning

The first stage of the samples preparation is the cutting of the substrates. The undoped lithium niobate samples are obtained by a commercial x-cut wafer, with congruent composition, thick 1mm and polished on both faces. A South Bay 540 cutting machine, equipped with a diamond-coated Cu-alloy blade, is used to cut the wafer, whose crystallographic axes can be aligned with respect to the blade by using a protractor. Therefore the lithium niobate wafer is cutted along its $\hat{y}$ and $\hat{z}$ directions and, according to their experimental purpose, substrates with different dimension can be obtained. After the cutting, just before the beginning of the deposition process, each sample is treated with a hydrofluoric acid, then immersed in acetone in an ultrasonic cleaner for about ten minutes and finally cleaned with the propanol, in order to completely remove all the residual wax previously used to fix the wafer to its support on the cutting machine.

2.1.2 Iron thin film deposition

In this work, to realize iron thin film on lithium niobate substrate it is exploited the magnetron sputtering technique, which is one of the most widely used surface coating technique. Sputtering is basically the removal of atoms from a solid material by bombardment of its surface with energetic particles. The process occurs in a vacuum chamber, where the substrate and the target are located and, once the appropriate pressure is reached, and inert gas is introduced. When a negative voltage is applied to the target, it attracts the positive ions of the gas which collide with the surface atoms of the material, leading to an energy transfer which results with the sputtering of some atoms. Then the sputtered neutral atoms tend to deposit on all the surfaces present in the chamber, therefore also on the considered substrate. Besides from the sputtering of a target atom, another important phenomenon involved in this process is the emission of secondary electrons from the target surface. If permanent magnets are positioned under the target, the secondary electrons are trapped around the magnetic field lines undergoing more ionizing collisions with neutral gas than would otherwise occur. This enhances the ionization of the inert gas near the target leading to a higher sputter rate.

The sputtering machined used was provided by Thin Film Technology and it is equipped with two sources: a DC (diode) magnetron for metallic targets and a RF (radio frequency) magnetron for semiconducting ones. In the cylindrical chamber the vacuum is achieved by using two pumps: first a rotary vane vacuum pump is activated to reach a pressure of about $9\text{-}10 \cdot 10^{-2}$ mbar, then a turbomolecular one is switch on to obtain and maintain a pressure less than $3 \cdot 10^{-6}$ mbar. The usual DC magnetron sputtering configuration is not suitable for ferromagnetic targets, because they affect the magnetic field created by permanent magnets, preventing the plasma confinement. Therefore, to realize iron deposition an adjustment of the sputtering machine was necessary. However, it was chosen not to modify the magnetron configuration of the source, but to change the geometry of the target itself. Indeed, by reducing the thickness of the target, adapting as consequence all the geometry of the source components, the magnetic field lines are able to exit from the target and to confined the secondary electrons near the material surface. Thus a 0.99 mm thick, 99.98 pure Fe target (by Testbourne) is used. The sample is mounted in a sample-holder located at about 4 cm from the iron target and during the sputtering process it is rotated, in order to achieve a good homogeneity in the thickness of the deposited film. The used inert gas is Ar and, before starting with the deposition process, a pre-sputtering of about 2 minutes is usually performed, to remove all the possible impurities present on the surface of the solid target. Finally, when the deposition is completed, all the pumps are stopped and, to return to the atmospheric pressure, Ar gas is still introduced in the chamber.

The process calibration was performed by dr.ssa Ciampolillo[19] and, by using the Rutherford Backscattering Spectrometry technique, the deposition rate has been evaluated to be $(4.15 \pm 0.02)\,x\,10^{14}\ atoms/s\,cm^2$. Moreover, the Atomic Force Microscopy (AFM) and the X-Ray Reflectivity results show that the iron films are smooth and flat, with a roughness less than 2 nm and a good homogeneity of the film thickness.

2.1.3 The thermal treatments

After the deposition of the iron film, the dopant is completely diffused inside the $LiNbO_3$ substrate by performing thermal treatments. The diffusion process occurs in a tubular furnace, by Gero Hochtemperatur*ö*fen Gmbh, and the heating tube consists of an uncovered FeCrAl heating coil, mounted on a ceramic fiber module whose low thermal conductivity guarantees low energy consumption and allows high heating rates, up to 600°C/h. The furnace is equipped with all the necessary to realize thermal treatments in vacuum or different gases: water-cooled flanges, gas inlet and outlet and two rotameters to adjust the gas flux at the entrance of the furnace. The rotameters scale is in Nl/h and the gases used are provided by Sapio in cylinders of 40L and purity 5.0. At the center of the tubular furnace there is a region, long some centimeters, where the highest temperature is homogeneous, thus the sample is located in that zone by using a quartz rod with at the end a square support. Moreover, between the support and the $LiNbO_3$ sample a curved alumina piece is fixed, to avoid a possible high-temperature reaction between SiO_2 and the sample, which would dissolve the crystal. Each sample is positioned on the support with the iron film upward and heating/cooling rates of 300°C/h are used, in order to avoid that the sample undergoes an excessive thermal stress.
The diffusion of iron into the substrate can occur in vacuum or in different atmospheres, which affect also the valence state of the dopant. However, for reasons that will be widely discussed at the end of this chapter, in our case the gas used during the diffusion process is oxygen, at temperature varying between 900°C and 1100°C. Moreover, since after the iron diffusion the dopant is mainly Fe^{3+}, afterwards the doped sample undergoes a further thermal treatment at a lower temperature (500°C) in a reducing atmosphere, $Ar+H_2$ or N_2+H_2.

2.1.4 Lapping and polishing

Lapping and polishing are processes by which material is precisely removed from a workpiece to produce a desired dimension, surface finish, or shape. They have been applied to a wide range of materials and applications and they are useful due to the precision and control with which material can be removed. Surface finishes in the nanometer range can be produced using these techniques, which makes lapping and polishing an attractive method for materials processing. In particular the lapping is

the removal of material to produce a smooth, flat, unpolished surface and a mid-range abrasive particle (5-20μm) is typically used, while polishing is exploited to produce a scratch-free, specular surface using fine (<3μm) abrasive particles.
The machine used to polish and lap the samples of this work is a professional one by Logitech. The machine uses a rotating disc and a device, called *JIG*, on which one or more samples are mounted and that allows to regulate the force with which the sample is pressed on the disc. The lapping process is divided into two steps and it is used to remove the subsurface damage caused by the cutting of the sample from the original commercial wafer. In these stages an iron disc is used to remove material from the surface of the sample with a rate of 10μm/min by using first an aqueous solution of 9μm alumina particles and then a 3μm one. Moreover at each step, before changing to the next one, a microscopy is used to verify if at the surface of the sample they are present only damages whose size is about the same of the alumina suspension used. Finally, in the third stage a polyurethane disc is used with a SF1 alumina colloidal suspension (0.1μm) and a polished sample is obtained with a surface rugosity less than 1μm.

2.2 Samples characterization

After the preparation procedure, the compositional and structural properties of each sample are systematically investigated by exploiting secondary Ion Mass Spectrometry, High Resolution X-ray Diffraction and Optical Absorption techniques, whose relative measurements are all performed at the Physics Department of the University of Padua. Therefore, in the following, a briefly description concerning the results obtainable on Fe-diffused LN sample by the mentioned techniques will be presented.

2.2.1 Compositional characterization)

The compositional characterization was performed by means of the Secondary Ion Mass Spectrometry, which is an analytical technique used to characterize the near surface region of the solids, by detecting the ionized secondary particles sputtered from the sample, as a consequence of the bombardment of its surface with a beam of energetic primary ions. Thus this technique is fundamental to understand as iron diffuses into the substrate, according to the temperature of the thermal treatment, the thickness of the deposited film and so on. In particular in this work SIMS is exploited to derive informations on the in-depth iron concentration profile, since its knowledge is crucial to be able to correctly comprehend the experimental results that will be discussed in sections 3.2 - 3.3 and, above all, in chapter 5.
Usually the diffusion process is described in the frame of the Fick's model, which assumes that the diffusion coefficient D is a constant and does not depend on the dopant concentrations, as well verified for diluted systems. Thanks to this assumption, with appropriate initial and boundary conditions, the Fick's second law can be

analytically solved and the relative solutions are often used also in samples whose dopant concentrations is not so low, in order to obtained a first order estimation of its distribution inside the material. This is also the case of Fe-diffused lithium niobate crystals studied in this thesis, where the source of diffusion species is finite and the dopant diffuses in the direction perpendicular to the surface, leading to the following Fick's model one-dimensional solution, which is a gaussian distribution

$$c_{Fe} = \frac{N_{Fe}}{\sqrt{\pi\, D_{Fe}\, t}}\, exp\left(-\frac{x^2}{4\, D_{Fe}\, t}\right) \tag{2.1}$$

where N$_{Fe}$ is the total amount of iron present in the dopant distribution, that is the total iron deposited by sputtering, and t is the duration of the diffusion process. Therefore, if the iron thin film is completely diffused into the substrate the dopant in-depth profile obtained by SIMS can be fitted with a gaussian function, deriving its maximum concentration at the surface of the sample and, by the HWHM ω of the curve, the diffusion coefficient

$$c_{sup} = N_{Fe}/\sqrt{\pi\, D\, t} \tag{2.2}$$
$$D_{Fe} = \frac{\omega^2}{2t} \tag{2.3}$$

Concerning iron diffusion coefficients, a wide investigation was performed and discussed in [19] on samples characterized by different amount of dopant and diffused in a O$_2$ atmosphere at different temperatures, deriving D along the $\hat{x}$ axis at the following temperatures:

$$\begin{aligned}
D_{900°C} &= (0.056 \pm 0.009) \cdot 10^{-3}\, \mu m^2\, s^{-1} \\
D_{950°C} &= (0.27 \pm 0.10) \cdot 10^{-3}\, \mu m^2\, s^{-1} \\
D_{1000°C} &= (0.51 \pm 0.07) \cdot 10^{-3}\, \mu m^2\, s^{-1} \\
D_{1050°C} &= (1.3 \pm 0.2) \cdot 10^{-3}\, \mu m^2\, s^{-1}
\end{aligned}$$

It is interesting to notice that the knowledge of the above diffusion coefficients and of the equations 2.2-2.3 allows to decide at priori which temperature and duration of the diffusion process has to be used to obtain a desired iron concentration profile and the relative surface concentration. This is the case of the samples investigated by means of holographic measurements, as reported in chapter 5. In particular those samples have been diffused at 1100°C, whose diffusion coefficient has not experimentally derived; however its value has been extrapolated by those ones relative to lower temperatures by exploiting the Arrhenius relation, deriving $D_{1100°C} = (3.2 \pm 0.1) \cdot 10^{-3}\, \mu m^2\, s^{-1}$.

Among all the interesting results pointed out by SIMS measurements on diffused Fe:LN crystals [1], in the frame of this thesis it is important to remember that ones

---

[1] For further details see [19]

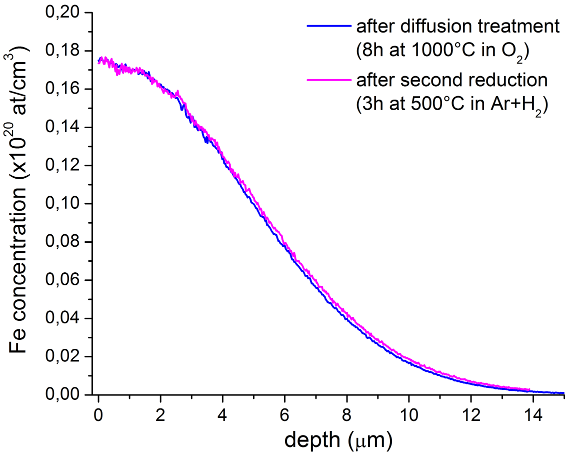

Figure 2.1: *SIMS profiles relative to the same sample after and before the reducing treatment.*

relative to the influence of the thermal reducing treatment on the iron in-depth profile. As mentioned in the previous section, after the diffusion process to incorporate the Fe atoms in the crystal, the iron valence state is changed by performing a post annealing, which consists in a reducing thermal treatment in a gas mixture of Ar+H_2 at 500°C. Thus, they have been performed SIMS measurements on the same sample before and after this further thermal treatment, in order to check the presence of possible variation in the iron distribution. The semi-gaussian iron profiles are reported in fig. 2.1: their difference is at the most 2.5%, which means that at 500°C the iron diffusion coefficient is orders of magnitude smaller that those relative to 900-1100°C, preventing the dopant to significatively diffuse further into the substrate. This result is of great interest for the realization of diffused Fe:LN photorefractive samples, because it shows as the reduction degree of the sample can be tailored at one's pleasure without varying the dopant distribution obtained previously by the diffusion process. Moreover it allows to perform a direct comparison between samples with different reduction degrees, being sure that, as it will be discussed in the following chapters, the observation of a possible change in their structural, optical and photorefractive properties can not be attributed to a different iron concentration profile, but only to its different valence state.

2.2.2 High Resolution X-Ray Diffraction

The High Resolution X-Ray Diffraction (HRXRD) technique is used to investigate the structural quality of Fe-diffused lithium niobate samples in a region closed to the surface (to few nm to about 10μm), in order to look for possible lattice deformations or crystal disorders induced by Fe incorporation. Indeed, since the thermal treatments used to realize our samples not only promote the diffusion of the iron film into the substrate, but may also produce some undesired modifications in the lithium niobate matrix itself, then a structural characterization of each sample is mandatory.

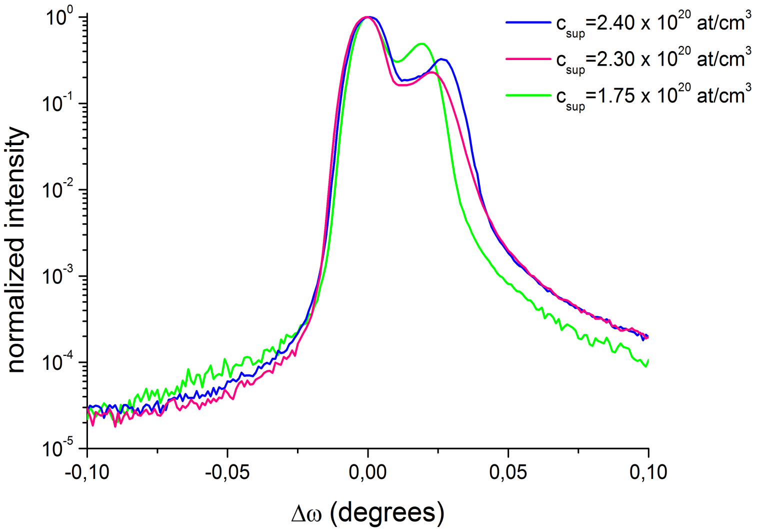

Figure 2.2: *Rocking curves relative to the lithium niobate (110) symmetrical reflection. Two peaks are evident in each angular scan: the first, at 17.41°, is relative to the substrate, the second one is due to the doped layer.*

The informations on the crystallographic structure of the sample can be derived by the shape, the intensity and the angular position of the diffraction spots present in the reciprocal space, thus for each sample two kinds of measurements are performed: the $\omega - 2\theta$ scans, called *rocking curves*, and the reciprocal space maps. The rocking curves probe the diffraction spot only in the direction perpendicular to the investigated crystallographic planes and they are generally used to obtained information on the lattice parameters of the sample; on the contrary in the reciprocal space maps a 2D section of the reciprocal space around the diffraction spot is realized and, by the distribution of the diffuse scattering, more informations can be derived concerning the lattice disorders induced by defects.

As way of example three rocking curves around the (1 1 0) symmetrical reflection, which refers to planes parallel to the surface of the sample, are reported in fig.2.2 and in each of them it is possible to notice the presence of two peaks: the peak at 17.4° is the regular lithium niobate diffraction peak, while the peak at an higher angle is related to the doped layer which, due to the iron incorporation, presents a compression of the lattice parameters along the direction perpendicular to the surface of the sample. From the angular positions of the two peaks, by exploiting the Bragg's law it is possible to derive for both the substrate and the doped layer the corresponding interplanar spacings along the investigated axis, named respectively d_x^S and d_x^L, and therefore the *relative mismatch*, defined as

$$\xi_{xx} = \frac{d_x^L - d_x^S}{d_x^S} \tag{2.4}$$

Similarly the relative mismatches ξ_{zz} and ξ_{yy} can be estimated and an analysis

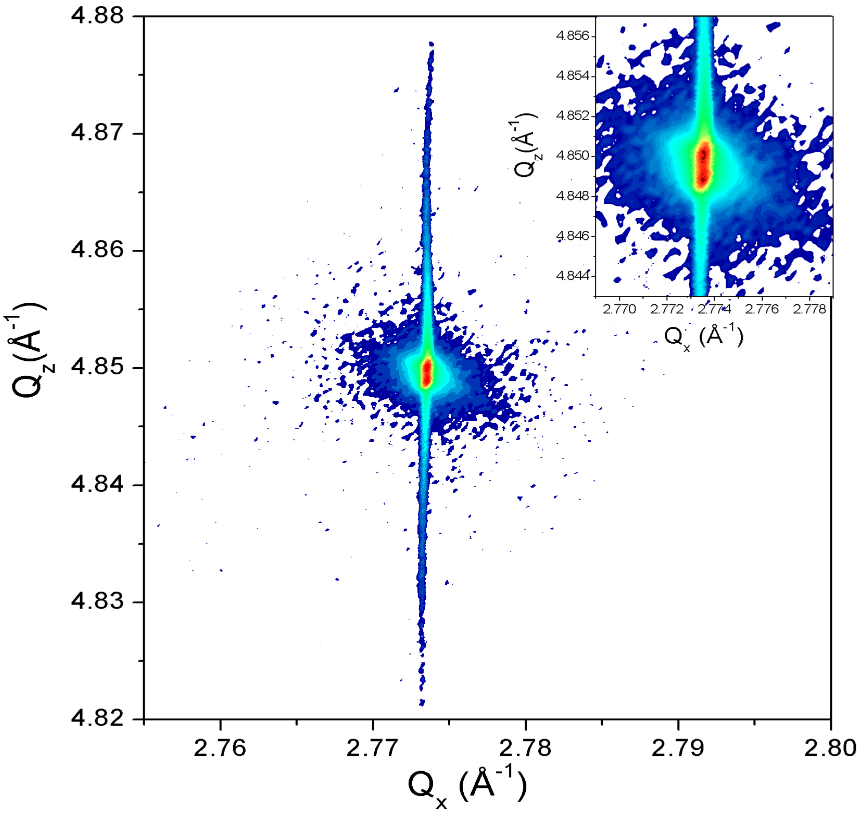

Figure 2.3: *Reciprocal space map relative to the lithium niobate (226) asymmetrical reflection. From the relative distance between the two peaks it is possible to derive the perpendicular and parallel relative mismatches.*

performed on an asymmetrical reflection has pointed out that these two contributions can be neglected if compared with the perpendicular mismatch ξ_{xx}. Indeed, if a (226) asymmetric reciprocal space map is taken into account, both the perpendicular and the parallel mismatch can be estimated, because the angular position of the "layer diffraction peak" has to satisfy at the same time the Bragg's condition for the lattice parameters along the $\hat{x}$ and $\hat{z}$, or $\hat{y}$, axis of the crystal. Thus, as way of example, in fig.2.3 the (2 2 6) asymmetrical reflection is shown and ξ_{xx} and ξ_{zz} are derived by using the following relations:

$$\xi_{xx} = \frac{q_y^S - q_y^L}{q_y^L} = (-301 \pm 1) \cdot 10^{-6} \tag{2.5}$$

$$\xi_{zz} = \frac{q_x^S - q_x^L}{q_x^L} = (-5 \pm 2) \cdot 10^{-6} \tag{2.6}$$

The parallel mismatch is less than 2% of the perpendicular one and, within the errors, almost comparable with zero. This means that the iron doped layer is pseudomorphous to the undoped substrate and that the lattice deformation induced by the dopant incorporation practically occurs only in the direction perpendicular to the surface. Moreover, since in the doped layer the deformation of the unit cell is due to the presence of iron, reasonably the measured mismatch, which is the maximum one present in the layer, is mainly due to the area where the iron concentration is maximum, that is the surface of the sample, and it is expected that this compression is larger with increasing surface iron concentration, as confirmed by the experimental rocking curves reported in fig. 2.2. Thus in the following in Fe-diffused samples the term *mismatch* will implicitly refers to the perpendicular and the maximum one present in each sample and it will be labeled as $\xi_{\perp,max}$.

2.2.3 Optical Absorption

In photorefractive applications using Fe:LiNbO$_3$, concentrations of Fe^{2+} and Fe^{3+} ions are two of the most important factors in determining the performance of the material. Indeed Fe^{2+} and Fe^{3+} ions serve respectively as source and traps of electrons and their concentrations govern the most important parameters involved in the photorefractive process, such as the photoconductivity, the photovoltaic current, the space-charge field and so on. Therefore it is fundamental to be able not only to change the concentration of the filled and empty traps, for instance by performing appropriate reducing thermal treatment, but also to estimate these parameters, and the optical absorption technique is a reliable method to achieved this aim.
Pure lithium niobate crystals are transparent in the near-IR, the visible and the near-UV region up to 3.8 eV, but when they are doped with iron new energy levels are present in the middle of the band gap, which can be involved in photon induced electronic transitions. The first characterization of the optical absorption processes in bulk Fe:LiNbO$_3$ samples was realized by Clark et al.[20] and subsequently formalized by Dischler et al.[21]. The observed optical transitions are explained by means of the crystal field theory and they are shown in fig. 2.4 and summarized in the corresponding table. The *A band* is centered at 1.1 eV (1128 nm) and it is assigned to the crystal field transition ^{5}A - ^{5}E of Fe^{2+}; the broad *D band* at about 2.6 eV (477 nm) is due to the intervalence transfer Fe^{2+} - Nb^{5+} (leading to the creation of electrons in the conduction band formed by Nb^{5+} ions); the *C band*, which begins at 3.1 eV (400 nm) and extends to higher photon energies, is related to charge transfer from oxygen π -orbitals to Fe^{3+} ions (leading to the creation of holes in the valence band formed by O^{2-} ions) and presents an apparent shift of absorption edge toward longer wavelengths when the Fe content exceeds $\approx$ 20 ppm; the two small *F bands* centered at 2.57 eV (483 nm) and 2.91 eV (426 nm) are assigned to the spin-forbidden d-d transition of Fe^{3+}. Since all these bands are polarized mainly perpendicularly to the ferroelectric axis of the lithium niobate crystal, it is preferred to work with an ordinary polarized incident light to investigate them. Moreover, while the F bands are very weak and the C one is

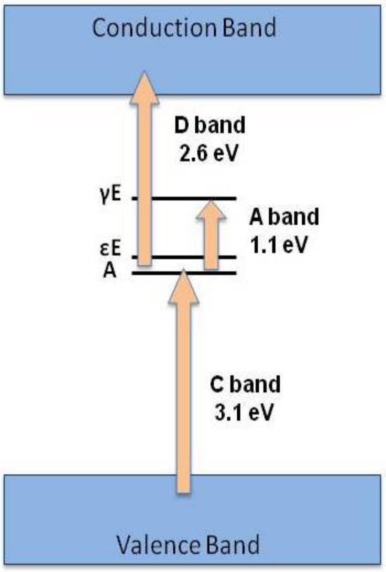

Peak (eV)	Transition
1.1	^{5}A - ^{5}E (Fe^{2+})
2.6	Fe^{2+} - Nb^{5+}
3.1	O^{2-} - Fe^{3+}
2.57 and 2.91	d-d (Fe^{3+})

Figure 2.4: *Energy levels scheme of Fe:LiNbO*$_3$*. The main optical transitions A, C and D are reported, in agreement with the nomenclature proposed by [21].*

not visible due to the overlapping with the fundamental absorption of the substrate, on the contrary the A and D bands are easily observable. It is also possible to notice that both the D band and the A one are related only to Fe^{2+}, thus they can be used to estimate the concentration of filled traps in the material. In particular, in this work the ordinary optical absorption at 532 nm, in the D band, is used to determine the Fe^{2+} absolute concentration, as proposed for bulk Fe:LN by Berben et al.[22], whose experimental results lead to the following cross section:

$$\sigma_{532nm} = (3.95 \pm 0.08) \cdot 10^{-18}\, cm^2 \tag{2.7}$$

However, to determine the reduction degree $[Fe^{2+}]/[Fe^{3+}]$ of each sample, not only the concentration of filled traps but also that of empty ones has to be known. The Fe^{3+} concentration can be obtained as difference between Fe^{2+} and Fe_{tot}, where this latter can be exactly derived by combining XRR and RBS techniques. As firstly reported by Ciampolillo et al.[23], it can be exploited the *isosbestic point* at 342 nm found in our Fe-diffused lithium niobate samples. Indeed, it has been demonstrated that at the mentioned wavelength the absorbance of the each sample is proportional only to the total iron diffused in the substrate, regardless its reduction degree, and the corresponding cross section has been derived

$$\sigma_{342nm} = (5.69 \pm 0.06) \cdot 10^{-18}\, cm^2 \tag{2.8}$$

The transmittance T_s of each sample is measured by a spectrometer in the range between 300 and 900 nm, by using ordinary polarized light. To isolate the contributions

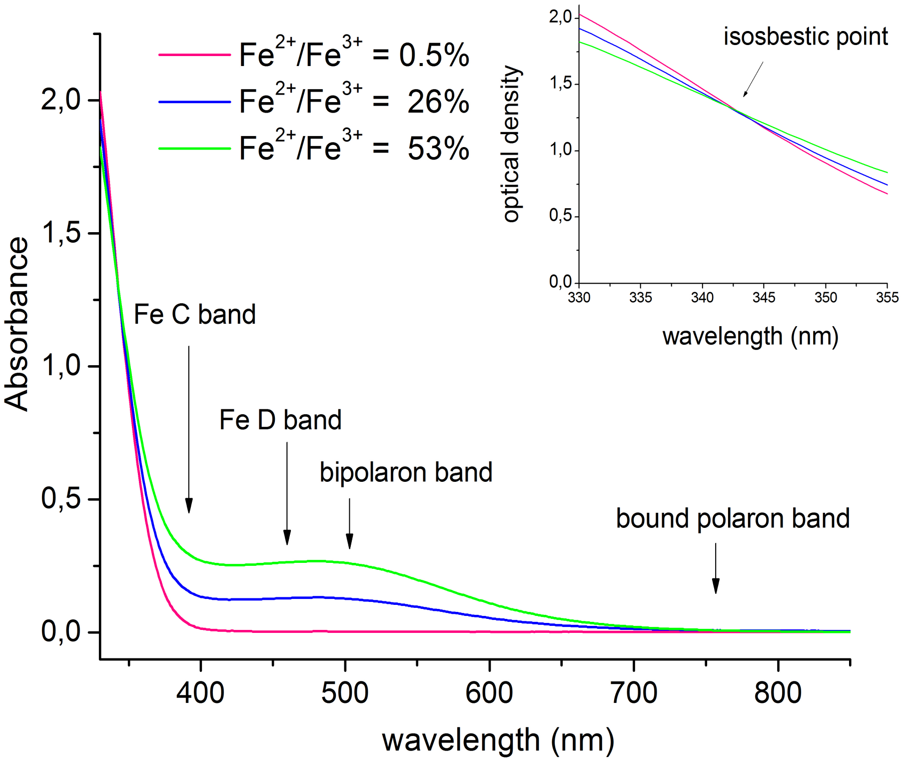

Figure 2.5: *Absorption spectra relative to diffused Fe:LN samples with the same amount of iron, but different reduction degree [Fe^{2+}]/[Fe^{3+}]. It is evident that the intensity od the D band increases with increasing Fe^{2+} content. The isosbestic point is highlighted in the inset.*

to the optical absorption deriving only from the iron present in the doped layer, T_s is normalized with the transmittance T_c relative to a pure lithium niobate crystal, obtained in the same experimental conditions. Then, from the normalized spectra, the absorbance $A = -log(\frac{T_s}{T_c})$ is calculate. As way of example in fig. 2.5 they are shown the final spectra relative to three samples with the same iron amount but different reduction degree: they are evident the above mentioned isosbestic point at 342 nm, the C band and the D one, whose intensity grows with increasing Fe^{2+} content. Moreover they are also indicated the bands relative to the bipolaron and polaron absorption processes, which partially overlap the iron D band. Thus, it is important to verify if these polaron contributions are present in the diffused Fe:LN samples to eventually correct[2] their optical absorption spectra, in order to isolate the contribution of the dopant.

Usually in bulk Fe:LN crystals the Fe^{2+} concentration is calculated as $[Fe^{2+}] = \alpha_{532}/\sigma_{532}$, where the absorption coefficient α_{532} is derived by the absorbance A at 532 nm and

---

[2] The presence of polaron or bipolaron absorption in a Fe:LN sample can be easily verified by observing the absorbance values at about 700-800 nm, since at these wavelength the presence of an absorption band can be attributed only to the polarons. If these contribution are present, the spectrum can be corrected by subtracting to it the absorbance of an undoped reduced pure LN crystal, multiplied by a convenient constant, so that the final spectrum does not present an absorption band at 700-800 nm and the isosbestic point is still at 342 nm.

the thickness d of the crystal by using $\alpha = \mathrm{A/d}$. On the contrary, since in Fe-diffused samples the absorption species is not homogeneously distributed over a well defined thickness, the above analysis can not be performed and the absorbance itself is used to estimate the total reduction degree of each investigated sample. The Fe^{2+} and Fe^{tot} fluences are given respectively by

$$Fe^{2+}_{fluence} = \frac{A_{532nm}}{\sigma_{532}} \qquad Fe^{tot}_{fluence} = \frac{A_{342nm}}{\sigma_{342}} \tag{2.9}$$

and the reduction degree R is calculated as

$$R = \frac{Fe^{2+}_{fluence}}{Fe^{tot}_{fluence} - Fe^{2+}_{fluence}} \tag{2.10}$$

However, concerning the reduction degree, it is important to underline that the absorption measurements are integral ones and they provide the total amount of filled traps Fe^{2+}, without giving information on its spatial distribution inside the doped layer. Thus the reduction degree estimated by means of optical absorption technique is a mean over the entire doped regions and it can be considered constant along all the depth only assuming that Fe^{2+}, if multiplied for a convenient factor, has the same in-depth profile of Fe^{3+}. The validity of this assumption will be better investigated in the last chapters of this work, by exploiting holographic measurement technique.

2.3 Best procedure for samples preparation

As previously described at the beginning of this chapter, to realize our lithium niobate crystals locally doped by iron the thermal diffusion process is exploited. However, as already mentioned, this approach not only leads to the diffusion of the dopant inside the substrate, but it also affects the host matrix itself. Thus, it has to be found the best experimental procedure that on the one hand allows to realize the desired doping and, on the other one, preserves the structural quality of the material. For these reasons a systematic study was performed on the effect of the annealing atmosphere on the composition and crystalline structure of the Fe-diffused samples, since they play a key role in the optimization of the photorefractive response of the material. The mentioned investigation is widely discussed in [19] and in the following only the main results are reported, in order to clarify the experimental procedure exploited to realize the samples that will be investigated in the next chapters.

Besides the iron diffusion, a fundamental advantage of the thermal treatment is the possibility to change the dopant valence state, thus different annealing atmospheres were considered in this analysis: the inert Ar gas and the O_2 oxidizing atmosphere for the diffusion process and the reducing $\mathrm{N}_2(96\%) + \mathrm{H}_2(4\%)$ mixture for the post-diffusion treatment. Moreover, to study the influence of the water vapor on the structural quality of the samples, each treatment was performed both in dry and wet atmosphere, this latter by using a water tank where the gas bubbles before entering in the furnace. By exploiting the three analysis techniques discussed in the previous section the following observation were done:

- The diffusion processes performed in O_2 atmosphere lead to more reproducible in-depth iron concentration profiles that those realized by thermal diffusion in Ar, regardless of the dry or wet nature of the gas. Moreover, Ar atmosphere affects more severely the crystal matrix, presenting an higher defectivity on both the faces of the samples, as pointed out by their reciprocal space maps. On the contrary the reciprocal space maps relative to the samples treated in oxygen are characterized by a limited diffuse scattering and a well defined truncation rod, indicating that the textured structure has been more preserved during the thermal annealing in this atmosphere;

- Also the post-diffusion reducing treatment leads to a good quality of the crystallographic structure of the sample, increasing significatively the amount of filled traps Fe^{2+} without changing the dopant concentration profile. In these thermal processes the reducing electrons are provide by the dissociation of the molecule H_2 into e^- and protons, but in any case the hydrogen content of the substrate does not significatively increase with respect to the as diffused samples;

- In all the doped faces less structural disorder and no $LiNb_3O_8$ formation are observed. In particular the lithium triniobate appears only in the undoped face of the samples treated in Ar and N_2+H_2 dry atmosphere, confirming that the oxygen, both dry and wet, and all the wet atmospheres inhibit the precipitation of $LiNb_3O_8$.

- Concerning the incorporation of hydrogen during the thermal treatments, IR spectroscopy shows that the main source of H^+ is the water present in the wet atmosphere, which dissociates and enters in the crystal, increasing its OH content. Moreover it is also important to underline that the dissociation of H_2 during the reducing treatments introduces much less OH groups than those incorporated by the crystal during the diffusion process in a wet atmosphere.

Considering the above mentioned experimental evidences, it is clear that the best choice to realize a local iron doping with the desired reduction degree consists in diffusing the iron film in a O_2 atmosphere, subsequently performing a post-diffusion treatment in a reducing gas mixture (Ar+H_2 or N_2+H_2). Indeed this two-steps process allows to decide and realize separately the diffusion profile and the amount of filled traps of each single crystal. Finally, the wet atmosphere is preferred to the dry one because it prevents Li-out diffusion and the presence of relative defects, as the formation of lithium triniobate on the undoped face of the samples. However it has to take into account that the water present in the wet atmospheres introduces in the crystal OH groups during the diffusion process and the hydrogen, as it will be deeply discussed in the subsection 4.3.2, is the main responsible at room temperature for dark decay of holograms. However, despite this last remark, all the samples investigated in the next chapters are realized in a wet atmosphere and in the fifth chapter it will be also experimentally demonstrated that the hydrogen present in our Fe-diffused lithium niobate samples is not enough to drastically increase the dark conductivity, compromising the holographic measurements. In any case, a future step in the sample preparation will be the hydrogenation of the doped crystal by performing dry thermal treatment at low temperatures (about 400°C), as reported in [18], in order to obtained a low hydrogen content. Obviously, also the effects of this further thermal treatment on the crystallographic structure of the samples will be deeply investigated.

Chapter 3

Microscopic structure of diffused Fe:LN samples

In this chapter the structural properties of diffused iron doped lithium niobate crystals are presented, with special care devoted to the new results.
In the first section it is presented a complete view on the compositional and structural evolution of the Fe_2O_3 - $LiNbO_3$ system during the entire diffusion process.
The second and third sections are devoted to an exhaustive study of the final Fe location in diffused samples. As already mentioned, while in bulk Fe:LN crystals the iron site location was widely investigated, on the contrary in literature there are not studies concerning the iron lattice position in diffused iron-doped lithium niobate sample and this investigation is mandatory to correctly understand the photorefractive response of this material. Indeed, in the usual band transport models it is assumed that Fe locates only at the lithium site, thus behaving as a deep photorefractive center, whereas there are not photorefractive theories which take into account other different iron positions in the lithium niobate matrix. Furthermore, concerning the band transport model with two photorefractive centers, it is important to know Fe lattice site to understand how the dopant interacts with the lithium niobate defect structure. Therefore, by means of ion beam analysis and micro-raman spectroscopy, it was demonstrated that Fe occupies the lithium site also in diffused crystals, regardless of its valence state and pushing out the niobium antisites to their natural location.
Finally, in the last section, they are reported experimental observations on the maximum lattice deformation induced at the surface of a Fe-diffused LN sample: it depends on both the Fe concentration and the reduction degree of the doped layer. These results open the possibility to characterize the ratio $[Fe^{2+}]/[Fe^{3+}]$ along the whole iron concentration profile.
All the results discussed in this chapter are also useful to better understand the optical properties of Fe:LN, which will be deeply discussed in the next chapters.

3.1 New insights on the diffusion process of Fe in lithium niobate crystals

Up to now in literature a study on the microstructural evolution of the lithium niobate matrix during the diffusion of iron does not exist. On the contrary the incorporation of Ti in LN by in-diffusing a thin layer has been widely investigated [24, 25], showing the formation of a Ti-LiNbO$_3$ compound which acts as a source of titanium during the diffusion process. These observations suggested that also in the Fe:LN samples an intermediate phase develops during the thermal treatments and exists until the dopant is completely entered into the substrate. Thus, to investigate this aspect of the iron diffusion process, a set of samples were prepared ad hoc: the same amount of iron [$(6.64 \pm 0.03) \times 10^{20}$ at/m^2] was deposited on eight x-cut congruent LN samples, which were subsequently thermal treated in oxygen atmosphere at temperatures ranging from 600°C to 900°C for 1 or 2 hours, as reported in table 3.1.
Immediately after the thermal treatments it is already visible that each sample differs from the other, since they present a different colour depending on the annealing process. Indeed, while the sample treated at 900°C is transparent, as the samples where iron is completely incorporated in the substrate, on the contrary the samples annealed at lower temperatures present an orange colour (600°C-700°C-750°C) or a yellow one (800°C-850°C), testifying the presence of a superficial residual layer of Fe atoms which has not diffused into LiNbO$_3$. Moreover, by treating a part of each sample in phosphoric acid (H$_3$PO$_4$) in aqueous solution it has seen that only the orange layer was attacked by the acid, leaving an yellow layer in the samples annealed at 700°C and 750°C, whereas the crystal treated at 600°C became uncoloured. Since the phosphoric acid removes the iron oxide, the orange colour has to be attributed to an iron oxide, whereas the yellow layer, which starts to grow under the orange one at 700°C, is probably a compound which contains iron oxide and atoms of the substrate. To study the nature of this probable interlayer each sample was characterized by using SIMS technique, whose results are widely discussed in the Ph.D. Thesis by Dr. M.V. Ciampolillo[19] and summarized in the following:

sample 1	sample 2	sample 3	sample 4	sample 5	sample 6	sample 7	sample 8
1 h at 600°C	1h at 700°C	1h at 750°C	1h at 800°C	2h at 800°C	1h at 850°C	1h at 900°C	2h at 900°C

Table 3.1: *Schematic summary of the samples realized to investigate the diffusion process of iron inside a lithium niobate substrate.*

- In the sample treated at 600°C for 1h the SIMS profiles relative to Fe, O, Nb and Li, show that iron did not diffuse in the substrate and that lithium and niobium concentrations are almost negligible in the residual Fe layer. On the contrary in this layer the oxygen atoms are abundant, suggesting that it is probably a bare iron oxide. This results agrees with the qualitative observations derived by the phosphoric acid H_3PO_4 attack.

- Both the samples annealed at 700°C and 750°C present an exponential decay of the Fe signal from the layer-substrate interface down into the crystal bulk, indicating that iron atoms have started to diffuse into the substrate. Moreover also Li and Nb profiles indicate that at this temperature an interdiffusion of chemical species has occurred between the iron oxide and lithium niobate, which leads to the formation of an interlayer between these two phases of mixed composition.
- In the samples realized at 800°C and 850°C the presence of an intermediate phase is underlined by the profiles relative to Fe, O and Nb signals which are clearly present in a layer of about 40nm. In particular the Nb signal remain constant from the surface of the sample to the bulk material, indicating a non negligible amount of Nb in the interlayer.
- The samples annealed at 900°C present the same in-depth Fe profile typical of samples where the dopant is completely diffused in the lithium niobate crystal. This suggests that the interlayer has been completely, or almost, exhausted.

In addition to the compositional analysis mentioned above, each sample has been characterized by a structural point of view by exploiting the High Resolution X-Ray Diffraction technique and performing ω-2θ scans along the symmetrical reflections (1 1 0), (2 2 0) and (3 3 0) of lithium niobate. While the latter two reflections do not present anomalies respect to those obtained in samples where iron is completely diffused in the substrate, on the contrary the rocking curve relative to the reflection (1 1 0) shows in each sample a further diffraction peak. In fig. 3.1 besides the peak relative to (1 1 0) planes of $LiNbO_3$ (at 17.41°) it is evident the presence of a second diffraction peak at about 18.26°, whose intensity grows with increasing annealing temperature, reaching a maximum in the samples treated at 800 - 850°C. This indicates the formation of a new crystalline phase in these samples. As clearly shown in the inset on the right, the shape of the peak in the sample realized at 600°C is very broadened, indicating that this new phase starts to form at this temperature in the shape of small grains. At 800°C the diffraction peak becomes narrow and it is shifted towards small angles, indicating an increase in the grain size and an expansion of the lattice parameters of the new phase. Moreover while in the sample treated at 800°C for 2 hours the diffraction peak appears unchanged, in the crystal annealed for 1h at 900°C it is considerably less intense, probably because in this sample the interlayer is thinner, and it completely vanishes after a thermal treatment of 2 hours at 900°C. To study how the temperature and the duration of the thermal treatments affect the microstructural evolution of this new phase, an in-situ annealing was realized at the diffractometer and successive rocking curves were performed during the thermal process. The sample investigated initially presented on its surface a thin film with the same amount of iron of the crystal previously discussed, and the annealing was

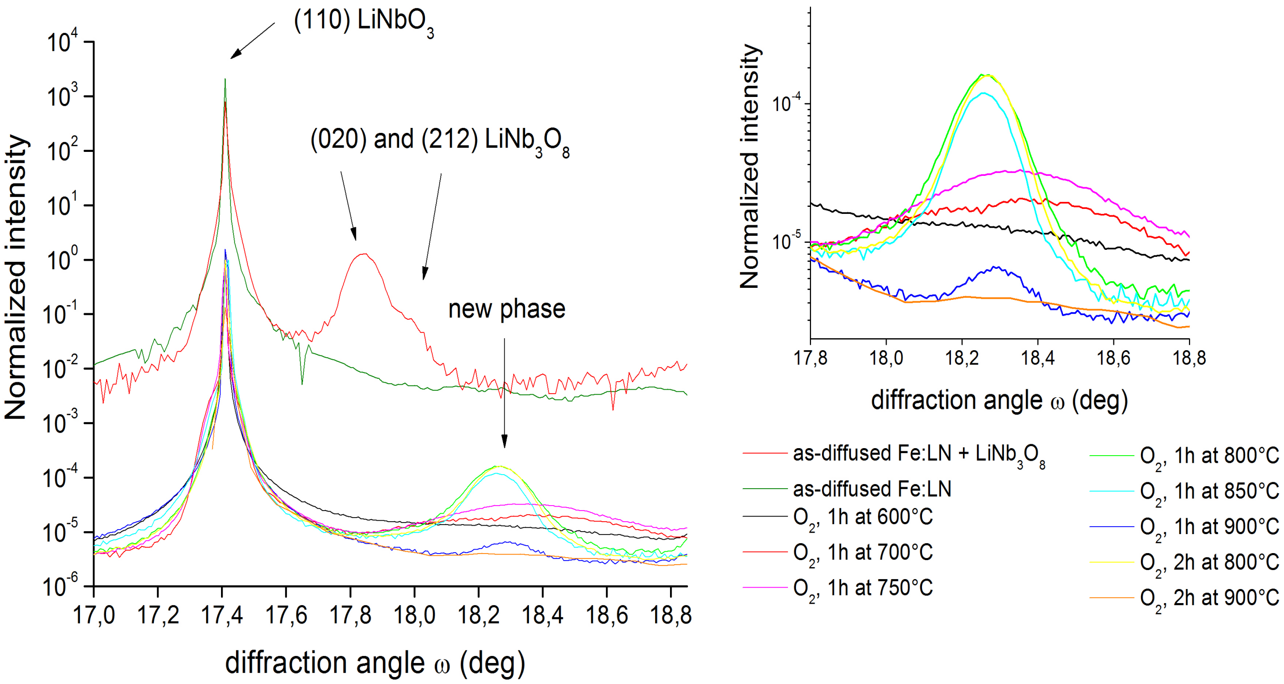

Figure 3.1: *Rocking curves relative to the symmetrical reflection (1 1 0) of LiNbO$_3$ measured in each samples. A further diffraction peak at about 0.85° from the LN peak is evident.*

carried out in a oxygen atmosphere with an heating rate of 200°C/h. Some results are reported in fig. 3.2, where the noise of the rocking curves is due to the short time taken to perform each measure, in order to avoid changes of the shape of the diffraction peak during the measurement. This systematic analysis shows that the new phase previously observed is completely absent at 500°C and it begins to develop at one hundred degrees above. The broadened shape of the investigated reflection is more evident at 700°C, becoming gradually narrower with the increasing temperature, until reaching a well defined peak shape at 800°C, as already observed in fig. 3.1. What it is really new is the fact that the shape and the intensity of this peak does not change while the sample is maintained at the higher temperature for long time, resulting still present after 17 hours at 800°C, while, as mentioned above, it completely vanished after 2 hours at 900°C. These experimental observations can be explained taking into account the different diffusion coefficients relative to these two temperatures, which are $D_{800°C} \simeq (2.9 \pm 0.1)\,\mathrm{nm}^2\mathrm{s}^{-1}$ and $D_{900°C} \simeq (56.1 \pm 6)\,\mathrm{nm}^2\mathrm{s}^{-1}$ [19]. Indeed, assuming that the observed peak refers to an intermediate layer which provides Fe atoms to the substrate, since $D_{800°C}$ is about 20 times smaller than $D_{900°C}$ it derives that at 800°C the complete incorporation of iron inside the material, and the consequent consumption of the interlayer, should occur in 40 hours, which are about 20 times the time required at 900°C to observe the disappearance of the unknown diffraction peak.

To identify this new crystallographic phase, first of all a comparison with other sam-

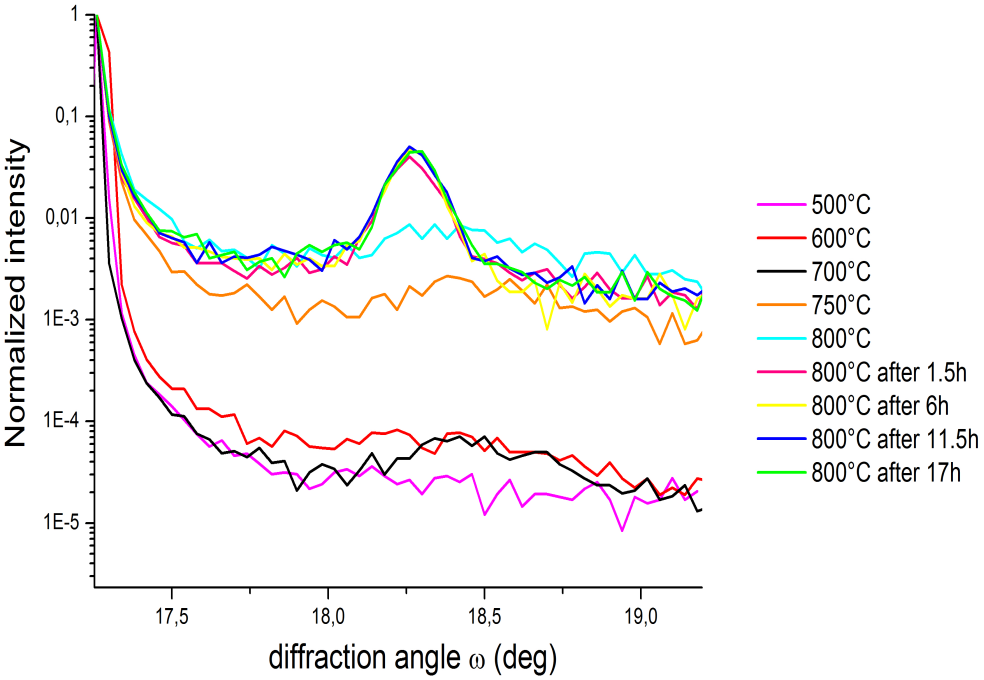

Figure 3.2: *Rocking curves relative to the symmetrical reflection (1 1 0) of $LiNbO_3$ measured in a Fe:LN sample during the diffusion process. The noise of the measurements is due to the short time taken to perform each measures, to avoid changes in the shape of the diffracted peak during the measurement.*

ples was performed, thus in fig. 3.1 there are also shown[1] the rocking curves relative to a sample where a complete diffusion of iron is achieved and another one which presents the existence of the lithium triniobate phase ($LiNb_3O_8$), in addition to the full incorporation of the dopant. It should be noticed that the intermediate phase was not observed in any other samples where the diffusion of Fe in the lithium niobate substrate has completely been accomplished, confirming that long treatments at higher temperatures (8h at 1000°C) completely dissolve this phase. On the other hand the peak at 18.26° cannot be attributed to the $LiNb_3O_8$ phase. In fact, even if this phase possesses two Bragg reflections at $\theta_1 = 18.09°$ (planes (1 2 0)) and $\theta_2 = 18.49°$ (planes (6 0 0)), which are close to the observed one, the epitaxial relations between a $LiNb_3O_8$ layer grown on a x-cut $LiNbO_3$ substrate[25] forbids the observation of these reflections close to the symmetrical (110) reflection of lithium niobate.

These results confirms that a new phase develops during the iron diffusion process which is not simply related to some compound of the Li_2O - Nb_2O_5 system. Considering the previous observations made on the basis of the SIMS profiles, we assume that the intermediate layer is mainly composed by Fe, Nb and O atoms. A possible compound of these three elements which has a reflection at about 18.26° is the *iron niobate* ($FeNbO_4$), with its (120) reflection at the mentioned angle. The iron nio-

---

[1] These two scans were multiplied for an opportune factor for the sake of clarity.

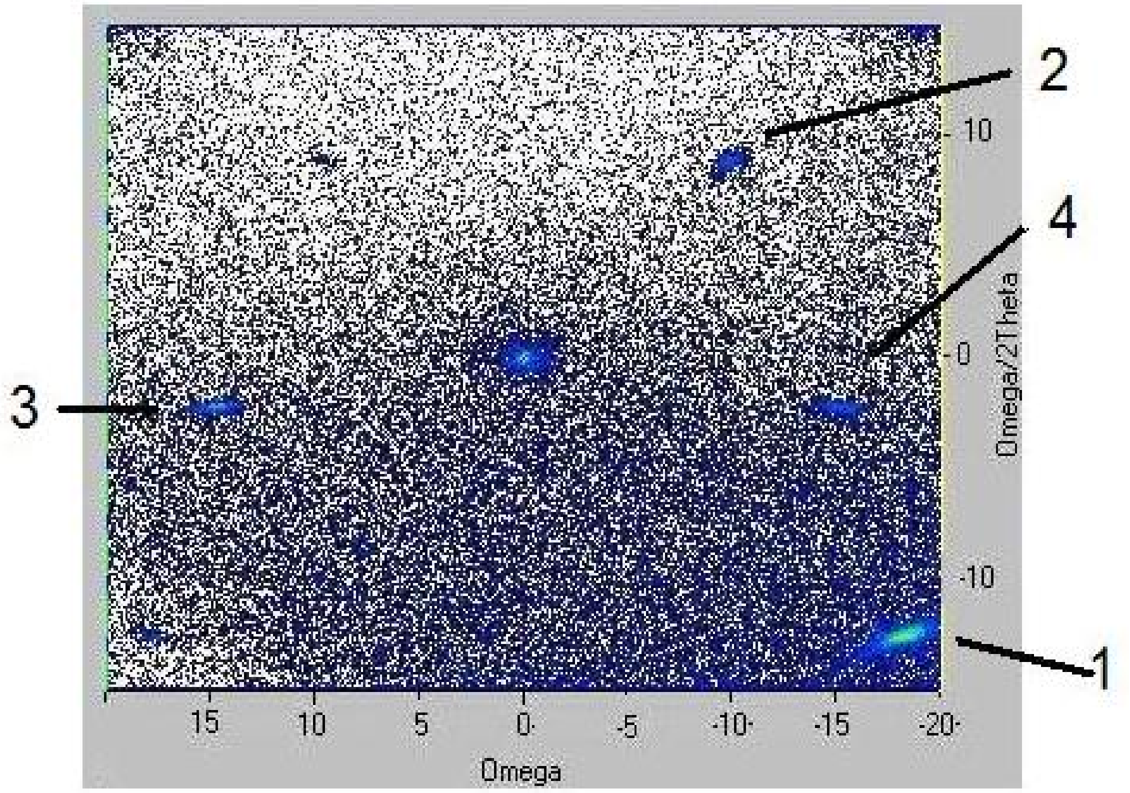

Figure 3.3: *Reciprocal space map around the symmetrical reflection (2 2 0) of* $LiNbO_3$*. Besides the mentioned diffraction peak other ones are present, which refer to* $FeNbO_4$*.*

bate is a compound obtainable from Fe_2O_3 and Nb_2O_5, with possible application as gas sensor material or photodetector, which exhibits three different crystallographic phases: monoclinic, triclinic and orthorhombic[26]. The latter phase is a transition one between the formers two, representing also the passage from an ordered structure to a disordered one. The polymorphism of $FeNbO_4$ can be summarized as follows

$$\text{Monoclinic} \quad \xrightarrow{1077°\text{C}} \quad \text{Orthorhombic} \quad \xrightarrow{1300°\text{C}} \quad \text{Triclinic}$$

The room temperature phase is the monoclinic one, which exists up to 1077°C, with cell parameters: a = 5.006 Å, b = 5.623 Å, c = 4.649 Å and $\beta = 90.4°$[27]. By exploiting once again the diffraction technique, a very large[2] reciprocal space map around the lithium niobate reflection (2 2 0) was realized, to check the presence of other reflections relative to the $FeNbO_4$ interlayer. The measure is reported in fig. 3.3, where other diffraction peaks are present besides the central one which refers to $(2\,2\,0)_{LN}$ planes, indicating that the new phase is epitaxially oriented with respect to the substrate.

---

[2] The ω and the ω - $2\,\theta$ ranges were respectively 40 and 30 degrees, therefore they were used steps of measurement larger than the usual ones (0.1°), decreasing the resolution of the shape of each peak.

peak number	2θ (degs)	LN reflections	$FeNbO_4$ reflections
1	48.69	(2 -2 4) at $2\theta = 48.52°$	(2 2 0) at $2\theta = 48.66°$ (0 3 0) at $2\theta = 48.53°$
2	91.49	absent	(3 4 0) at $2\theta = 91.53°$ (2 3 3) at $2\theta = 91.47°$
3 - 4	69.09	(2 0 8) at $2\theta = 68.50°$	(1 4 0) at $2\theta = 69.38°$ (0 2 3) at $2\theta = 69.16°$

Table 3.2: *Table of the reflections observed in the reciprocal space map and that ones relative to LN or* $FeNbO_4$ *which occur at the same angles.*

For the sake of semplicity, each peak has been labeled with a number, and the corrisponding 2θ angle is listed in table 3.2, where the reflections were indexed according to the $LiNbO_3$ or $FeNbO_4$ lattices. It is interesting to notice that the lithium niobate has not reflection relative to the angle $2\theta = 91.49°$ and, considering the orientation of its crystallographic cell respect to incident and reflected beam, its reflections (2 -2 4) and (2 0 8) are in any case too far from the (2 2 0) one to be detected in this reciprocal space map. Thus only the families of planes relative to the iron niobate can be taken into account. In particular the reflections (2 2 0), (1 4 0) and (3 4 0) are consistent with a $FeNbO_4$ cell which has the $\hat{c}$ axis almost perpendicular to the $\hat{z}$ one of LN, while the other two axes lie in the (0 1 0) plane of the lithium niobate substrate. Further studies are in progress to fully characterize the crystallography of this newly formed layer.

In summary, all the mentioned experimental results shows that during the iron in-diffusion process a intermediate layer is formed at temperature above 700°C, whose crystalline structure has been identified as that of the iron niobate $FeNbO_4$. We suggest that this phase acts as source of Fe atoms for the substrate and, as shown in the HR-XRD analysis, its exhaustion velocity depends on several parameters of the diffusion process, such as the temperature and the duration of the thermal treatment and, obviously, the amount of dopant deposited on the substrate. This finding can have interesting practical consequences, as this phase possesses interesting technological applications, which could be implemented on an optical circuit prepared on the toped of lithium niobate substrate

3.2 Lattice site of iron in diffused Fe:LN crystals

It is known that in a nominally pure lithium niobate crystal the native impurities of iron and the point defects Nb_{Li} have both two possible valence states, respectively Fe^{2+} / Fe^{3+} and Nb_{Li}^{4+} / Nb_{Li}^{5+}, and act as donors and acceptors for the charge carriers, both governing the photorefractive effect of the material. Thus the final photorefractive sensitivity of the crystal is influenced by a complex interplay of all these defects which depends on several parameters, as for instance the reduction degree of each species and their relative concentrations. Obviously all these parameters can be sig-

nificatively changed when the material is doped and a crucial importance is assumed by the lattice site of the dopant, since it can affect the whole crystal structure of the host material and, as consequence, its photorefractive properties.
Concerning Fe doped lithium niobate crystals, several works[28, 29, 30] have been performed on bulk materials grown by Czochralski technique in order to investigate the iron location in this material. Samples with concentrations up to 7% mol have been studied and it was demonstrated that in the LN matrix both Fe^{2+} and Fe^{3+} atoms are in the octahedral geometry surrounded by oxygen atoms and they occupy the Li site. Despite these results, the lattice site of iron in Fe:LN crystals realized by thermal diffusion is up to now not clear and in literature there are not study concerning this topic. While in the Czochralski grown the system assumes at each time the most stable configuration, on the contrary the diffusion process is a non-equilibrium one and the dopant atoms have to find a site in an already established crystalline structure. Therefore it is not obvious that the incorporation of the dopant in bulk and in-diffused samples lead to the same final atoms arrangement and, to better understand the photorefractive properties of diffused sample, a deeper investigation of the iron lattice site in our crystals is necessary. In the following subsections the experimental techniques used to perform this study and the final results will be discussed.

3.2.1 Ion beam analysis

To investigate the defect structure of diffused Fe:LN samples, due to the atomic composition of the examined material a single ion beam analysis is not sufficient to obtain a complete view of the site location of each element, therefore three analysis techniques has been used, exploiting three different interaction mechanisms between an incident ion beam and the atoms of the samples. These techniques are the Rutherford Backscattering Spectrometry (RBS), the Proton Induced X-ray Emission (PIXE) and the Nuclear Reaction Analysis (NRA), which analyzes respectively the energy of the incident particles backscattered by the atoms of the material, the x-rays emitted by these formers and the products of nuclear reactions between the ion beam and some elements of the samples. In fig. 3.4 (a) a typical RBS spectrum performed in a diffused sample is reported as example. Since the energy of the backscattered particles is related to the element of the sample which causes the backscattering, in the spectrum it is possible to recognize the edges referring to Nb, O and Li. However even if this technique is useful to investigate the Nb signal, it can not be exploited to study also the Fe and Li ones. Indeed the amount of dopant inside the sample is low, thus its signal is covered by that relative to niobium, while the analysis of the Li signal is complicated due to the fact that lithium is the lighter element of the material and that its signal lies at lower energies, overlapping those relative to both oxygen and niobium. For these reasons besides the RBS technique, also PIXE and NRA ones has been performed to realize this study, providing informations respectively on Fe and Li atoms. The NRA technique measures the energy of the α particles produced

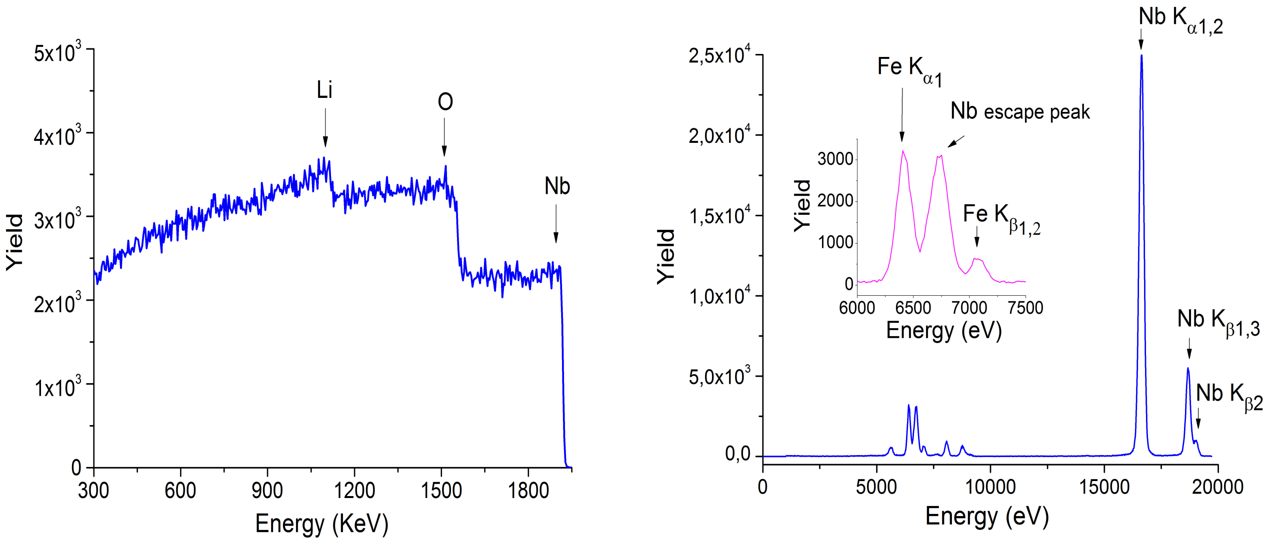

(a) *(b)*

Figure 3.4: *Examples of an RBS spectrum (a) and a PIXE one (b) performed on a diffused Fe:LiNbO*$_3$ *crystals.*

in the nuclear reaction $Li^7(p,\alpha)He^4$, thus the signals are due only to Li species, and in the PIXE spectra the K_α line of iron is taken into account, to verify the presence of the dopant. As way of example in fig. 3.4 (b) it is reported a typical PIXE spectrum obtained in a diffused Fe:LN sample: the K lines relative to Nb and Fe are well distinct, thus it is easy to analyze the respective signals, and in the inset, besides the Fe K_α and K_β peaks, also an intense peak due to Ge detector escape phenomenon of Nb photons is present. In particular by comparing the values of the escape peaks measured in an undoped crystal and Fe-doped one, it is possible to estimate the background present below the Fe peaks, obtaining the correct value of the K_α line of iron. Finally all the measurements were performed in a channeling configuration, that is aligning the incident beam along a certain crystallographic direction, so the incident particles are channeled in a axis or a plane of the crystal. Then, by rotating the sample, single spectra were collected at different incident angles of the beam with respect to that of the chosen lattice direction, obtaining angular scans.

The experiment was carried out at the AN accelerator of Laboratori Nazionali di Legnaro (Padova, Italy, by using a proton beam. The beam charge collection was performed by using the whole scattering chamber as a Faraday cup, reaching an accuracy better than 1%. In order to avoid charging effects during NRA-RBS-PIXE analyses a 10 nm thick sputtering deposition of Al was performed on all the samplesand all the measurements were always performed with a beam current lower than 20 nA. The sample holder was a two-axis remote-controlled goniometer allowing channelling alignments with an accuracy of about 0.01°. Two translation movements are also available, allowing to locate the beam spot of about 1x1 mm^2 on the sample surface

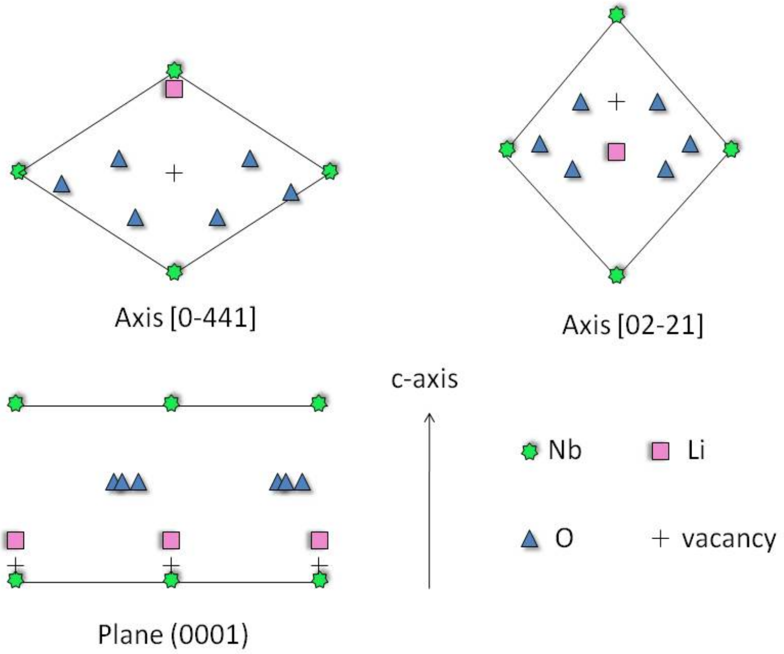

Figure 3.5: *Projection of the mentioned directions on the planes normal to them. The Nb, O, Li and free octahedral positions are indicated.*

with an accuracy of a tenth of millimeter. RBS and PIXE signals of all the samples were contemporary collected with a 2 MeV proton beam by using a silicon solid-state detector with a 170° scattering angle for backscattered particles and a Ge hyperpure detector for the beam induced X-rays. A 12 μm thick Cu filter is positioned in front of the X-ray detector to cut the low energy X-rays due to O and Li and to reduce the intensity of the strong Nb fluorescence peak. Moreover a mylar foil is used to prevent the backscattered protons from reaching the Ge detector. Finally the NRA measurement were realized at 1.6 MeV on an undoped sample, to obtain the Li channeling signal to compare with those of Nb and Fe, and a 300 mm^2 detector with a solid angle of about 0.2 mrad and a mylar film to suppress Rutherford backscattered particles was used in this case.

3.2.2 Results and discussion

In order to investigate the lattice location of Fe, they have been measured three samples with the same iron concentration profile (1.75×10^{26} at/m^3 at the surface and 4.1 μm as average penetration depth), but different amount of filled traps ($Fe^{2+}/Fe_{tot} \simeq 1\%$ - - 26% - 100%) in order to verify if the iron valence state affects its lattice site. To realize this study the planar direction (0 0 0 1) and the axial ones [0 2 -2 1] and [0 -4 4 1] were examined, since they allow to investigate all the possible lattice sites present

Crystallographic direction	PIXE (Fe) depth (μm)	NRA (Li) depth (μm)	RBS (Nb) depth (μm)
plane (0001)	2.9	2.3	1.8
axis [0-441]	3.1	1.7	1.7
axis[0-221]	3.0	1.2	1.2

Table 3.3: *Average depth investigated by each ion beam analysis along the chosen crystallographic directions.*

in a lithium niobate crystal, determining without doubt which one is occupied by iron. The projections of the chosen directions on planes normal to them are reported in figure 3.5. As it is possible to notice the axial direction [02-21] puts in evidence both the vacancy site and the lithium one, since they lie at the center of the channel, whereas the latter position is partially hidden by the niobium rows along the [0-441] axis. Moreover by using (0001) planes it is possible to probe the lattice location of niobium, lithium and the free octahedral.

However, before starting with the discussion of the results, some considerations on this kind of lattice position characterization has to be done. Indeed, to correctly interpret the obtained angular scans, first of all it has to considered the interaction potential between the atoms of the lattice and the incident protons. As reported by Rebouta et al.[30], the potential energy in the (0001) plane is minimum when the beam interacts with the Li plane, whereas it is maximum in the case of Nb and O planes. Moreover the niobium and oxygen planes play a comparable role, due to the fact that the atomic plane density of oxygen ions is three times that of the niobium ions, thus along this crystallographic direction the beam is confined between them. As a consequence the free octahedral site and the lithium one lie at the center of the investigate channel. Similar considerations suggest that also in the [0-441] direction the beam confinement is slightly shifted towards the upper part of the channel due to oxygen matrix, but anyway the free octahedral site is probed, whereas that relative to lithium is completely hidden by Nb rows. As the same manner, also in the axial direction [02-21] the lithium site is partially hidden, since the incident protons are induced to be channelled between oxygen and niobium rows. Besides the just mentioned considerations, it has also to take into account the fact that each ion beam analysis technique provides signals which refer to different depths inside the sample, since they are exploiting different interaction mechanisms between the protons beam and the lattice ions. Thus the depths investigated by each technique, reported in table 3.3, has been calculated by dr. Davide De Salvador and dr. Nicola Argiolas as explained in the following. Concerning the depth sensitivity of the Fe PIXE signal, it is influenced by three factors: the reduction of Fe content by increasing depth, the decreasing of the photo-emission cross section with increasing depth due to a reduction of the proton energy and the absorption of the out-coming X-rays by the $LiNbO_3$ matrix. Thus the decreasing of the PIXE signal sensitivity by increasing the depth can be estimated by properly considering the incoming angle of the proton and out-coming angle of the X-ray and by using the tabulated values of stopping power[31], PIXE cross section[32] and X-ray absorption coefficients[33]. In the case of the RBS the signal relative to niobium was integrated in the range from 1560 to 1950 KeV, that is from the upper energy to the O edge (see fig. 3.4) and, by performing RBS simulations, the average depth corresponding to this integration window was estimated. Finally, by computing several simulations with the help of the simNRA sofware it was decide to integrate the whole energy range of each NRA spectrum: in this way the whole depth investigated by this technique is taken into account and it results comparable with that relative to RBA signal, but smaller than the Fe PIXE one.

In fig. 3.6 the main results are summarized, reporting for Fe, Nb and Li respectively the signals obtained by PIXE, RBS and NRA characterizations: the signal yield measured at a given angle is normalized with the corresponding one obtained in a non-alignment condition, then the final values are plotted as a function of the misalignment angle. In the first column on the left the iron signals relative to the three Fe:LN crystals are shown, while on the right the Nb and Li signals relative the undoped sample are reported. The first row of fig. 3.6 regards the (0001) planar direction and it is possible to see that both iron and lithium signals present a flux peak when the beam is aligned with (0001) planes, whereas niobium present a deep profile. Remembering that, as mentioned above, the beam is confined between oxygen and niobium planes, these first results means that the iron occupies a lattice position between the confining planes, that is the lithium site or the free octahedral one. Moreover another important result is that the all the three PIXE signals are comparable within the errors, even if they refer to samples with different reduction degrees, demonstrating that the reduction treatment does not significantly change the iron position inside the hosting matrix. Considering the angular scans along the axial direction [0-441] (second row of fig. 3.6), both lithium and niobium signals fall down when the beam is aligned with the axis, as also observed in the iron signals which clearly follows the lithium profile. In this crystallographic direction the intrinsic vacant sites are at the center of the channel, thus the absence of a flux peak in the iron signal rule out that an appreciable fraction of Fe is located at the free octahedral position. Moreover once again it is proved that the valence state of Fe does not affect its lattice position. Finally, also in the last angular scans along the [02-21] axis it is evident that the iron and lithium profiles are very similar, as confirmed by their full widths at half maximum, which are the same within the errors ($\omega_{Fe} = (11 \pm 2)\,^\circ$ and $\omega_{Li} = (15 \pm 3)\,^\circ$), whereas the niobium signal present a wider deep profile. However, in both the axial directions the Fe profile is not perfectly equal to that of Li, but it appears slightly less deep: this fact can be reasonably attributed to the different depth investigated by these two techniques. Indeed the channeling profile results more smoother with increasing probed depths, due to the beam flux progressive randomization. Thus, since the difference in the average depth investigated by PIXE and NRA is more considerable in the axial directions than in the planar one (see table 3.3), it is expected that also the differences in the deep profiles are more evident

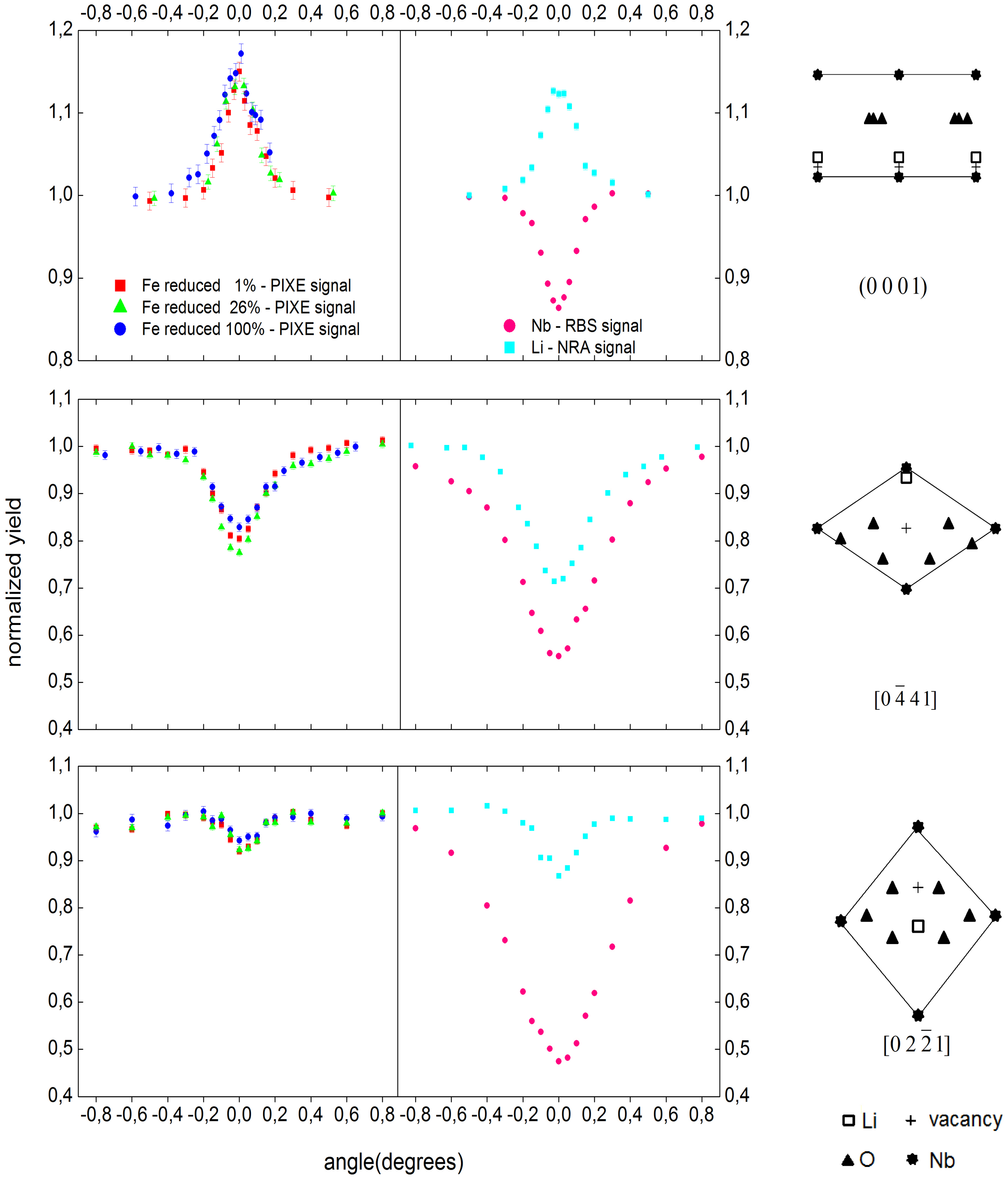

Figure 3.6: *Angular scan along the planar direction (0001) and the axial ones [0-441] and [02-21]. In the column on the left the Fe (PIXE) signals relative to the three samples with different reduction degrees are reported, while in the column on the right the Nb (RBS) signal and the Li (NRA) one are shown. The error bars relative to the values obtained with NRA and RBS measurements are often small than the size of the experimental points.*

in the former directions, as experimentally verified.
In summary, by means of ion beam analysis diffused Fe:LN samples has been structurally characterized, demonstrating without doubts that iron inside the $LiNbO_3$ matrix is substitutional to Lithium, as observed in bulk Fe:LN samples grown by Czochralski technique. Moreover it has been proved that the reducing thermal treatment does not change the iron lattice site, even in fully reduced samples. Finally, Montecarlo simulations can be performed to study small displacements of the dopant with respect to its proper lattice site: by exploiting the simulations reported in [34] it follows that in our samples iron is mostly located at the Li site within 0.2 Å. However a deeper investigation of this aspect are planned for the near future.

3.3 Micro-spectroscopy on diffused Fe:LN samples

Both Polaron Luminescence and Raman spectroscopies are widely used to investigate the structural properties of materials, providing informations on the structural quality of the sample, its defect structure and so on. Thus, in the following both these techniques will be exploited to study the incorporation mechanism of the dopant in our Fe-diffused lithium niobate samples, with major attention on its final lattice position and how this affects each sublattice of the material.

3.3.1 Micro-Raman spectroscopy

Raman spectroscopy was discovered in 1928 by the Indian physicist sir C.V. Raman and it investigates the inelastic scattering of a monochromatic light hinting on a sample, deriving informations on the sublattices constituting the considered material and its defect structure. Moreover, Raman spectroscopy can be combined with a confocal microscopy (micro-Raman spectroscopy) allowing to obtain all the mentioned informations at the micrometer-scale, an approach very convenient to study our in-diffused Fe:LN samples.
To characterize Fe:LN doped sample the $A_1(TO)$ phonons, which are related to ionic motions along the ferroelectric axis $\hat{c}$ of the lithium niobate, were investigated. Indeed it is exploited the fact that the four lines visible in the Raman spectrum are well resolved (see fig.3.7) and provide separate informations on the sublattices of the matrix[35]. The $A_1[TO_1]$ phonon is associated to the out-of-phase motion of Nb ions against O ions, providing information on the niobium sublattice, also called B site; the $A_1[TO_2]$ is mainly sensitive to the Li lattice position (site A), since it is related to the vibration of Li and O ions in opposite directions; the $A_1[TO_3]$ is associated to the oxygen ions motion, while the line relative to the $A_1[TO_4]$ phonon is affected by any distortion of oxygen octahedron, and thus of the whole lattice. These Raman lines have been already used to investigate the influence of the thermal treatment in the preparation of our Fe-diffused samples[36], observing that the slight damage caused by the O_2 diffusion treatment (1000°C) is canceled by the reducing post-treatment ($N_2 + H_2$ at 500°C), which leads on the diffused surface to a more ordered

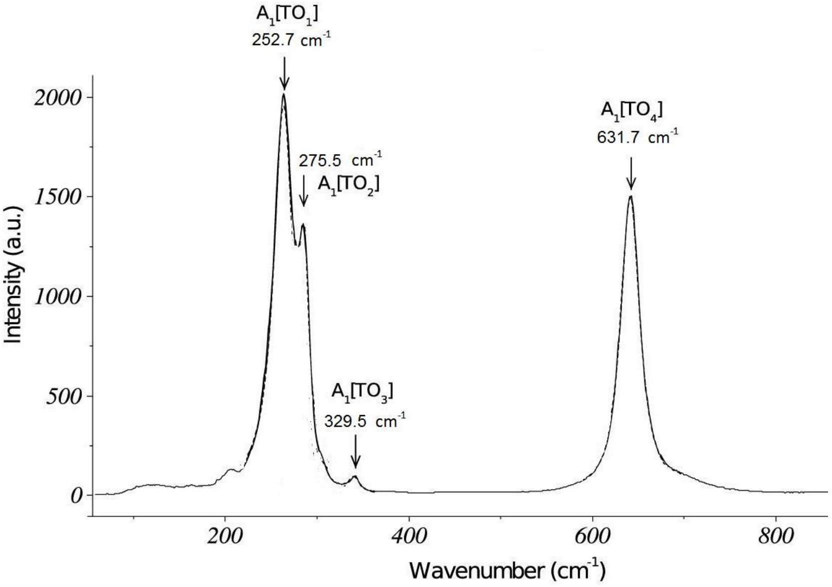

Figure 3.7: *Raman spectrum of a diffused Fe:LN sample obtained in the Y(zz)Y configuration.*

and compact structure, besides the desired increasing of filled traps Fe^{2+}. Moreover, the previously mentioned Raman lines can also be used to study the incorporation mechanism of a dopant inside the host material, since the final position of the extrinsic defects affects the sublattices of the $LiNbO_3$, changing the frequency and the damping of the measured lines. Thus in the following the Raman spectroscopy technique was exploited to investigate the iron lattice site in diffused Fe:LN samples.

Micro-Raman measurements were carried out in Metz, at Laboratory LMOPS, in cooperation with dr. M.D. Fontana and dr.ssa S. Mignoni. The 633 nm exciting line of a He-Ne laser with 1 mW power was exploited, in the backscattering geometry and by using a confocal spectrometer LabRam, with an 100x objective and a 1800 tr/mm grating. The Raman line at 521 cm^{-1} of a Si crystal was used for spectrometer calibration at the beginning of any series of measurements, in order to avoid any drift, and two polarizers provide the desired polarization for both the incident and the scattered light. To perform a Raman in-depth profile along the iron concentration one, a scan along the dopant diffusion direction, $\hat{x}$ axis, is possible in principle, thanks to the confocal geometry. However in these samples a depth dependent change of the instrumental broadening makes the analysis quite difficult. Thus, to limit this problem a scan on the lateral face of the sample is preferred, since in this way the scattering cross section remains constant for the different points along X. To realize these lateral scans after the diffusion process the samples have been carefully polished on both the Y and Z faces and the Y(ZZ)Y configuration has been used, since it allows to obtain only the A_1[TO] phonon modes investigated in this study. Moreover, all the profiles, performed by realizing scans on the lateral Y face of the sample along the crystallographic direction X, start from the doped edge of the crystal to reach about 20μm

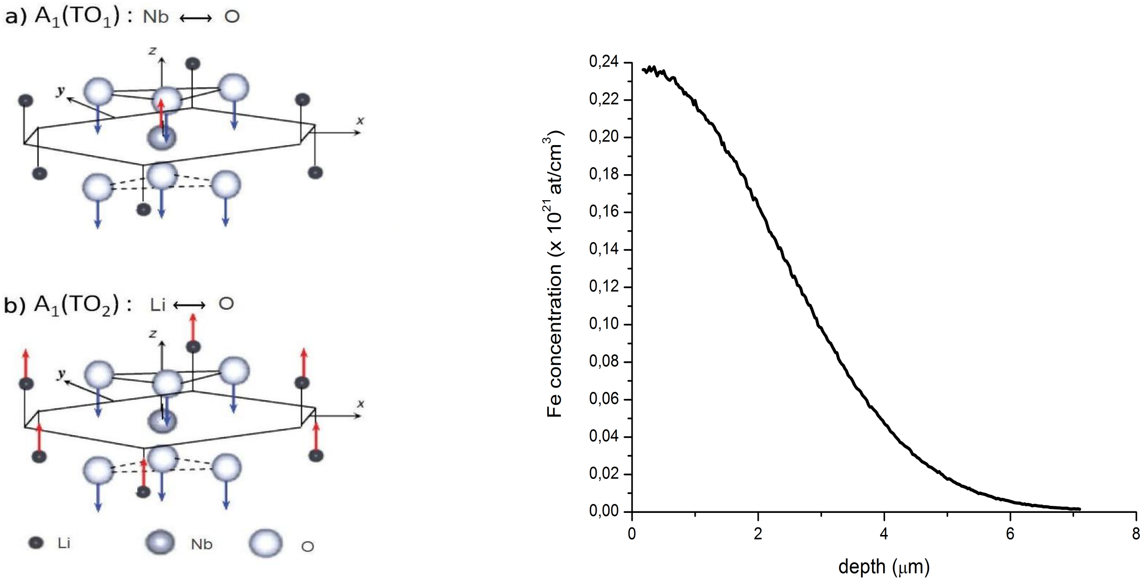

(a) *(b)*

Figure 3.8: *(a)Schematic illustration of the two lattice modes involved in the measurements. $A_1(TO_1)$ is the collective motion of Nb against O sublattices; $A_1(TO_2)$ corresponds to the motion of Li against O sublattices.(b) iron concentration in-depth profile of the samples investigated in the present analysis.*

inside the sample, with 1μm steps. Concerning the samples investigated in this study, they are cutted from the same starting Fe-diffused lithium niobate crystal, thus they have the same semi-gaussian concentration profile, characterized by a maximum iron concentration at the surface of 1.3% mol, a width at half maximum of 2.5μm and a diffusion depth of about 7μm (fig.3.8 (b)). In order to study how the valence state of the dopant can affect the substrate, after the diffusion process, one sample was left in its almost completely oxidized state, whereas the other ones underwent a reducing thermal treatment (1.5 hours at 500°C in $N_2 + H_2$): their reduction degrees are respectively 1.5% and 39%. Moreover, since, as reported in [19], the reducing treatment does not change the iron concentration profile, a direct comparison between the oxidized and the reduced sample can be made. Finally, all the considered samples have been annealed in a wet atmosphere, to avoid lithium out-diffusion because it, as also reported in [36], creates in the samples diffused in a dry atmosphere a damage which is not subsequently recovered by the reducing treatment.

In the present analysis the $A_1[TO_1]$ and $A_1[TO_2]$ phonons are considered, since, as mentioned above, they are able to specifically probe Li(A) and Nb (B) sites, studying the vibrational motions associated to these ions (fig. 3.8). Several spectra measured at different depths have been fitted with a sum of damped harmonic oscillators and in fig.3.9 for each Raman line the obtained frequency and FWHM are reported as a function of depth. As it is possible to notice, the frequency of the $A_1[TO_1]$ mode presents in both the samples an increase from the substrate to the doped surface,

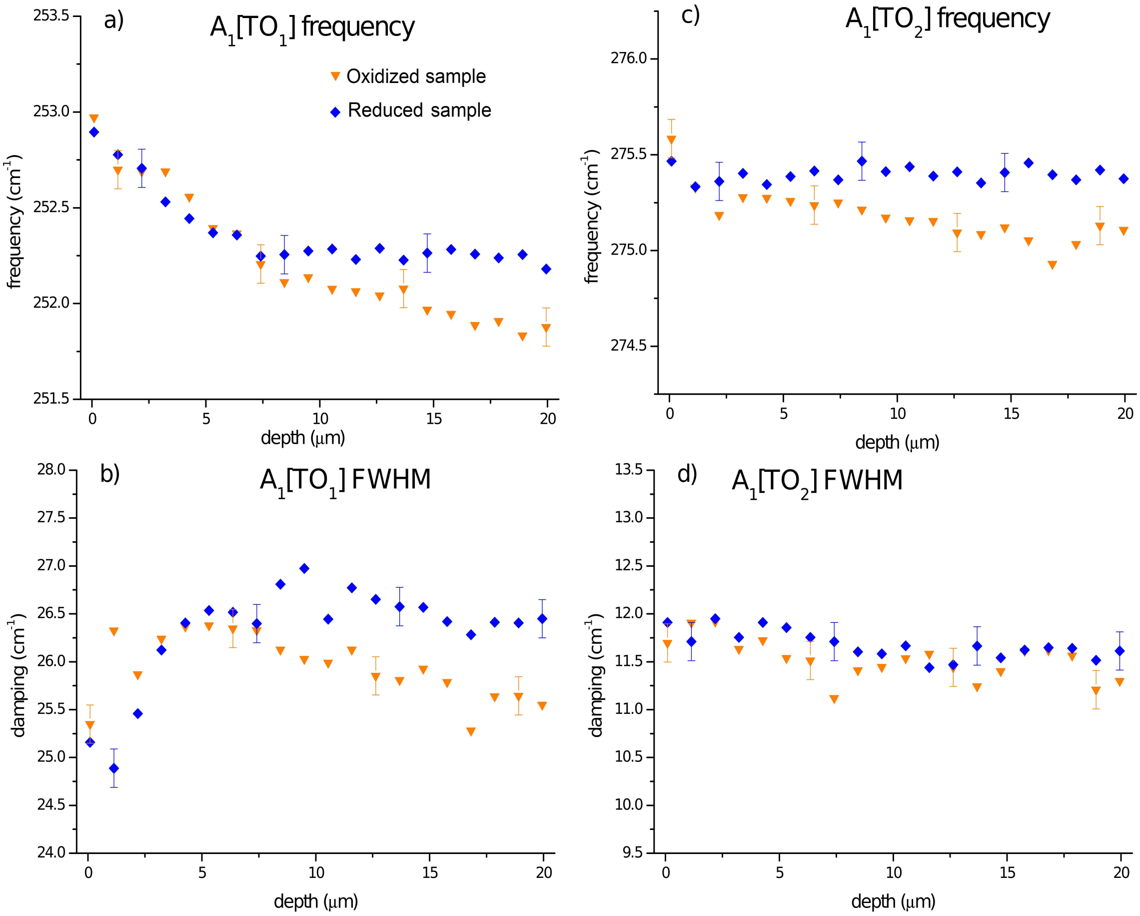

Figure 3.9: *In-depth profiles of the frequencies and the FWHM relative to $A_1(TO_1)$ and $A_1(TO_2)$ phonons, obtained in a reduced Fe:LN sample and an oxidized one. The error bars are not reported on all the experimental points to make more clear the figure.*

following a profile which is in remarkable agreement with that one provided by the SIMS analysis (fig.3.8 (b)) and reaching a constant values after about 7-8 μm, which is exactly the iron diffusion depth. The frequency shift is not so large (0.5 to 0.7 cm^{-1}) but significant enough to be attributed to Fe doping. Indeed the used step of 1μm ensures that the measured values are completely independent from one point to another one along the iron concentration profile, thus the observed profile is reliable and all the above observations supports the idea that the observed frequency profile is caused by the incorporation of Fe into the lithium niobate lattice. Moreover also the damping of the $A_1[TO_1]$ line shows a change on approaching the surface of the crystal, with a gradual decreasing of the measured values, recalling the same depth dependence of the frequency. On the contrary, both the frequency and the damping relative to the $A_1[TO_2]$ mode remain constant along the investigated depth. Remembering that the frequency increase is related to a strengthening of chemical bonds and the damping decreasing to a diminishing of the lattice disorder, the depth dependencies exhibited by the $A_1[TO_1]$ phonon and the constancy of the $A_1[TO_2]$ properties at fist blush could suggest that, irrespective of the dopant valence state,

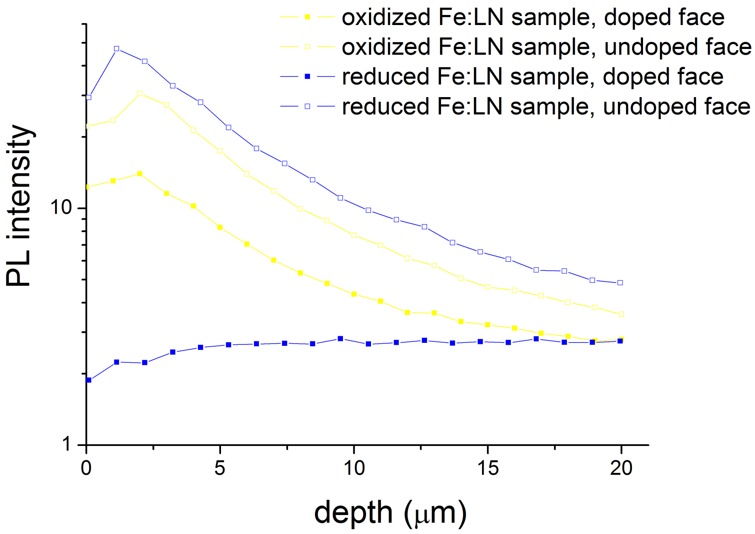

Figure 3.10: *In-depth profiles of the frequencies and the FWHM relative to $A_1(TO_1)$ and $A_1(TO_2)$ phonons, obtained in a reduced Fe:LN sample and an oxidized one. The error bars are not reported on all the experimental points to make more clear the figure.*

the Fe incorporation affects only the B site, whereas the A site results unchanged. However also assuming that the Fe atoms go in the Nb lattice position, this should induce a disorder in the Nb sublattice and therefore an increasing of the damping of the $A_1[TO_1]$ mode, exactly the opposite of the observed experimental measurements. In any case the mentioned incorporation mechanism has to be discarded above all because the ion beam analysis discussed in the previous chapter has demonstrated undoubtedly that both Fe^{2+} and Fe^{3+} occupy the lithium lattice site, thus the Raman data obtained in this analysis has to be explained in agreement with the results found by combining PIXE, NRA and RBS techniques. The more realistic hypothesis is that when the Fe ions are incorporated in the A site, they push away the Nb ions from the antisite position back to their natural site, which is the B one. Hence the damping decrease and the frequency increase observed in the $A_1[TO_1]$ phonon is due to a replenishment of the niobium vacancy by Nb ions, which induces a strengthening of chemical bonds involved in the Nb sublattice and a structural re-ordering of the latter. The fact that the $A_1[TO_1]$ mode does not present significatively variations both in the frequency and in the damping can be explained considering the fact that if all the Nb_{Li} pushed out from the A site are replaced by Fe ions, since both them are source of disorder for the Li sublattice this change affects only slightly the characteristics of $A_1[TO_2]$ mode and the corresponding Raman line results unaffected by this iron incorporation mechanism.
All these results are also confirmed by the Polaron Luminescence measurements discussed in the following subsection.

3.3.2 Polaron luminescence

It is well known that in congruent lithium niobate crystals the niobium antisite defect Nb_{Li}^{5+} is able to trap an electron on an energy level below the conduction band, giving a small bound polaron Nb_{Li}^{4+}. Moreover, in the dark and at room temperature the electrons trapped by two neighboring Nb_{Li} and Nb_{Nb} atoms form a bound state, indicated as Nb_{Li}^{4+} - Nb_{Nb}^{4+} and called *bipolaron*, and when the sample is illuminated by visible light a two-step photoexcitation process should be involved: a first photon dissociates the bipolaron and then a second one ionizes one of the two polarons previously created. Thus, in the range between 700 and 950 nm it is observed a broad luminescence band, which is always present in congruent LN, also doped, but vanishes in the stoichiometric one[37]. This luminescence band presents two main contributions, both due to polaron excitation: a gaussian peak centered at 790 nm and a wider lorentzian peak centered at 880 nm.
Since the intensity of polaron luminescence (PL) band is proportional to the concentration of polarons created by the previous dissociation of bipolaron, it can be used to monitor the presence of niobium antisite in the Fe-doped layer of our samples. Hence, the same samples previously characterized by micro-Raman spectroscopy have been also investigated by performing Polaron Luminescence measurements. All the measures were realized at 633 nm, wavelength at which the PL process is enough efficient, exploiting the same set-up described in the previous subsection. In-depth profiles were realized on the lateral faces of the sample, both on the doped and the undoped sides, by using the Z(yx)Z configuration. In each spectrum the total intensity of the whole luminescence band was normalized to the intensity of a reference Raman line: the final values are reported in fig.3.10 as a function of depth. It is evident that all the profiles, except that relative to the doped face of the reduced Fe:LN sample, present an enhanced polaron luminescence near the surface of the crystals. This fact can be explained taken into account that during the non-equilibrium diffusion process it occurs a rearrangement of the structure, due to both O and Li out-diffusion, which induces the creation of further Nb_{Li}. On the contrary the decreasing of PL at the doped face of the reduced sample has to be attributed to the absorption of the exciting light by Fe^{2+}, whose absorption D band includes also the wavelength used in this experiment (633 nm). However, the main interesting feature is that both in the oxidized sample and in the reduced one the PL intensity is lower on the doped face of the sample with respect to the undoped side. This fact suggests that in the doped face the amount of niobium antisites is lower, confirming the results obtained by Raman experiment. Indeed, since Fe substitutes for Li pushing out the niobium antisites to the B site, it is expected that in the doped layer the Polaron Luminescence decreases, as experimentally verified. Moreover, a further decrease of the polaron luminescence intensity is observed in the reduced sample. This fact is not well understood yet, because a strong signal should be expected in this case. This fact seems to suggest that further elements may affect the intensity of the polaron luminescence signal. Further studies are in progress on this aspect.

3.4 Relation between lattice deformation and reduction degree

As mentioned above, the incorporation of iron in a lithium niobate structure induces a lattice rearrangement, which is proportional to the dopant concentration and presents an in-depth dependence. Therefore it is not surprising that not only a single sublattice, but the whole crystallographic structure of the material is affected by the iron incorporation, presented at the surface a slightly strained layer. Moreover, since the realization of optical devices requires the capability to control and optimize the structural properties of the material and both Fe concentration and the reduction degree $[Fe^{2+}]/[Fe^{3+}]$ are key parameters in determining the photorefractive response of Fe:LN sample, in the following a relation between all these aspects is searched and investigated.

For this study three Fe-diffused samples with different dopant concentration profiles were prepared, adopting the experimental conditions reported in table3.4. Since after the diffusion treatment the iron is mainly in its oxidation state (Fe^{3+}), to increase the amount of filled traps Fe^{2+} each sample underwent one or more subsequent reducing treatments, realized at 500°C in a gas mixture of $Ar(96\%) + H_2(4\%)$. Besides the Secondary Ion Mass Spectrometry, after each preparation step the samples were also characterized by means of High Resolution X-ray Diffraction and Optical Absorption measurements at 532nm, which, as already discussed in chapter 2, allow to determine respectively the vertical lattice deformation and the reduction degree of the material. From the compositional point of view, all the samples show a semi-Gaussian iron concentration profile, which, as previously mentioned, does not change after the reducing treatment, since the low temperature of this thermal treatment does not allow further diffusion of dopant inside the crystal. Thus, if between the oxidized and the reduced samples some variations on the structural properties of the material are observed, they have to be attribute only to the different valence state of the dopant. In fig.3.11, as way of example, the optical absorption spectra and the symmetrical (3 3 0) rocking curves relative to the sample A are reported. It is evident that the intensity of the absorption D band, proportional only to Fe^{2+}, grows with longer reducing treatment, confirming the increase of the number of empty traps in the reduced samples. Concerning the rocking curves, they clearly show that the valence state of the

Sample	Diffusion treatment	Surface concentration of Fe (x 10^{26} at/m^3)	First reduction treatment duration (h)	Second reduction treatment duration (h)
A	8h at 1000°C	1.75 ± 0.05	1.5	1.5
B	8h at 900°C	2.30 ± 0.06	0.5	–
C	10h at 900°C	2.4 ± 0.06	1.5	0.5

Table 3.4: *Preparation conditions of the samples and surface concentration values.*

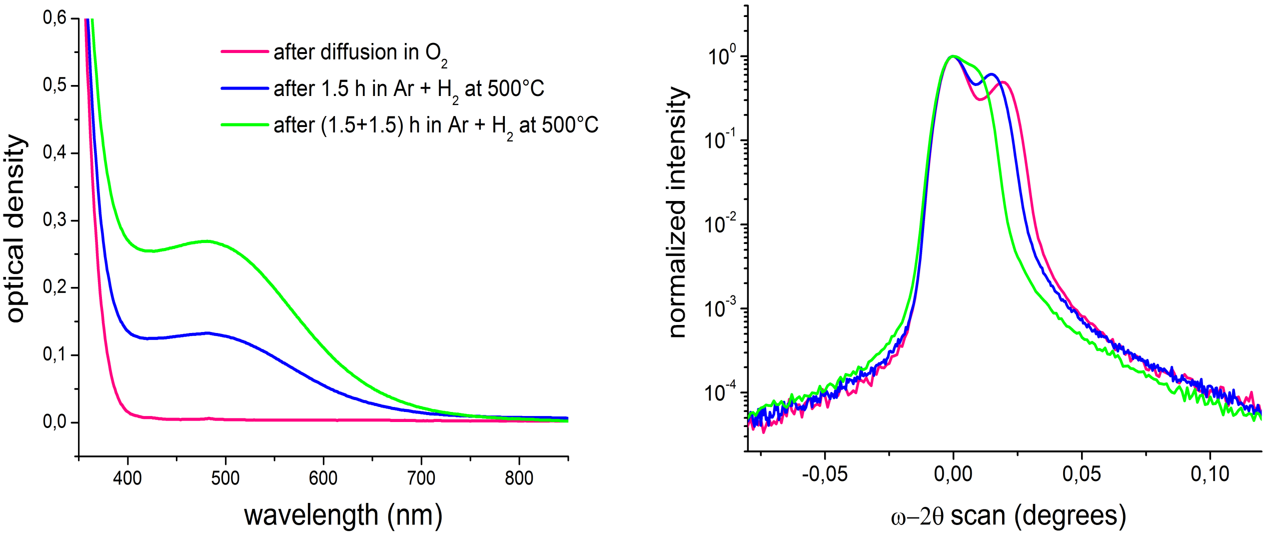

(a) *(b)*

Figure 3.11: *Optical absorption spectra (a) and symmetrical (330) rocking curves (b) relative to sample A, after subsequent reducing treatments.*

dopant affects the structure of the sample. Indeed, the angular separation between the peaks relative to the substrate and the doped layer progressively decreases in reduced samples, meaning that the lower the concentration of empty traps, the lower the lattice compression present in the doped layer. This behavior is confirmed for all the investigated samples and suggests that in the lithium niobate matrix Fe^{3+} acts as a strain point source more effective than Fe^{3+}.

Assuming that Fe ions in the lattice do not interact with each other, the deformation of the crystal lattice is simply given by a superposition of the contributions from all the defects. Moreover, remembering that the doped layer is pseudomorphous to substrate and by using the linear theory of elasticity, a relation between the vertical lattice mismatch and, separately, the concentration of Fe^{3+} and Fe^{3+} ions can be derived

$$\xi_{\perp} = k_1 \, c_{Fe^{3+}} + k_2 \, c_{Fe^{2+}} \tag{3.1}$$

where k_1 and k_2 depends on the orientation of the sample. At this point it is also easy to link the mismatch to the absorption coefficient α, derived from optical measurements. Indeed $\mathrm{c}_{Fe^{3+}} = \mathrm{c}_{Fe} - \mathrm{c}_{Fe^{2+}}$ and $[\mathrm{Fe}^{2+}] = \alpha \, / \, \sigma$, which provide

$$\xi_{\perp} = k_1^{'} \, c_{Fe} + k_2^{'} \, \alpha \tag{3.2}$$

with

$$\begin{aligned} k_1^{'} &= k_1 \\ k_2^{'} &= \frac{k_2 - k_1}{\sigma} \end{aligned}$$

where σ is the absorption cross section relative to 532nm.
Since in the iron diffused samples, both the Fe concentration and the optical absorption are depth dependent, in the following, for simplicity, we will focus our analysis on the sample surface, that is by considering the strained mismatch and the optical absorption data referred to the top of the diffusion profile, where both the strained mismatch and the optical absorption coefficient are maximum. This procedure is also necessary because the investigated samples have different diffusion profiles and therefore they are not directly comparable considering the whole doped layer. As mentioned in chapter 2, the relative perpendicular mismatch measured by HRXRD technique is the maximum one present in the doped layer and thus it already refers to the surface of the sample ($\xi_{\perp} \equiv \xi_{\perp,max}$). On the contrary, the absorbance A obtained by optical measurements is relative the entire Fe^{2+} amount present in the sample and distributed along the diffusion depth. Thus in order to calculate the absorption coefficient at the surface α_{max} of each sample, we have to assume that the reduction degree $[Fe^{2+}]/[Fe^{3+}]$ is constant along the whole diffusion profile, so that the Fe^{2+} concentration is a fixed percentage of the local Fe ions concentration, independently of the depth. In this way α_{max} can be derived by using

$$\alpha_{max} = A \cdot \frac{c_{Fe,max}}{F} \tag{3.3}$$

where c_{max} and F are respectively the surface iron concentration and the fluence of the sample, and the relation 3.2 became

$$\xi_{\perp,max} = k_1^{'} c_{Fe,max} + k_2^{'} \alpha_{max} \tag{3.4}$$

In fig. 3.12 for all the investigated samples the relative vertical mismatches are reported as a function of optical absorption coefficients and the expected linear relation between $\xi_{\perp,max}$, $c_{Fe,max}$ and α_{max} is confirmed by experimental data. According to this view, all the data in fig. 3.12 have been fitted using eq. 3.4 by a simultaneous least-squares minimization for the two parameters $k_1^{'}$ and $k_2^{'}$, considering as independent variables$\xi_{\perp,max}$ and $c_{Fe,max}$, because they have smaller experimental errors than α_{max}. The errors of the two parameters are then calculated by the standard error propagation rules, assuming statistical independence between the optical absorption errors and the concentration ones. The final values of the parameters relative to the concentrations of empty and filled traps are

$$\begin{aligned} k_1 &= (-1.29 \pm 0.17)\, x\, 10^{24}\, cm^{-3} \\ k_2 &= (-0.30 \pm 0.14)\, x\, 10^{24}\, cm^{-3} \end{aligned}$$

These values highlight that when iron is in its 2+ oxidation state it produces a lattice deformation which is several times lower than that induced by Fe^{3+} ion. This fact is not surprising considering that, as demonstrated in section 3.2 and 3.3, both Fe^{3+} and Fe^{2+} are located at the Li site, thus the charge difference between Li^{+} and Fe^{3+} ions

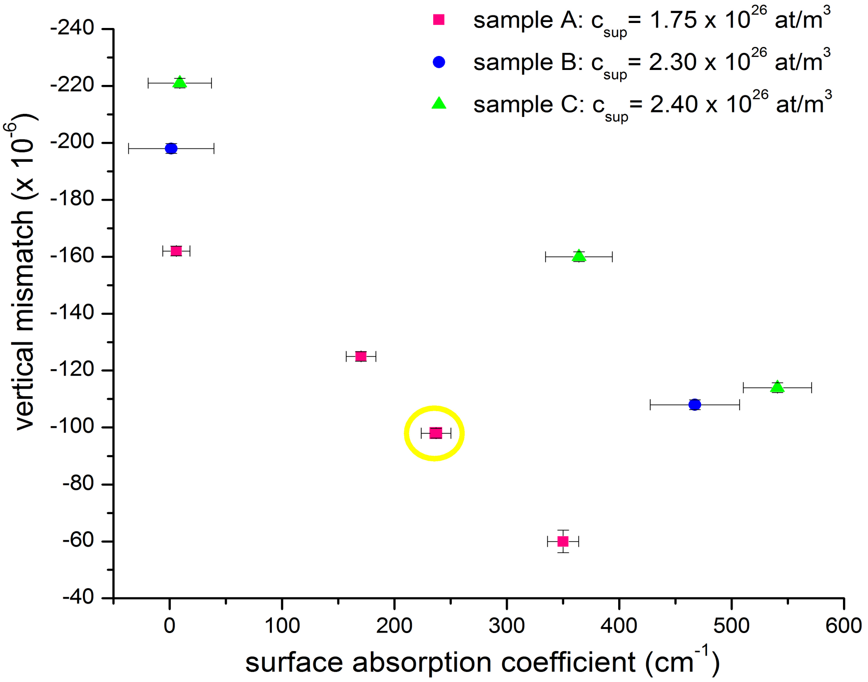

Figure 3.12: *Relative vertical mismatch as a function of the absorption coefficient calculated at the sample surface for the three samples and subsequent reduction treatments. The marked point indicates the effect of an oxidizing treatment performed after the second reduction on sample A. Often the error bars relative to the y coordinate are smaller then the size of the experimental point.*

is larger than with Fe^{2+} ones and consequently in the former case the surrounding O ions are attracted more strongly by the defect. However, it is also possible that the observed lattice deformation is induced, by mean of piezoelectric effect, by the electric field associate to the dipole constituted by the Fe defect and the other ions which compensate its charge. Therefore further calculations will be performed taking into account this last hypothesis.

In summary, all the above results have shown that the vertical mismatch of the doped layer is affected by the valence state of the dopant and that it can be tuned simply by a reducing treatments, without moving the Fe ion from their site. Finally, it has to underline that the reversibility of this effect has been proved, by re-oxidizing the sample A after the two reducing treatments. It was observed that after the re-oxidizing annealing (in O_2 at 500°C) the sample A presented not only, as expected, a reduced amount of Fe^{2+} and therefore a decreased absorption coefficient, but also a larger lattice deformation. The compression of the doped layer has been partially restored by the oxidizing process and the relative experimental point reported in fig. 3.12, and evidenced by a yellow circle, is perfectly aligned with the other data, confirming that the effect is reversible.

At the moment a local investigation of the optical properties of diffused samples is quite difficult with the standard optical technique, thus the above results are interesting above all because they could allow to derive separately the in-depth profiles of Fe^{2+} and Fe^{3}, whose knowledge would significatively help to achieve better understanding of the photorefractive phenomena in diffused samples. Indeed each rocking curve could be computationally simulated assuming that its final shape is obtained as the sum of a set of layer with different lattice mismatch, whose values gradually fall to zero going from the surface of the sample to the undoped substrate. In this way a mismatch profile would be derived and, by using eqs.3.2-3.4, also those ones relative to empty and filled traps. A simulation program devote to this study is being developed, but the complex crystallographic structure of the lithium niobate makes the work difficult. However, the results obtained with the new optical set-up described in the next chapter can surely help to reach this aim, opening a completely new world on the possibility to locally characterized sample realized by thermal diffusion.

Chapter 4

Experimental Study of Photorefractive Properties in Fe-diffused lithium niobate

In the last decades the interest in photorefractive materials has increased significatively, due to their unique optical properties which can be used for several applications in optics, such as *self-pumped phase conjugation*, *holographic gratings* for interference filters and *volume holographic memories.* Optical devices realized in lithium niobate crystals are still now considered a good alternative to conventional electronic system, since this material presents excellent photorefractive properties, that can be enhanced by iron doping.
Thus in the first part of this chapter the photorefractive properties of Fe:LiNbO$_3$ are discussed, with major attention to the band transport model with one photorefractive center. Then, in the last sections, we present an innovative set-up for holographic measurements able to study the photorefractive effect in diffused samples, where the dopant concentration is not constant all over the volume but it presents a in-depth profile.

4.1 Fundamentals of Photorefractive Effect

In 1966, at Bell Laboratories, Ashkin et al.[38] discovered a light-induced refractive index change in LiNbO$_3$ crystals. They observed a fanning of the light passing through the material and attributed this behaviour to a sort of laser induced damage, calling it *optical damage.* Only after some years a *band transport model* was proposed to explain this effect and in 1968 Chen[39] provided for it a theoretical formalism based on a set of rate equations for electrons and traps densities, recognizing the importance of the refractive index change for the storage of volume phase holograms. The effect observed by Ashkin is now known as *Photorefractive (PR) Effect*, which refers to a change of the refractive index of a material under illumination, as a result of the electro-optic effect. Under uniform illumination charge carriers are excited

$$I(\mathbf{r}) \rightarrow N_{e,h}(\mathbf{r}) \rightarrow \mathbf{j}(\mathbf{r}) \rightarrow \rho\,(\mathbf{r}) \rightarrow \mathbf{E}_{sc}(\mathbf{r}) \rightarrow \Delta n(\mathbf{r})$$

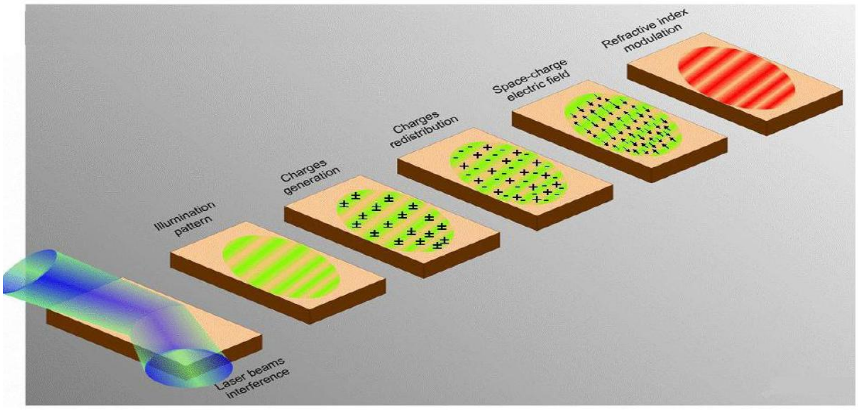

Figure 4.1: *The main steps of PR effect with a non-uniform illumination*

from localized state in the forbidden band to conduction (or valence) band, where they move until they are retrapped, then excited again and so on. But if an inhomogeneous illumination is used, a charge distribution between darker and brighter regions occurs, leading to the final buildup of a refractive index modulation, as illustrated in fig. (4.1) and summarized in the following main steps:

- a nonuniform illumination creates an intensity pattern and the donor centers of the material (N_D) are excited, generating free charge carriers (electrons or holes);
- the charge carriers migrate in the conduction or valence band due to *drift*, *diffusion* and *bulk photovoltaic effect* and a density current arises;
- when a charge carrier is trapped at an acceptor center (N_A) in a dark area, it can no longer move and therefore a charge redistribution between illuminated and dark regions is built up;
- the charge density spatial modulation induces an electric space-charge field, which acts against further charge transport, and finally a steady-state situation is achieved;
- thanks to the electo-optic effect the space-charge field affects the refractive index of the material, leading a refractive index modulation.

The influence of extrinsic centers on the photorefractive properties of $LiNbO_3$ was already known in the seventies. In particular transition metals, such as iron, were carefully investigated since they can be incorporated in lithium niobate in different valence states, acting as donors and acceptors and enhancing the PR effect in this material. Therefore in the following sections the present knowledge on the PR effect in Fe:LiNbO$_3$ is summarize, starting with a detailed description of the involved charge transport processes.

4.2 Charge Transport in Fe:LiNbO$_3$

The photo-induced charge carriers can move because of drift, bulk photovoltaic effect and diffusion, whose corresponding currents are denoted as $\mathbf{j}_{drift}$, $\mathbf{j}_{phv}$ and $\mathbf{j}_{diff}$. Therefore the total current arising in the material is the sum of these three contributions

$$\mathbf{j} = \mathbf{j}_{drift} + \mathbf{j}_{phv} + \mathbf{j}_{diff}$$

and it generally depends on spatial position and time.
Moreover for all charge transport models the Poisson and continuity equations

$$\nabla(\hat{\epsilon}\,\mathbf{E}) = \rho/\epsilon_0 \tag{4.1}$$

$$\nabla \cdot \mathbf{j} + \frac{\partial \rho}{\partial t} = 0 \tag{4.2}$$

must be fulfilled.

4.2.1 Drift current

The *drift current* derives from the Coulomb interaction between an electric field and the charge of the carriers, obeying Ohm's law

$$\mathbf{j} = \hat{\sigma}\mathbf{E} \tag{4.3}$$

$$\hat{\sigma} = q\hat{\mu}_{e,h}N_{e,h} \tag{4.4}$$

where $\hat{\sigma}$ is the conductivity tensor, $\mathbf{E}$ the electric field, q and $N_{e,h}$ respectively the charge and the density of the free charge carriers (electrons in the conduction band or holes in the valence band) and $\hat{\mu_{e,h}}$ is the mobility tensor. The electric field $\mathbf{E}$ consists of three contributions: *the externally applied electric field* $\mathbf{E}_0$, the *pyroelectric field* $\mathbf{E}_{pyro}$ and the *space-charge field* $\mathbf{E}_{sc}$, which originates from the redistributed charge carriers. In particular the pyroelectric field arises from a local heating of the crystal due to illumination, which causes a change in the spontaneous polarization $\mathbf{P}_s$ of the material. For small temperature changes ΔT the equation

$$\mathbf{E}_{pyro} = \frac{1}{\epsilon\epsilon_0}\frac{\partial \mathbf{P}_s}{\partial T}\Delta T \tag{4.5}$$

is valid and the electric field is opposite to the direction of $\mathbf{P}_s$. However this field is usually negligible in holographic experiments performed in Fe:LiNbO$_3$ with low intensity ($<10^5$ W/m^2)[4].

4.2.2 Bulk photovoltaic current

The *bulk photovoltaic effect* is a mechanism typical for non-centrosymmetric crystals due to an asymmetric charge transfer from the absorbing center to the neighboring ions during optical excitation. Indeed in these materials the charge carriers are excited with a preferred momentum and only when they are thermalized they loose their directional properties, contributing to drift and diffusion currents but not more to photovoltaic one. This effect was discovered in 1974 by Glass et al. that observed in lithium niobate crystals exposed to light a stationary current[40], proportional to light intensity and to the absorption coefficient of the material.
This density current, named *bulk photovoltaic current*, is expressed as

$$j_{phv,i} = \beta_{ikl}\, e_k\, e_l^\star \tag{4.6}$$

where $\hat{\beta}$ represents the complex photovoltaic tensor, e_k and e_l are components of the light field **e** and $\beta_{ikl} = \beta_{ilk}^\star$ with i,k,l=1,2,3. Generally the real and imaginary parts of the photovoltaic tensor are, respectively, symmetric and antisymmetric in the indices k and l; moreover for a linearly polarized light wave only the real part of β_{ikl} is taken into account, on the contrary for circular polarization also the imaginary part is involved. For $LiNbO_3$, whose space and point groups are R3c and 3m, the photovoltaic tensor has four nonvanishing independent components: β_{333}, $\beta_{311} = \beta_{322}$, $\beta_{222} = -\beta_{112} = -\beta_{121} = -\beta_{211}$ and $\beta_{113} = \beta_{131}^\star = \beta_{232} = \beta_{223}^\star$.
The largest current densities are obtained along the **c**-axis, but currents perpendicular to **c**-axis have been also identified, even if they are order of magnitude smaller. Often the photovoltaic current along the **c**-axis is written in the scalar form

$$j_{phv}/I = \alpha k_G = \mu \tau_{phv} E_{phv} \alpha / h\nu \tag{4.7}$$

where α is the absorbing coefficient and k_G is a constant describing the anisotropy of the charge transport, called *Glass constant*, which for $Fe:LiNbO_3$ is 2.8 x 10^{-11} m/V. Moreover μ is the mobility of the charge carriers, τ_{phv} the time within which excited carriers contribute to photovoltaic charge transport, $h\nu$ the energy of the incident photons and E_{phv} is a *phenomenological introduced* field acting on the charge carriers.

4.2.3 Diffusion current

If a spatially fluctuation of the concentration of charge carriers is built up, a diffusion current arises and it is described as

$$\mathbf{j}_{diff} = -q\hat{D}\nabla N_{e,h} \tag{4.8}$$

$$\hat{D} = \hat{\mu}_{e,h} k_B T/q \tag{4.9}$$

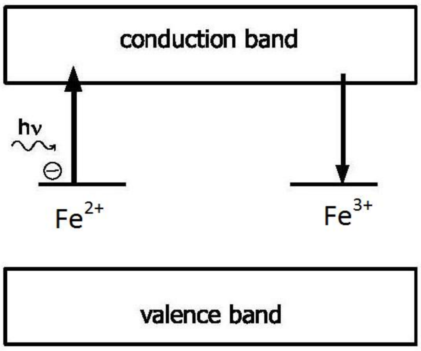

Figure 4.2: *Band scheme of the one center charge transport process: an incident photon excites a trapped electron to the conduction band where it migrates due to drift, diffusion or photovoltaic effect until it is retrapping in an empty center.*

where $\hat{D}$ is the diffusion tensor and q refers to -e or +e respectively for electrons or holes.

In 1980 an alternative model to the band charge transport model was proposed by Feinberg et al.[41]. In this new model, called *hopping model*, when a material is exposed to optical illumination a direct tunneling of electrons and holes from one site to another is taken into account as transport mechanism. However, in the limit of zero external field E_0, as it will be in our case, both the hopping and the band transport models lead to the same results. Therefore in the following only the band transport model will be considered, since it is more general and detailed treated in literature.

4.3 The one-center model

The *one-center charge-transport model* was the first model developed at the beginning of the studies on photorefractive effect and it still holds for many situations. Equations considering generation and recombination of charge carriers were already proposed by Amodei in 1971, but only four years later Vinetskii and Kukhtarev[42] introduced a first complete set of rate equations which took into account also concentration for filled and empty traps. In this model only a single type of photorefractive center is considered, which presents two possible valence state acting as either donor or acceptor for the carriers. This is also the case of iron which can be incorporated in lithium niobate with the possible valence state Fe^{2+} and Fe^{3+}, behaving respectively as filled or empty trap. The one-center model is illustrated in fig. (4.2) and the evolution of the system is governed by the following set of equations:

$$\frac{\partial N_{e,h}}{\partial t} = (s\,I + \beta_T)\,N_{Fe^{2+}} - \gamma_{e,h}\,N_{e,h}\,N_{Fe^{3+}} - \frac{1}{q}\nabla\cdot\mathbf{j} \tag{4.10}$$

$$\frac{\partial N_{Fe^{2+}}}{\partial t} = -\frac{\partial N_{Fe^{3+}}}{\partial t} = -(s\,I + \beta_T)\,N_{Fe^{2+}} + \gamma_{e,h}\,N_{e,h}\,N_{Fe^{3+}} \tag{4.11}$$

$$\mathbf{j} = q\,\mu_{e,h}\,N_{e,h}\,\mathbf{E} - q\,D\,\nabla N_{e,h} + s\,N_{Fe^{2+}}\,k_G\,I \tag{4.12}$$

where q and $N_{e,h}$ are respectively the charge and the density of the carriers (electrons or holes), s the photoionization cross section, $\gamma_{e,h}$ the recombination constant, $\mu_{e,h}$ the mobility, $\mathrm{D} = \mu \mathrm{K}_B \mathrm{T}/\mathrm{q}$ the diffusion coefficient with k_B the Boltzmann constant and T the absolute temperature, k_G is the Glass constant, β_T the thermal generation rate and $\mathrm{N}_{Fe^{2+}}$ and $\mathrm{N}_{Fe^{3+}}$ the concentrations of filled and empty centers. Moreover in (4.12) the total current density includes the drift, diffusion and photovoltaic contributions described in the previous section and the electric field **E** refers to externally applied and space charge ones.
Finally the space charge field must obey the poisson equation

$$\nabla \cdot (\hat{\epsilon}\,\epsilon_0\,\mathbf{E}_{sc}) = \rho = q\,(N_{e,h} + N_{Fe^{2+}} - N_{Fe^{2+}}(0)) \tag{4.13}$$

where $N_{Fe^{2+}}(0)$ is the concentration of donors in absence of illumination.

Usually the concentration of the free carriers ($\approx 10^{14}$ m^{-3}) is small compared to the typical concentration of photorefractive centers ($\approx 10^{24}$ m^{-3}) and therefore $N_{e,h}$ can be neglected in eq.(4.13). However in eq. (4.2) the time derivate of ρ occurs and the $\frac{\partial N_{e,h}}{\partial t}$ has to be considered. When the light is switched on, $N_{e,h}$ quickly rises and after it changes on the same time scale of $\mathrm{N}_{Fe^{2+}}$, since for constant light further changes of free carriers concentration result only from changing concentration of photorefractive donors and traps. In this second stage it holds the so-called *quasi-steady-state approximation* or *adiabatic approximation*, which states that under illumination $N_{e,h}$ reaches nearly instantaneously the equilibrium state and after this short time one can assume $\frac{\partial N_{e,h}}{\partial t}$=0, implying that charge carriers are at any time in equilibrium (quasi-equilibrium) with the traps distribution. The initial rise time of $N_{e,h}$ is in the ps scale for crystal of lithium niobate family ($\mathrm{LiNbO_3}$ an $\mathrm{LiTaO_3}$) and during this time interval the space-charge field built-up is not appreciable, so the adiabatic approximation can be used if the light pulse duration is longer than the rise time of $N_{e,h}$.
Moreover, in terms of the adiabatic approximation the relation $\frac{\partial N_{Fe^{2+}}}{\partial t}$=0 is valid, allowing a good estimation of the concentration of the charge carriers at any time and place from eq.(4.11):

$$N_{e,h} = \frac{(s\,I + \beta_T)}{\gamma}\,\frac{N_{Fe^{2+}}}{N_{Fe^{3+}}} \tag{4.14}$$

It is also important to note that assuming $\frac{\partial N_{Fe^{2+}}}{\partial t}$=0 does not mean that a steady-state situation has been reached, since it is present a small contribution $\frac{\partial N_{Fe^{2+}}}{\partial t} \neq 0$

that slowly builds up the spatial modulation of donors and acceptors concentration due to charge transport.
From eq.(4.4) the conductivity can be derived

$$\sigma = \sigma_{ph} + \sigma_{dark} = q\,\mu\,\frac{s\,I}{\gamma}\,\frac{N_{Fe^{2+}}}{N_{Fe^{3+}}} + q\,\mu\,\frac{\beta_T}{\gamma}\,\frac{N_{Fe^{2+}}}{N_{Fe^{3+}}} \tag{4.15}$$

showing the presence of two contributions: σ_{ph}, named *photoconductivity* and proportional to light intensity I, and σ_{dark}, called *dark conductivity* and caused by the thermal excitation of charge carriers without illumination. Both these types of conductivity depend on the reduction degree $\frac{Fe^{2+}}{Fe^{3+}}$, as confirmed by several experiments on Fe:LN samples with dopant concentration up to 20 x 10^{24} m^{-3}[43]. However for light intensity higher than 1 W/cm^2, thermal excitations are negligible and thus $\sigma_{ph} \gg \sigma_{dark}$.

4.3.1 Electrons-holes competition

Up to now both electrons and holes were considered as possible charge carriers. Indeed also excitation of holes is possible and they can migrate in the valence band, trapping electrons from a Fe^{2+} centers. Moreover not only one charge carrier type can dominate on the other, but they can also simultaneously be involved in the charge transport, as demonstrated by Orlowski and Krätzing[44], who showed in their paper as holography measurements can be used to determine the relative contribution of electrons and holes to the charge transport mechanisms. Indeed if two beams interfere in a photorefractive material the induced refractive-index pattern can be shifted respect to the light pattern and this phase shift is influenced by the sign of the charge carrier. The rule of electrons and holes depends not only on the dopant used in the material, but also on its reduction degree and on the wavelength of the incident light. In iron-doped lithium niobate for ultraviolet light the holes dominate in strongly oxidized crystals, while for more reduced ones the excitation of electrons prevails. On the contrary for visible light electrons play the major rule over the entire oxidation/reduction range of Fe:$LiNbO_3$ crystals[4, 44]. Therefore in experiments performed with green light, as it is the case of this thesis, electrons can be considered the only charge carriers involved in charge transport mechanisms ($N_{e,h}$=N_e and q=e).

4.3.2 The dark conductivity

Besides the photoconductivity the dark conductivity is another important property of photorefractive materials. While in the presence of illumination σ_{dark} is often negligible compared to σ_{ph}, on the contrary the space-charge field and, thus, the refractive-index pattern decay in the dark only because of the dark conductivity and this is a serious problem for all those applications where persistence of stored pattern is required.
Usually dark-storage times up to 1 year[45] are measured in low-doped Fe:$LiNbO_3$

with values of dark conductivity of about 10^{-16}-10^{-18} Ω^{-1}cm^{-1} at room temperature, but in crystals with large amount of iron the dark decay is accelerated and the storage time falls down to hours, minutes or seconds[46]. These different behaviours of the dark storage time in iron doped lithium niobate is due to the two different mechanisms involved in the dark decay: a protonic conductivity and an electrons tunneling between sites of Fe^{2+} and Fe^{3+} with no band transport. In particular the latter contribution was identified by Buse et co-workers[47], who systematically studied the relation between iron concentration and dark conductivity in Fe:$LiNbO_3$ crystals. In crystals with doping level less than 0.05wt% Fe_2O_3 the proton compensation, with an activation energy of about 1eV, dominates the dark decay and the time constant is inversely proportional to H^+ amount inside the material[1]. On the contrary for doping levels above 0.25wt% Fe_2O_3 the electron transfer occurring by tunneling prevails on proton conductivity, with an activation energy of 0.28eV[49], while for iron concentration between 0.05wt% and 0.25wt% Fe_2O_3 both the proton transport and electrons tunneling contribute to the decay of an hologram in absence of illumination. Above 70-80°C, when the proton mobility increases, the proton transport is always dominant, regardless of the impurity level. Moreover it was experimentally demonstrated that the dark conductivity depends on the effective traps density $N_{eff}=[1/N_{Fe^{2+}}+1/N_{Fe^{3+}}]^{-1}$[47], i.e. the reduction degree of the iron, and that in strong reduced Fe:$LiNbO_3$ crystal new effects arise due to the formation of polaron and bipolaron, which enhance the dark conductivity. Therefore, if on one hand doping lithium niobate with iron allows to obtain stronger photorefractive effects than in undoped crystals, on the other hand it is necessary to avoid high dopant concentrations (above 0.05-0.06wt%) and an its excessive reduction[47], otherwise a dark decay would be too fast.

4.3.3 Solution for non-homogeneous illumination

A simple way to produce an non-homogeneous illumination and to obtain information on the consequent buildup of the space-charge field is given by the interference of two plane waves, since in the case of the sinusoidal interference pattern created by two plane waves an analytical solution for the equations (4.10-4.12)can be derived. For simplicity in the following a one dimensional light pattern along the $\hat{z}$ axis will be considered.

The light intensity due to the superimposition of two plane waves with wave-vectors $\mathbf{k}_1$ and $\mathbf{k}_2$ and intensity I_1 and I_2 is:

$$I(z) = I_0\,(1 + m\,sin(\mathbf{K}\cdot\mathbf{z})) \tag{4.16}$$

where I_0 is the average intensity, m= $(I_{max} - I_{min})/(I_{max} + I_{min})$ is the modulation

---

[1] To determine the amount of H^+ present in congruent lithium niobate crystals the OH^- stretching bond is usually exploited and the intensity of the major absorption line near 3480 cm^{-1}[48] is measured

degree of light pattern, which represents the visibility of the pattern, $\mathbf{K} = \mathbf{k}_1 - \mathbf{k}_2$ is the spatial frequency and $\Lambda = 2\,\pi/K$ the period length of the light grating. The solution was first obtained by Kukhtarev et al.[50, 51], using the idea to develop in Fourier series all the quantities involved in the eqs.(4.10)-(4.12) that depend on the spatial coordinate. For small modulation degree m≪1 the k th Fourier terms decreases quickly with m^k, therefore only the zero- and first-order components can be considered and each variables can be written as $X(t) = X^{(0)} + X^{(1)}(t)\,e^{iKz}$ ($X \equiv$ n, $\mathrm{N}_{Fe^{2+}}$, $\mathrm{N}_{Fe^{3+}}$, E). In particular, in the case of the electric field, $E^{(1)}$ stands for the amplitude of the sinusoidal component (representing the space charge field) and, for convenience, $E^{(0)} \equiv E_0$ is set as the externally applied field. Substituting those sinusoidal expressions into equations (4.10)-(4.12) the following results are obtained:

$$E_{sc} \approx E^{(1)} = -\frac{E_0 + E_{phv} + i\,E_D}{1 + E_D/E_q - iE_0/E_q - iE_{phv}/E'_q} \tag{4.17}$$

$$E_{phv} = \frac{j_{phv}}{\sigma_{phv}} = \frac{k_G\,\gamma}{e\,\mu}\,N_{Fe^{3+}} \tag{4.18}$$

$$E_D = \frac{k_B\,T}{e}\,K \tag{4.19}$$

$$E_q = \frac{e}{\epsilon\,\epsilon_0\,K}\left(\frac{1}{N_{Fe^{2+}}} + \frac{1}{N_{Fe^{3+}}}\right)^{-1} \tag{4.20}$$

$$E'_q = \frac{e}{\epsilon\,\epsilon_0\,K}\,N_{Fe^{2+}} \tag{4.21}$$

where E_q and $\mathrm{E'}_q$ are space-charge limiting fields and E_D is the diffusion one. In particular the E_q field is the maximum amplitude of the space-charge field provide by electrons transport for a given spatial frequency of the light grating, that corresponds to a complete spatial separation of positive and negative charges captured by traps. It is important to note the presence of the imaginary unit i in front of the diffusion field, which indicates the presence of a $\pi/2$ phase-shift between the light pattern and E_D (fig. 4.3), whereas the photovoltaic field and the external one are in phase respect to the interferogram. Therefore, in absence of externally applied field if the diffusion mechanism prevails the space-charge field results proportional only to $\mathrm{i}\,\mathrm{E}_D$ (see eq.(4.17)), with its same phase-shift, while if E_D and E_{phv} are comparable a phase-shift less than $\pi/2$ occurs. However, usually in doped lithium niobate the photovoltaic effect dominates and so a E_{sc} in phase with the light pattern is built-up. Moreover solving the equations (4.10)-(4.12) yields time-dependent monoexponential laws for the buildup and the decay of the space-charge field, with a time constant

$$\tau_{sc} = \frac{1 + (E_D - i\,E_0)/E_M}{1 + E_D/E_q - iE_0/E_q - iE_{phv}/E'_q}\,\tau_M \tag{4.22}$$

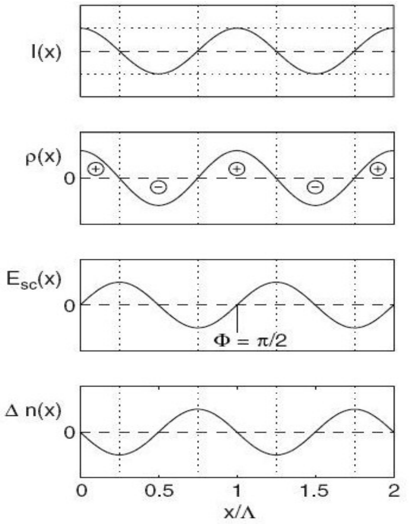

Figure 4.3: *Phase relation between the incident intensity pattern, the space-charge density, the builtup space-charge field and the refractive index modulation without externally applied field and for dominant diffusion mechanism.*

where

$$E_M = \frac{\gamma\, N_{Fe^{3+}}}{\mu}\,\frac{1}{K} \tag{4.23}$$

$$\tau_M = \frac{\epsilon\, \epsilon_0}{\sigma_{ph} + \sigma_{dark}} \tag{4.24}$$

Even in equation (4.22) an imaginary part is present, which is associated to the motion of the index fringes, and it causes oscillations on the evolution of the space-charge field. Moreover from eq.(4.24) it is evident as a significant dark conductivity can effect the time evolution of the system, leading a decresing of τ_M.

4.3.4 Simplified solutions

In many experiments some assumptions are easily verified and they can considerably simplify the formulas (4.17)-(4.24). These assumption are:

- No externally field is applied (E_0=0)
- No space-charge limiting effects are present, which means that there are enough filled and empty traps able to support the buildup of the space-charge field. Therefore $N_{Fe^{3+}}$ and $N_{Fe^{2+}}$ are to be large enough to ensure $E_q \gg E_D$ and $E'_q \gg E_{phv}$.
- The diffusion field has to be negligible compared to the photovoltaic field ($E_{phv} \gg E_D$). This assumption is ensured for sufficient dopant concentration and for grating that do not have small period length Λ, at room temperature.
- The above-mentioned assumptions imply also $E_M \gg E_D$ and $\tau_{sc} \simeq \tau_M$.

In this situation the time evolutions of the space-charge field during recording (eq. (4.25)) and erasing (eq. (4.26)) are:

$$E_{sc} = -E_{phv}\,(1 - exp(-t/\tau_{sc})) \tag{4.25}$$

$$E_{sc} = E_{sc,0}\,exp(-t/\tau'_{sc}) \tag{4.26}$$

where $E_{sc,0}$ is the value of the space-charge field at the begging of the erasure process and the saturation value of the E_{sc} is given by the bulk photovoltaic field.
Taking into account that for light intensity higher than 1W/cm^2 in Fe:LN $\sigma_{ph} \gg \sigma_{dark}$, some important dependences can be derived from the above analysis:

$$j_{phv} \propto I\,N_{Fe^{2+}} \tag{4.27}$$

$$\tau^{-1} \propto \sigma_{ph} \propto I\,(N_{Fe^{2+}}/N_{Fe^{3+}}) \tag{4.28}$$

$$\Delta n \propto E_{sc} \propto N_{Fe^{3+}} \tag{4.29}$$

where the saturation value of refractive index change Δn is related to E_{sc} by the electrooptical effect, obeying, for a field aligned along the optical axis of the material, to the following law:

$$\Delta n_{e,o} = -\frac{1}{2}\,n_{e,o}^{3}\,r_{13,33}\,E_{sc} \tag{4.30}$$

These dependences can be experimentally checked in order to verify the validity of the model used for the analysis and to obtain informations on some interesting material parameters.

4.3.5 The two centers model

The band transport model with one photorefractive center is able to described charge transport mechanism in Fe:LiNbO$_3$ if the light intensity is not too high, i.e. I<10^4 W/m^2, but it is not sufficient if laser pulse or focused cw laser light is used, reaching intensity higher than 10^6-10^7 W/m^2. Indeed at these high intensity new effects occur which contradict the relations (4.27)-(4.29), found in the frame of the one center model: light induced absorption changes, a superlinear relation between photoconductivity and light intensity and a refractive index change which depends on light intensity.
To explain these new phenomena a new simple approach was proposed considering a transport scheme which assumed the presence of a secondary photorefractive center, becoming active only at high intensity. In Fe:LiNbO$_3$ this second electron trap was identified to be the niobium antisite, Nb$_{Li}$, which acts in the forbidden band gap as *shallow center* with two possible valence states, Nb$_{Li}^{4+}$ and Nb$_{Li}^{5+}$. In 1993 a charge transport model with two photorefractive centers was proposed by Jermann and Otten[52], whose schematic representation is illustrated in figure (4.4), where Fe$^{2+/3+}$ are the deep centers. The rate equations which control this model are

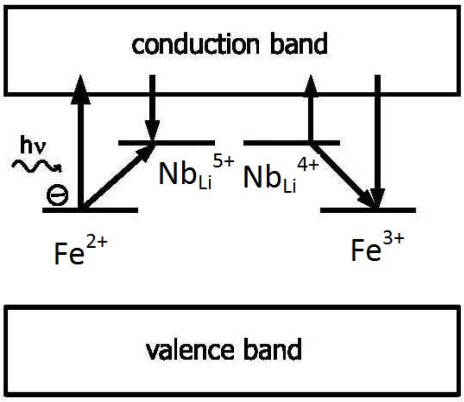

Figure 4.4: *Band scheme of the two centers charge transport process:* Fe^{2+} *and* Fe^{3+} *are the filled and empty deep traps, while* Nb_{Li}^{5+} *and* Nb_{Li}^{4+} *are the filled and empty shallow traps.*

$$\begin{aligned}\frac{\partial N_{\mathtt{Nb}_{\mathtt{Li}}^{4+}}}{\partial t} &= -\left[\beta_{\mathtt{Nb}_{\mathtt{Li}}} + s_{\mathtt{Nb}_{\mathtt{Li}}} I + \gamma_{\mathtt{Nb}_{\mathtt{Li}}\mathtt{Fe}}\left(N_{\mathtt{Fe}} - N_{\mathtt{Fe}^{2+}}\right)\right] N_{\mathtt{Nb}_{\mathtt{Li}}{}^{4+}} \\ &+ \left(\gamma_{\mathtt{Nb}_{\mathtt{Li}}} N_e + s_{\mathtt{FeNb}_{\mathtt{Li}}} I\, N_{\mathtt{Fe}^{2+}}\right)\left(N_{\mathtt{Nb}_{\mathtt{Li}}} - N_{\mathtt{Nb}_{\mathtt{Li}}{}^{4+}}\right)\end{aligned} \tag{4.31}$$

$$\begin{aligned}\frac{\partial N_{\mathtt{Fe}^{2+}}}{\partial t} &= -\left[s_{\mathtt{Fe}} I + s_{\mathtt{FeNb}_{\mathtt{Li}}}\left(N_{\mathtt{Nb}_{\mathtt{Li}}} - N_{\mathtt{Nb}_{\mathtt{Li}}{}^{4+}}\right) I\right] N_{\mathtt{Fe}^{2+}} \\ &+ \left(\gamma_{\mathtt{Fe}} N_e + \gamma_{\mathtt{Nb}_{\mathtt{Li}}\mathtt{Fe}} N_{\mathtt{Nb}_{\mathtt{Li}}{}^{4+}}\right)\left(N_{\mathtt{Fe}} - N_{\mathtt{Fe}^{2+}}\right)\end{aligned} \tag{4.32}$$

where the meaning of symbols are reported in table 4.1. Under illumination electrons

Table 4.1: *Symbols and their meanings used in the rate equations 4.31 and 4.32 describing the two-center model.*

Symbol	Meaning
$N_{\mathtt{Fe}^{2+}}$	concentration of $\mathtt{Fe}^{2+}$ ions
$N_{\mathtt{Fe}}$	concentration of $\mathtt{Fe}$ ions
$s_{\mathtt{Fe}}$	absorption cross section for absorption of an electron from $\mathtt{Fe}^{2+}$ to the conduction band
$\gamma_{\mathtt{Fe}}$	coefficient for recombination of an electron from the conduction band with $\mathtt{Fe}^{3+}$
$N_{\mathtt{Nb}_{\mathtt{Li}}{}^{4+}}$	concentration of filled shallow levels (Nb_{Li}^{4+})
$N_{\mathtt{Nb}_{\mathtt{Li}}}$	concentration of all shallow levels (Nb_{Li})
$\beta_{\mathtt{Nb}_{\mathtt{Li}}}$	thermal excitation rate of an electron from a filled shallow levels ($\mathtt{Nb}_{\mathtt{Li}}$) to the conduction band
$s_{\mathtt{Nb}_{\mathtt{Li}}}$	absorption cross section for absorption of an electron from $\mathtt{Fe}^{2+}$ to an empty shallow level (Nb_{Li}^{5+})
$\gamma_{\mathtt{Nb}_{\mathtt{Li}}}$	coefficient for recombination of an electron from the conduction band with an empty shallow level (Nb_{Li}^{5+})
$\gamma_{\mathtt{Nb}_{\mathtt{Li}}\mathtt{Fe}}$	coefficient for recombination of an electron from a filled shallow level (Nb_{Li}^{4+}) with $\mathtt{Fe}^{3+}$
N_e	concentration of electrons in the conduction band
I	light intensity

can be excited form Fe^{2+} either directly in the conduction band or into an empty shallow center Nb_{Li}^{5+}, forming a small polaron Nb_{Li}^{4+}. This mechanism induces a light absorption change $\Delta\alpha(\lambda)$, at a wavelength λ, which depends mainly on the polaron concentration

$$\Delta\alpha(\lambda) = (s_{Nb_{Li}} - s_{Fe})\, N_{Nb_{Li}^{4+}} \quad (4.33)$$

$$N_{Nb_{Li}^{4+}} = s_{FeNb_{Li}}\, I\, N_{Fe^{2+}} N_{Nb_{Li}}\, \tau\, [1 - exp(-t/\tau)] \quad (4.34)$$

$$\tau = \left[\beta_{Nb_{Li}} + \gamma_{FeNb_{Li}}\, N_{Fe^{3+}} + s_{Nb_{Li}}\, I\, (N_{Fe_{2+}} + N_{Nb_{Li}})\right]^{-1} \quad (4.35)$$

Considering the adiabatic approximation ($\partial N_e/\partial t = 0$), the rate equations give for electrons concentration in the conduction band

$$N_e = \frac{s_{\mathtt{Fe}}\, I\, N_{\mathtt{Fe}^{2+}} + (\beta_{\mathtt{NbLi}} + s_{\mathtt{NbLi}}\, I)\, N_{\mathtt{NbLi}^{4+}}}{\gamma_{\mathtt{Fe}}\, N_{\mathtt{Fe}^{3+}}} \quad (4.36)$$

which becomes eq. (4.14) for low intensity, when polaron concentration can be neglected. Moreover, remembering that $\sigma = \sigma_{phv} + \sigma_{dark} = e\,\mu\, N_e$ it follows that at hight intensities the photoconductivity has an additional quadratic intensity dependence, because the polaron concentration in eq.(4.36) increases with I.
Concerning the space charge field, it can be increased by the presence of filled shallow centers Nb_{Li}^{4+}. Indeed also the polarons contribute to the bulk photovoltaic transport[2] and, in the case of dominant photovoltaic effect, the space charge field is the sum of the photovoltaic fields induced by deep and shallow centers, respectively $E_{phv,Fe}$ and $E_{phv,Nb_{Li}}$. Thus, while for low intensity Δn is constant, on the contrary it increases with increasing intensity and values of about 3 x 10^{-3} can be achieved.

4.4 Holographic measurements

To study the photorefractive properties of a material a widely used method is the *holographic technique*, which allows to determine all the parameters involved in eqs. (4.17-4.26). This technique exploits the capability of a refractive index grating (or hologram)to behave as *diffraction grating*: indeed if a beam hits an hologram part of its light is diffracted, as shown in fig.4.5, with a diffraction angle which can be correctly predicted by simple geometrical considerations.
Photorefractive gratings are usually divided into several subclasses, but the most important distinction is between *thin* and *thick* holograms. A grating is considered thin if its thickness L satisfies the following condition:

$$L \ll \frac{\Lambda^2\, n\, cos(\theta)}{2\,\pi\,\lambda^2} \quad (4.37)$$

---

[2] For instance, at 532nm in $LiNbO_3$ the bulk photovoltaic coefficient of Nb_{Li}^{4+} is one order of magnitude larger than the bulk photovoltaic coefficient of Fe^{2+}[52].

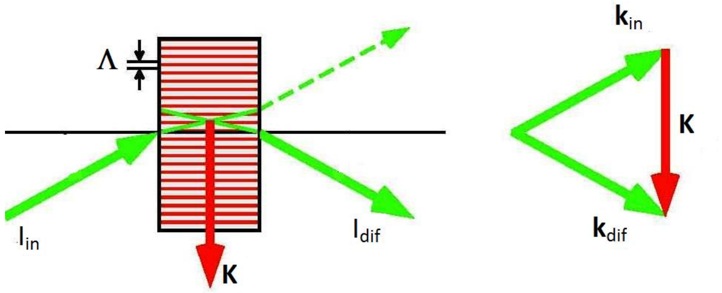

Figure 4.5: *Schematic representation of the diffraction of a beam which hits an holographic grating.* ***K*** *and* Λ *are respectively the spatial frequency and the period of the grating.*

where Λ is the period length, λ the light wavelength and θ the angle between the incident beam and the fringe planes inside the medium. In this case a wave that hits the grating will produce many partial waves that, at a certain distance from the hologram, may interfere in constructive or destructive manner, depending on their optical paths. So behind the hologram multiple diffraction orders will appear. On the contrary, if condition (4.37) is not satisfied, the grating is considered to be thick, only one diffraction order is present and strictly if the incident angle is chosen according to the *Bragg condition* $2\,sin(\theta) = \lambda/\Lambda$. In either case the intensities of the diffracted beams gives informations on same physical parameters of the grating, so the amplitudes of the diffracted waves can be found solving the Helmholtz equation and using different approaches. In particular for transmission thick holograms a suitable approach is the coupled-wave theory in the two wave approximation, as described by Kogelnik in his paper[53], which provides a relation between the diffraction efficiency of an holographic grating and the induced refractive index change

$$\eta \equiv \frac{I_d}{I_i} = sin^2\left(\frac{\pi\,\Delta n\,L}{\lambda\,cos(\theta)}\right)\,exp\left(-\frac{\alpha\,L}{cos(\theta)}\right) \tag{4.38}$$

where I_i and I_d are respectively the intensities of the incident and diffracted beams. This equation takes into account also the absorption of the incident light when it passes through the material; however this contribution can be neglected if I_i is replaced by the sum of the transmitted (I_t) and diffracted waves behind the hologram, obtaining

$$\frac{I_d}{I_t + I_d} = sin^2\left(\frac{\pi\,\Delta n\,L}{\lambda\,cos(\theta)}\right) \tag{4.39}$$

Moreover, if both I_t and I_d are symmetric respect to the geometry of the crystal, the above equation has the advantage that also the loss of intensity due to the reflections with the surfaces of the sample can be ignored.

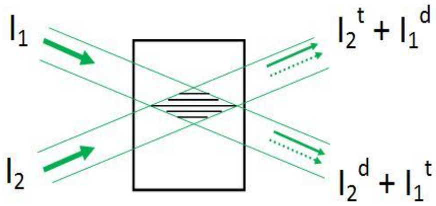

Figure 4.6: *Schematic representation of the interference of two beams in a photorefractive material. The holographic grating cause the diffraction of the incident beams, so behind the crystal each beam is the superimposition of two wave, a diffracted and a transmitted one*

Because the recording beams fulfills the Bragg condition, even during the recording of the grating part of the incident light is diffracted from one recording beam into the other one, so behind the crystal each beam is the superimposition of two waves, a diffracted and a transmitted one, as illustrated in fig. 4.6. Therefore by monitoring the time evolution of one of the diffracted beam during the recording mechanism it is possible to study the building-up of the grating and the dynamics of the photorefractive process.

4.5 Set-up for holographic measurements in diffused Fe:LN

In this section we present a new set-up which can be used to perform holographic measurements for the first time on diffused iron doped lithium niobate crystals.
Usually holography is realized in bulk crystals, where the dopant concentration is uniform on the whole volume, and so all the photorefractive properties mentioned in the previous sections were obtained in bulk Fe:LiNbO$_3$ crystals. Bulk doped materials have the advantage that they can be easy characterized with holographic measurements since both strong restrictions on the sizes of the light intensity pattern are not required and the holograms can be recorded in any area of the crystal without distinction. On the contrary this work is include in a project which counts to realized holographic gratings in a diffused Fe:LiNbO$_3$ crystal, so we will investigate samples that have dopant concentrations varying along the diffusion direction ($\hat{x}$ axis) and, therefore, also the physical properties involved in the photorefractive effect have a in-depth dependence. Thus, to characterize the doped layer by holographic measurements the sample is mounted with the $\hat{y}$ axis parallel to direction along which beams propagate and vertical scans (along $\hat{x}$ axis) are performed, as illustrated in fig.4.7, probing areas with different dopant concentration. In this configuration it is fundamental to be able to create holograms with a confined size along the vertical direction $\hat{x}$, so the area where the interference of the two incident beams occurs has to be vertically limited. In this way only a small part of the doped area can be investigated and in-depth profiles of a certain physical property can be obtained by performing scans along the direction of iron diffusion. On the contrary, since the iron concentration does not vary along the $\hat{y}$ and $\hat{z}$ directions, in holographic experiments

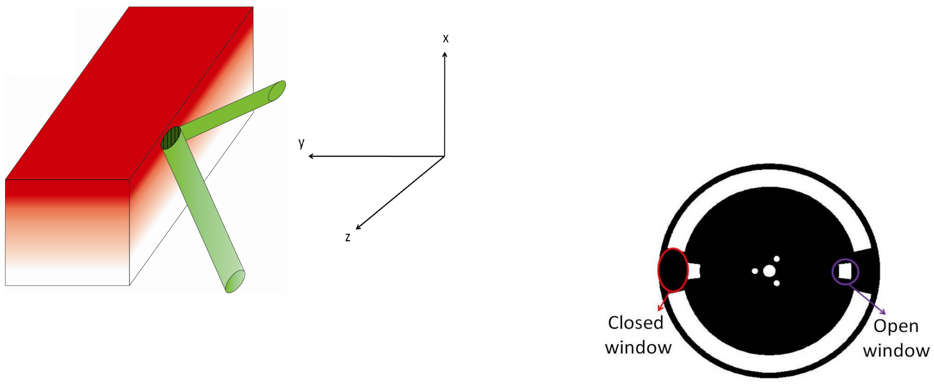

(a) (b)

Figure 4.7: *In (a) it is represented as the sample is mounted respect to the directions of the incident beams. In (b) the asymmetric chopper is shown:only when the closed window of the chopper stops beam 1, the beam 2 can passes through the open window and reaches the detector*

on diffused samples there are not constrains concerning the transverse size of the area where beam interfere, while its longitudinal size has only to satisfy the condition for thick gratings mentioned in the previous section.

To this aim a new set-up was realized and charcaterized in this thesis work: the set-up couples a standard two beam holographic scheme with a microscope objective, to realize spatially resolved photorefractive measurements. A schematic representation of the set-up, mounted in an optical table with non-isolating supports, is reported in figure 4.8. A diode-pumped solid state laser at 532nm is used as light source: the output beam has a power of 173 mW and a diameter of 2mm, with a coherence length longer than 10m. In front of the laser a round continuously variable neutral density filter is mounted in order to obtain a first attenuation of the laser beam. Then a couple of spherical lenses L_1 and L_2 (diameter $=$ 25mm, focal lengths $f_1 = 50$mm and $f_2 = 100$mm) are used to expand the beam obtaining a diameter of about 4mm. After the expansion the beam passes through another optical density filter[3] and then enters in a Mach-Zehnder similar interferometer, realized with two non polarizing beam splitter cubes (BS_1 and BS_2) and two mirrors (M_2 and M_3). After the first beam splitter a continuously variable attenuator is used to adjust the intensity I_1, so that behind the second beam splitter both the two beams have the same intensities ($I_1 = I_2$). When the two beams come out from the beam splitter BS2 they are slightly divergent, but, after passing through an horizontal polarizer, they are made parallel by a cylindrical plano-convex lens (focal length $f_3 = 120$mm). The cylindrical lens directs the light in a objective lens with magnification 40x (O 40x), which focuses the two beam on the sample. The sample holder is mounted on a 3-axes translation system (minimum step of 10 μm), equipped in addition with a tilt and rotation stage.

Since in this experiment vertical scans will be performed, we are interesting above

---

[3] Filters with different optical densities are used in this location, so it is possible to perform a systematic study of photorefractive properties varying the light intensity. The optical densities used are: 0.3, 0.5, 0.8, 1 and 1.3.

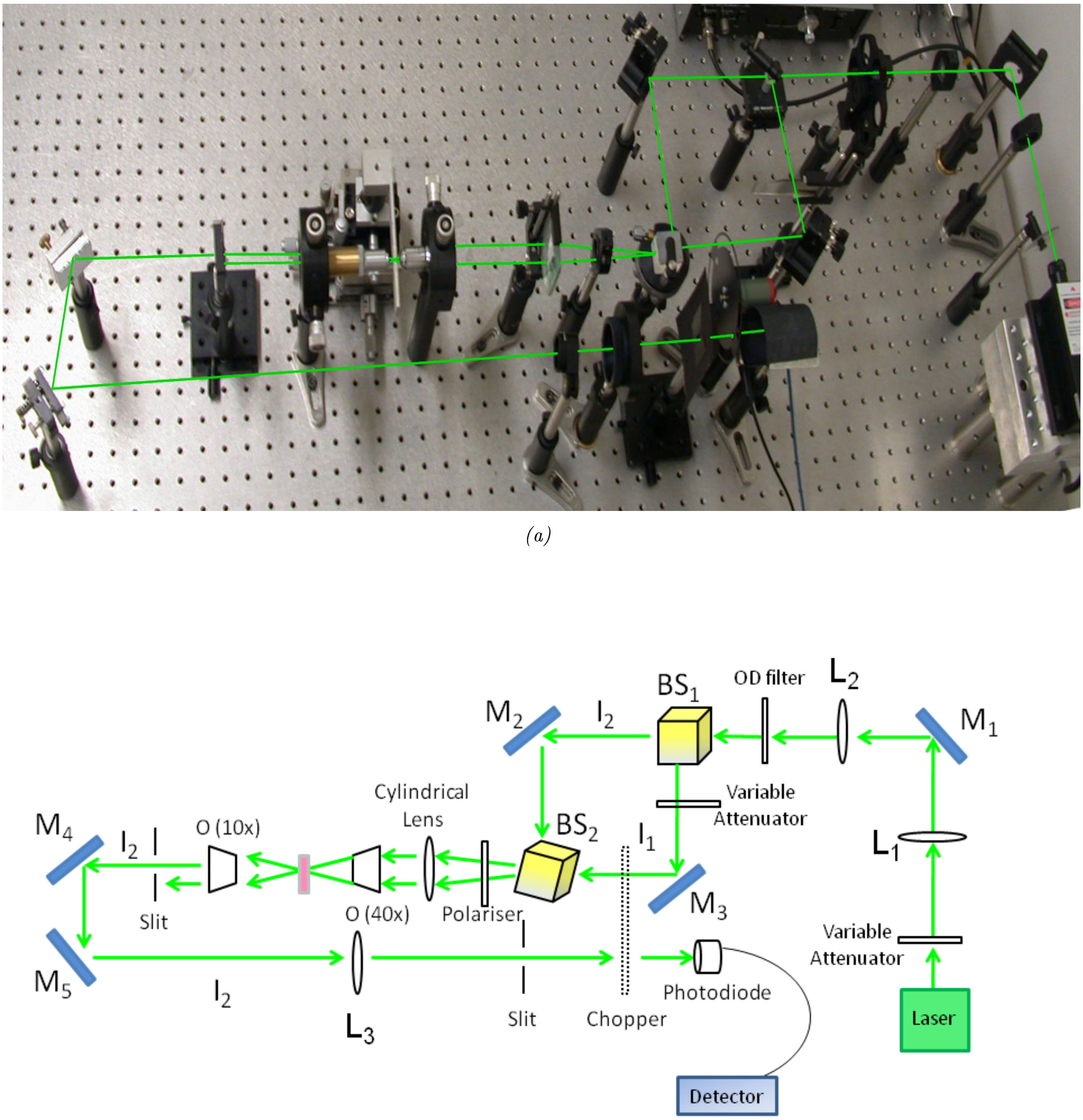

(a)

(b)

Figure 4.8: *Photo (a) and schematic representation (b) of the set-up used for holographic measurements in diffused Fe:LN samples.*

all to obtain in the focus of the objective vertical beam waists ω_1^v as small as possible, therefore each beam at the entrance of the objective has to have a large vertical waist ω_0^v [4]. However the waist ω_0 is limited by the geometrical size of the objective and by the necessity to have as input two beams well separated. A good compromise is found by using a cylindrical lens. Indeed the cylindrical lens has the property to focus the light which crosses it on a line and not on a point as spherical lenses: in particular in this set-up the two beams are compressed in the horizontal direction, while they are leaved unaltered in the vertical one. In this way in front of the objective the beams appear as two vertical lines which can be easily spaced in the horizontal plane and which have the maximum vertical waist allowed by the geometrical sizes of the entrance of the objective. To collect the light behind the sample an objective lens with magnification 10x (O 10x) is used and the two beams are directed to a spherical lens L_3 (f_4=150mm) by two mirrors. After the spherical lens the beams are enough small to enter in an asymmetric chopper (fig.4.8), which is mounted so that only if its *closed window* stops the beam 1 then the intensity (diffracted or transmitted) of beam 2 passes through its *open window* , reaching a silicon photodetector[5]. Finally two slits, located respectively behind the collecting objective and the last spherical lens, allow to select either I_2^d or I_2^t, monitoring their time evolution during the build-up of the hologram.

4.5.1 Set-up characterization

Since in this experiment focused gaussian beams are used, the light intensity distribution inside the interference area is not constant, but it varies at each point of the space and, consequently, also the dynamics of the holograms creation change. So in the following the term *probe* will represent the area inside the beams overlapping zone which will more contributes to the build-up of an induced refractive index change, that is also the area where the photorefractive properties of the material will be studied. Therefore to correctly analyze and understand the results that will be obtained, first of all it is necessary to know the size of the probe, determining in this way important parameters of the hologram,such as the fringes period, the incident intensity and the spatial resolution of our measurements.
Since the probe inside the sample is spatially limited by the area where the two incident beams overlap, which is the zone where their interference occurs, the *knife-edge technique* was performed to find first the angle between beams and their diameters in air, then their relative values in the material. In this technique a knife edge is used to slowly block the laser beam and the intensity of the forward light is measured as a function of the edge position. For each position of the knife edge along the $\hat{y}$ axis, scans along $\hat{x}$ and $\hat{z}$ directions were performed, obtaining intensity curves like that reported in figures (4.9 - 4.10). These curves were fitted with the error function

---

[4] When a gaussian beam passes through a lens of focal length f, the relation $\omega_1 = \frac{\lambda}{\pi \omega_0} f$ is observed[54]

[5] When I_2^t is measured, an optical density filter is necessary to avoid the detector saturation. Thus before the spherical lens a filter with OD=1.3 is mounted on a 90°-flip support.

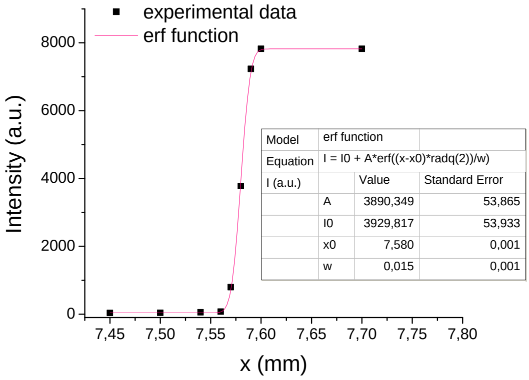

Model	erf function		
Equation	I = I0 + A*erf((x-x0)*radq(2))/w)		
I (a.u.)		Value	Standard Error
	A	3890,349	53,865
	I0	3929,817	53,933
	x0	7,580	0,001
	w	0,015	0,001

Figure 4.9: *Intensity as a function of the razor position along the $\hat{x}$ axis ($y = 2.83mm$). The experimental data are fitted with the error function efc((x-x0)·$\sqrt{2}$/w).*

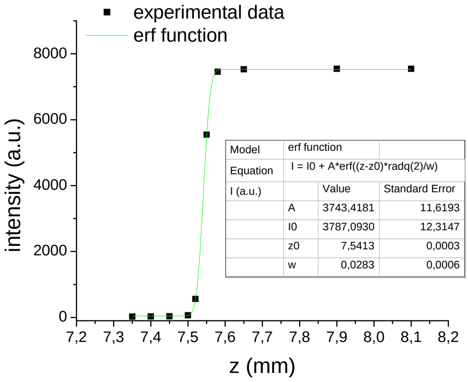

Model	erf function		
Equation	I = I0 + A*erf((z-z0)*radq(2)/w)		
I (a.u.)		Value	Standard Error
	A	3743,4181	11,6193
	I0	3787,0930	12,3147
	z0	7,5413	0,0003
	w	0,0283	0,0006

Figure 4.10: *Intensity as a function of the razor position along the $\hat{z}$ axis ($y = 2.5mm$). The experimental data are fitted with the error function efc((z-z0)·$\sqrt{2}$/w).*

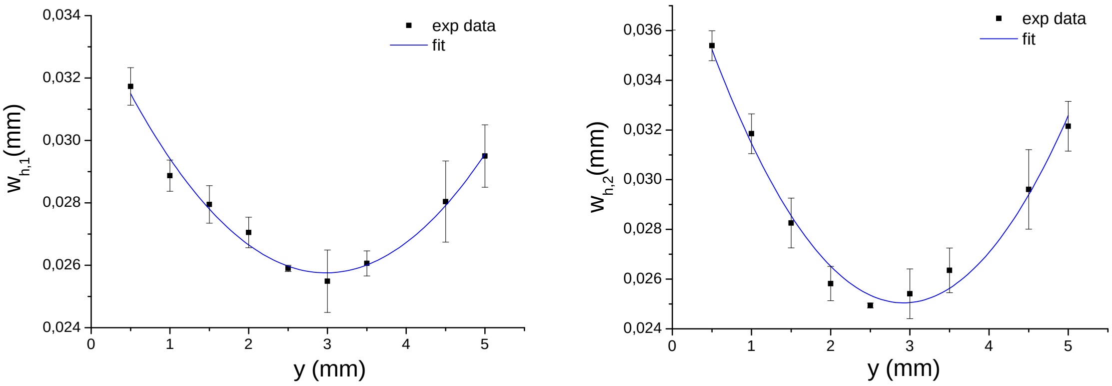

Figure 4.11: *Variation of the horizontal waist of beam 1 (left) and beam 2(right) along the $\hat{y}$ axis. The experimental data are fitted with the parabola function.*

(erf) which allows to determine the centers (x_0 and z_0) and the waist radii[6] (ω_v and ω_h) of the two beams, respectively in the vertical and horizontal planes, for each y position. All the values obtained by this analysis were plotted as a function of the razor position along the $\hat{y}$ axis, determining in this way the minimum waist radii achievable with the present set-up and verifying the alignment of the two beams. Moreover it has to be checked that the beams cross each other at the focal length of the objective, where their waist radii are minima and therefore also the probe has the smaller possible sizes. Several complete characterizations were performed until reaching the correct alignment, whose final results are discussed in the following.
From the experimental data reported in figures (4.11- 4.12) by using a parabola function it was possible to determine the minimum value of both the vertical and the transversal beam radius and their position along the $\hat{y}$ axis (see table 4.2). Within the errors ω_v and ω_h have the same minimum values and the Rayleigh range[7], which

---

[6] For more details see Appendix A

[7] For a gaussian beam the Rayleigh range r is give by the relation $r = \frac{\pi\, \omega_0^2}{\lambda}$ where ω_0 and λ are respectively the minimum waist and the wavelength of the beam. For more details see the Appendix

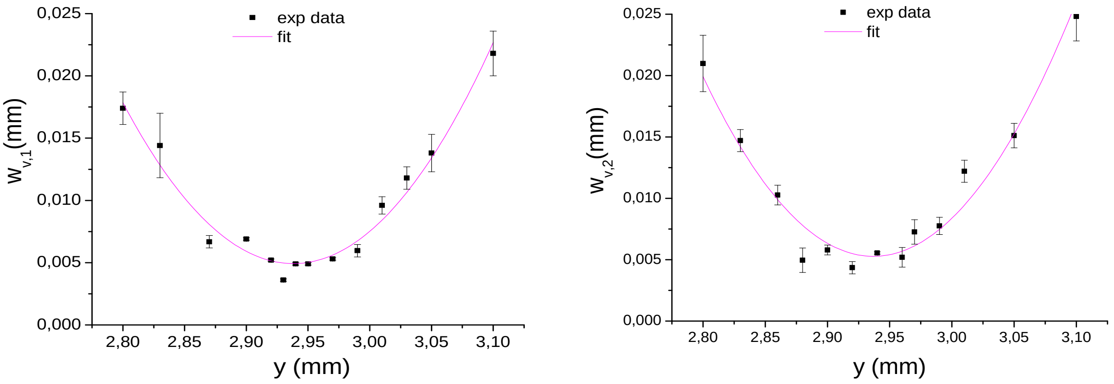

Figure 4.12: *variation of the vertical waist of beam 1 (left) and beam 2 (right) along the $\hat{y}$ axis. The experimental data are fitted with the parabola function.*

is the distance within which the beam radius lies within a factor $\sqrt{2}$ of its minimum value, is $r_v = (154 \pm 42)\,\mu$m and $r_h = (3.8 \pm 0.1)$ mm respectively, as confirmed by the experimental data. Moreover it is important to notice that the two beams are focused at the same y position, condition which occurs only if the beams enter into the objective parallel to each other. In fig. (4.13) the vertical and horizontal position of the beam center is reported as a function of the razor position, showing that the two beams lie in a horizontal plane located at 7,58 mm on the vertical scale of the translation stage, where the sample will be mounted. The angle between the beams, in air, and the y coordinate where they cross can be derived from linear fits of the data on the left

	minimum value (μm)	position (mm)
$\omega_{v,1}$	$4{,}9 \pm 0{,}4$	$2{,}94 \pm 0{,}01$
$\omega_{v,2}$	$5{,}3 \pm 0{,}6$	$2{,}93 \pm 0{,}01$
$\omega_{h,1}$	$25{,}7 \pm 0{,}2$	$2{,}98 \pm 0{,}04$
$\omega_{h,2}$	$25{,}0 \pm 0{,}3$	$2{,}92 \pm 0{,}04$

Table 4.2: *Minimum values and their relative position on $\hat{y}$ axis for the vertical and the transversal waists of the two beams.*

$$z_{0,1} = (0.120 \pm 0.001) \cdot y + (10.233 \pm 0.003) \tag{4.40}$$

$$z_{0,2} = (0.121 \pm 0.001) \cdot y + (10.944 \pm 0.002) \tag{4.41}$$

obtaining $2\theta_{air} = (13{,}50 \pm 0{,}01)^\circ$ and $y_{cross} = (2{,}95 \pm 0{,}01)$ mm, which is the same position where the beams are focused, as seen before, reaching their minimum waists.

In summary, after the focusing objective the two beams cross each other in the focal length, where the average vertical beam radius is $(5.1 \pm 0.7)\,\mu$m and the horizontal one is $(25.4 \pm 0.4)\,\mu$m. In particular the vertical beam diameter ((10.2 ± 1.4)) is

---

A.

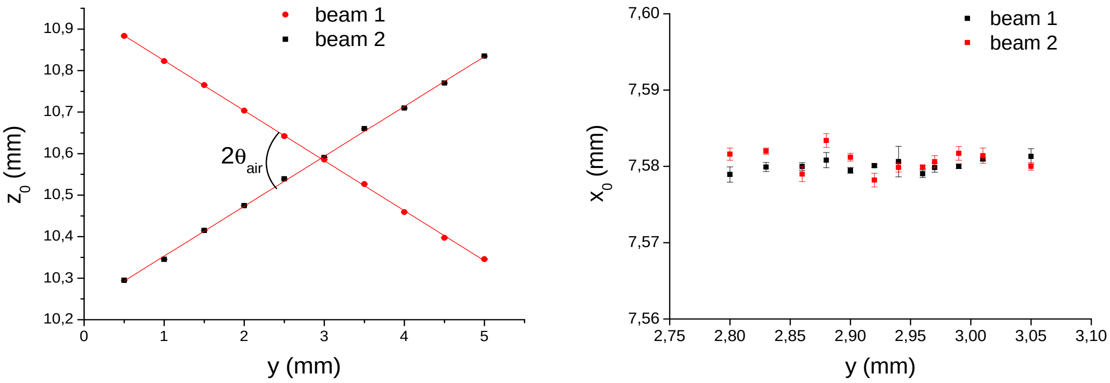

Figure 4.13: *Horizontal (z_0 on the left) and vertical (x_0 on the right) positions of the beam center as a function of the razor position along the $\hat{y}$ axis. Error bars are reported, but often they are smaller than the point size of experimental data.*

small enough to perform holographic scans along the iron concentration profile, probing areas with different amount of dopant. Moreover, taking into account the law of refraction it is possible to calculate the angle between beams inside the crystal, $2\theta_{in} = (5.89 \pm 0.01)°$, and by using simple geometrical considerations the longitudinal (d_1) and transversal (d_2) sizes of the area where they superimpose, which are $d_1 = (983.6 \pm 15{,}9)\,\mu$m and $d_2 = (50.6 \pm 0.8)\,\mu$m.

Remembering also as the sample is mounted respect to incident beams, fig. 4.7, and that the beams lie in a horizontal plane, it follows that the spatial frequency $\mathbf{K}$ of the grating is parallel to the $\hat{z}$ axis of the crystal. Therefore the absolute value of $\mathbf{K}$ and the relative grating period Λ inside the sample are

$$K = 2\left(\frac{2\,\pi}{\lambda}\right) sin\,(\theta_{in}) = (1.22 \pm 0.07) \cdot 10^6\,m^{-1} \tag{4.42}$$

$$\Lambda = \frac{2\,\pi}{K} = (5.15 \pm 0.30)\,\mu m \tag{4.43}$$

Finally, the light power after the objective 40x was fixed to 0,17 mW, so, considering the Fresnel transmittance coefficient and the beams sizes, inside the sample the light power is about 0,15 mW and the maximum incident intensity, which occurs in the focus, is $I = (35 \pm 4) \,x\, 10^4\,W/m^2$.

4.5.2 Probe sizes simulation

In the previous section the geometrical sizes of area where the beams superimpose were found, confirming that by using this set-up a tightly confined interference zone is obtained in the vertical direction. However, also the intensity distribution inside this area is important, since, as mentioned before, the time evolution of the photorefractive effect depends on I. Therefore starting from the values obtained with the experimental characterization of the set-up, computational simulations, performed by dr. N. Argiolas, of the intensity distribution inside the beams overlapping area were performed, in order to better understand the 3D shape of the probe, that is the part of the interference zone which more contributes to the rising of the hologram.

Considering two symmetric gaussian beams which propagate along $\hat{y}$ axis with Rayleigh range r$_o$ and equation

$$A(x,y,z) = A_0\, exp\left(-\frac{\rho^2}{\omega(y)^2}\right) exp\left\{-i\left[k\,y - tg^{-1}\left(\frac{y}{r_0}\right)\right]\right\} \tag{4.44}$$

$$A_0 \equiv A \cdot \frac{\omega_0}{\omega(y)} \tag{4.45}$$

$$I = A_0^2 \tag{4.46}$$

$$\rho = \left(x^2 + z^2\right) \tag{4.47}$$

their interference results

$$I_{tot} = (A_{0,1} + A_{0,2})^2 = A_{0,1}^2 + A_{0,2}^2 + 2\,(A_{0,1}\,A_{0,2})\; cos\,(\varphi_1 - \varphi_2) \tag{4.48}$$

where φ_1 and φ_2 are the phases of the two beams. Since φ_1 and φ_2 are not known, the spatial modulation of total intensity I$_{tot}$ can not be calculated, but this problem can be partially solved replacing the last term of eq. (4.48) with $2\sqrt{I_1\,I_2}$: in this way only an average intensity distribution inside the overlapping area is considered, losing the information on the intensity pattern. However, the purpose of this study is the determination of the volume within which the photorefractive effect occurs, so if this replacement does not change the final shape of the simulated probe this solution can be considered a good compromise. So before going along with this analysis it was verified that, apart from the sinusoidal component, $2\sqrt{I_1\,I_2}$ and

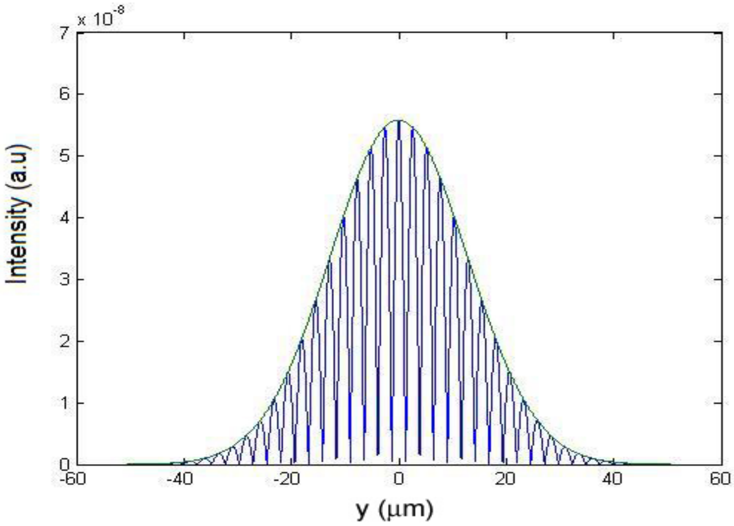

Figure 4.14: *Simulation of* $2\sqrt{I_1\,I_2}$ *(green line) and* $[2\,(A_{0,1}\,A_{0,2})\;cos\,(\varphi_1 - \varphi_2)]$ *(blu line) in the case of two symmetric gaussian beam that interfere*

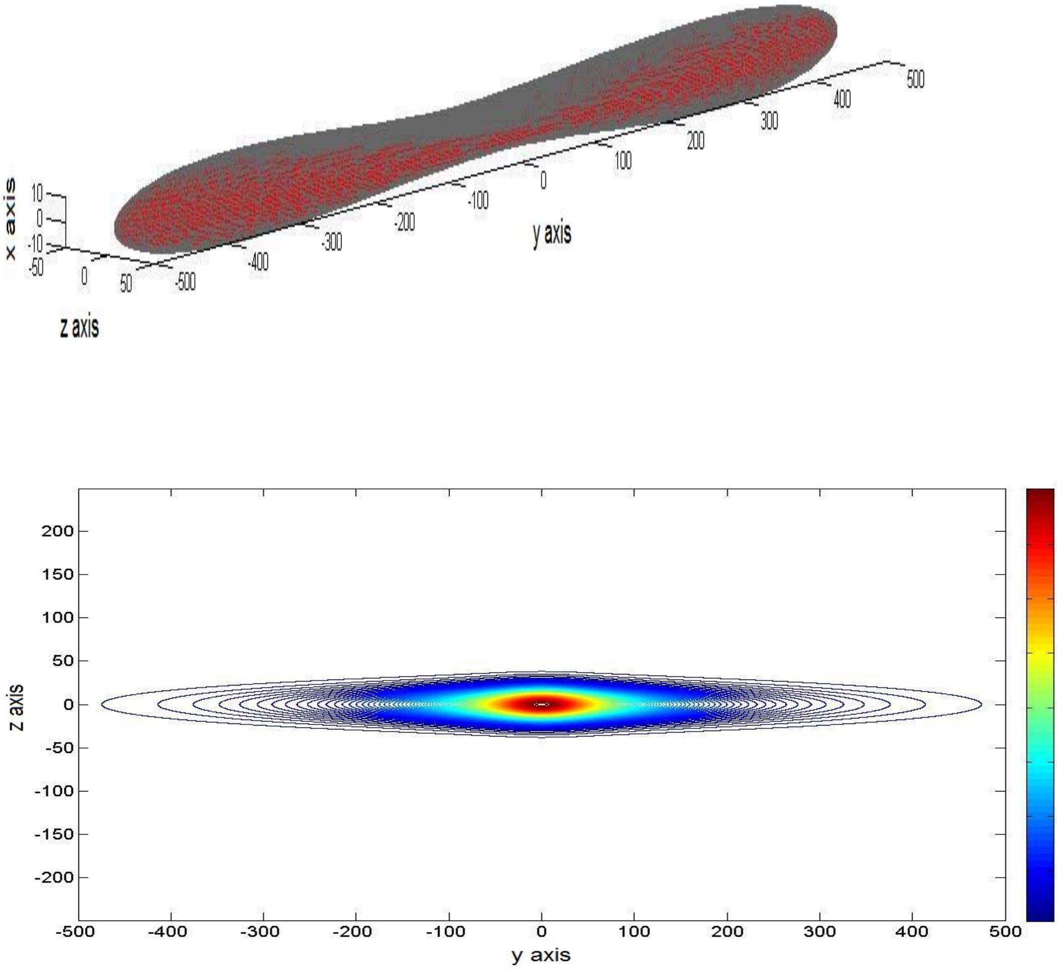

Figure 4.15: *Three-dimensional shape (a) and projection in the plane $x = 0$ (b) of the volume where the two beams superimpose . The units of measurement of the three axes are μm.*

$2[(A_{0,1}\, A_{0,2})\ cos\,(\varphi_1\ -\ \varphi_2)]$ give the same curve, as confirmed by the results reported in fig. 4.14, where the first term appears as a convolution of the second one.

The next steps were the calculation of the the intensity distribution produced by the interference of two elliptic and focused gaussian beams, as that used in the experiments. In all the simulations as minimum beam radii, angle between incident beams and intensity in the focus were used the values obtained by the previous experimental characterization, while the waists and the intensities at each point (x,y,z) were calculated by using the relation for gaussian beams illustrated in Appendix A. In fig. 4.15 the three-dimensional shape of the volume where beams superimpose is shown: this volume has a needle-like shape, stretched in the longitudinal directions and confined in the other ones, which is very constricted in the focus of the two beams. In the same figure it is also reported a projection of the interference volume in the plane x = 0,

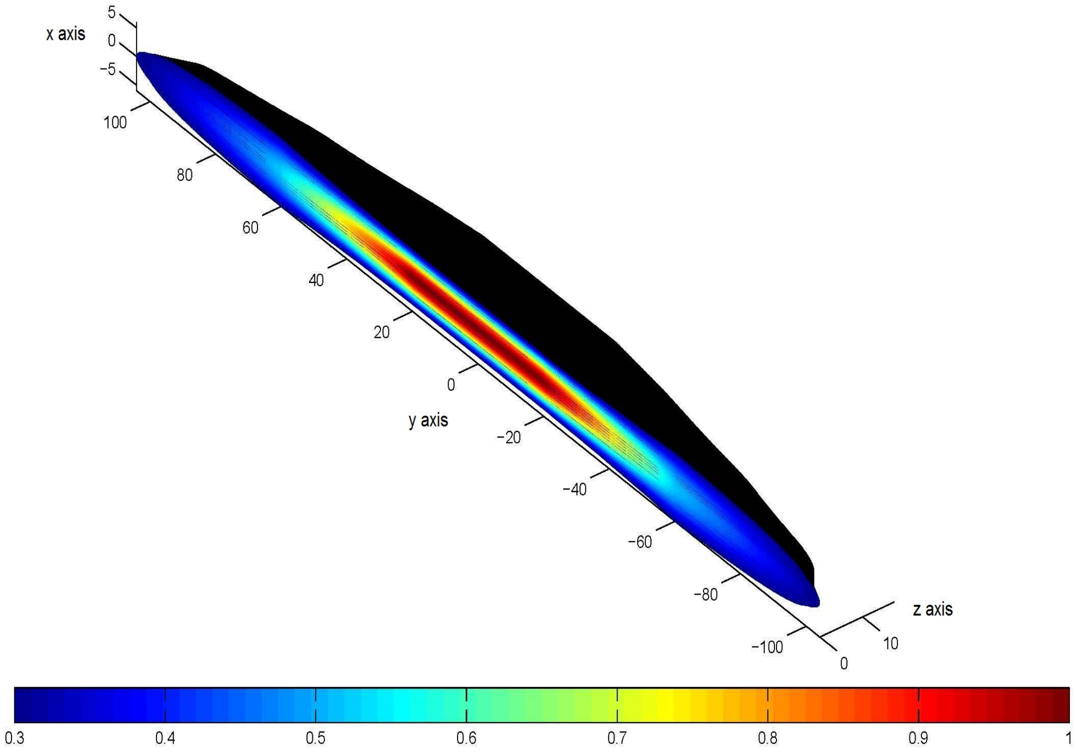

Figure 4.16: *Section of the intensity contour surfaces in the plane $z = 0$. The units of measurement of the three axes are μm.*

showing the level curves relative to different values of intensity (normalized to 1), also called *contour curves*. Moreover also *contour surfaces* can be considered, fig. 4.16, and they help to realize where the the most intense light is confined. In particular it is evident that intensity values that are over the 30% of the maximum intensity can be found in a reduced volume, whose size along the $\hat{y}$ axis is about $\mathrm{L} = 200\,\mu\mathrm{m}$. This volume will represents the *probe* of the experimental measurements, and its longitudinal size L will be considered as the thickness hologram. However this assumption will be experimentally confirmed in the following.

4.5.3 Experimental and data analysis procedures

In this subsection it will be presented the procedure for the acquisition and the subsequent analysis of the experimental data obtained by using the set-up previously described. As mentioned at the beginning of this section, the asymmetric chopper used in these experiments is located in such a way that the beam 2 enters in its open-window when its closed-window stops the beam 1. Therefore the time evolution of the beam 2 can be studied also during the recording of the hologram. Moreover before the chopper two slits are moved to select either the diffracted I_2^d or the transmitted I_2^t part of the beam 2, so that only one of them can reach the detector. In the following the main steps of the procedure adopted for each measurement is reported:

- once the sample is located in the desired position, the branch 1 of the interferometer is blocked and the slits are positioned so that I_2^t is selected, then the laser light is switch on and, since there is any hologram where the beam passes through the sample, all the light is transmitted along the incident direction. In this way for few seconds the intensity, opportunely attenuated, of the transmitted beam 2 is recorded, and it will be used in the data analysis to obtain the grating efficiency [8].

- then, while all the light is stopped, the slits are moved to select the diffracted part of beam 2, so when the light is again switch on the time evolution of I_2^d is recorded during the writing of the hologram.
- when the saturation value of I_2^d is reached either all the light is switch off or, if the erasure process has to be studied, only the beam 1 is stopped. Indeed in this last case, by blocking the beam 1 only the uniform light of beam 2 hits the hologram, inducing a charge carriers redistribution and the consequent erasing of the refractive index grating.

By way of example in fig. 4.17 they are reported the time evolutions of I_2^d during the recording and the erasing of holographic gratings, realized in an undoped lithium niobate crystal and in two diffused Fe:LN samples, one oxidized and the other reduced. As it is possible to notice, sometimes the curve present some irregularities, which occurs at random: they are probably due to some defects on the surface of the sample, such as a particle of dust or a scratch, or to the vibrations which are present in the laboratory and which affect the measurements, since the optical table has not an active vibration-control system.

To analyze the experimental data an important approximation was considered. All the photorefractive theory discussed in the first part of this chapter was develop for the case of planar waves which interfere in a material, whereas, as in the case of this work, to obtain a spatially confined interfering volume focused gaussian beams are used. However, since the photorefractive effect depends on the light intensity, which significantly increases near the beam center, and it is known from the theory[54] that a gaussian beam near its center has wavefronts that are approximatively planar, in this work the beams used are approximated by plane waves. Thus in the following analysis the photorefractive theory for plane waves, described previously, is used. Moreover, since the condition for thick hologram in this work is valid for grating thickness larger than 32μm and the simulated length (about $200\,\mu$m) satisfies this requirement, also the Kogelnik's equations (4.38-4.39) for thick holograms can be used.

The efficiency is derived by normalizing the experimental data relative to I_2^d with the value I_2^t recorded before the beginning of each measure. Then the Kogelnik's equation

---

[8] The intensities of the diffracted and transmitted beams were measured before the recording of the hologram, after its complete build-up and after the total erasing of the grating, verifying that the sum $I_2^{tot} = I_2^t + I_2^d$ does not change. Thus, for simplicity it was chosen to measured this sum before the hologram is written, when $I_2^d = 0$ and therefore only I_2^t has to be measured to obtain I_2^{tot}.

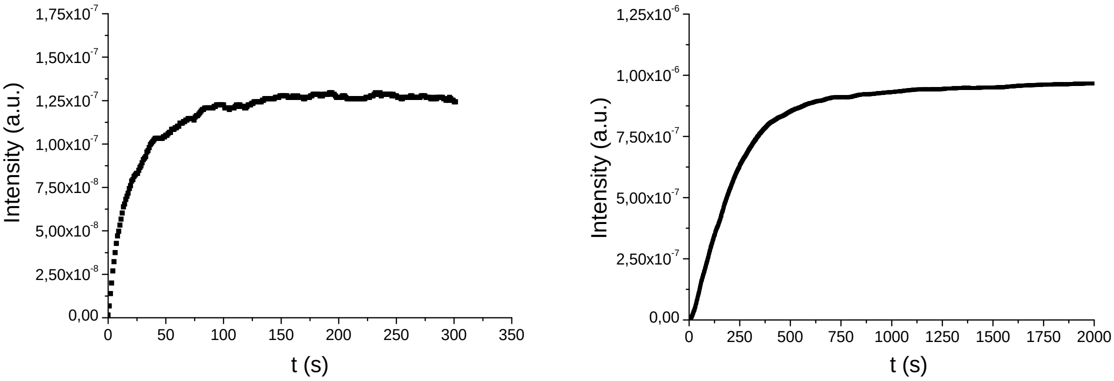

(a) undoped lithium niobate *(b)* oxidized Fe:LN

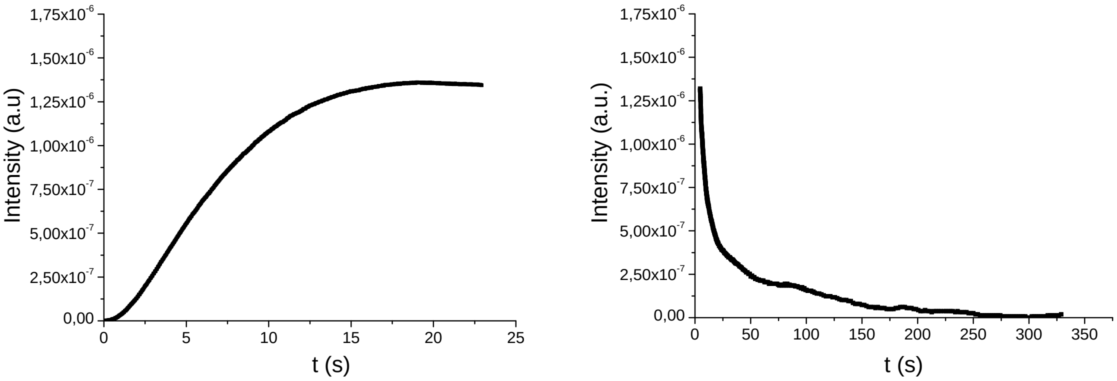

(c) reduced Fe:LN *(d)* reduced Fe:LN

Figure 4.17: *Time evolution of the diffracted intensity I_2^d during the recording of an hologram in an undoped lithium niobate crystal (a) and in two diffused Fe:LN sample, one oxidized (b) and the other reduced (c). In fig. (d) an erasing curve realized in the reduced sample is reported.*

and the formulas relative to the electro-optic effect for an electric field parallel to the $\hat{z}$ axis

$$\begin{aligned}
\Delta n &= \arcsin\left(\sqrt{\eta}\right)\,\frac{\lambda\,\cos(\theta)}{\pi\,L}\\
E_{sc} &= \frac{2\,\Delta n}{n_e^3\,r_{eff}}\\
r_{eff} &= r_{33}\,\cos^2(\theta)\,-\,r_{13}\,\sin^2(\theta)\,+\,\frac{n_e-n_o}{n_e}\,(r_{33}+r_{13})\,\sin^2(2\,\theta)\,=\,30.7\,pm/V
\end{aligned}$$

are used to convert the experimental data to values of space charge field. Concerning the thickness of the written hologram L, an its rough evaluation was obtained in this way: an hologram was completely written inside a diffused Fe:LN sample, then the light was attenuated by a factor 200 and the sample was moved along the longitudinal direction $\hat{y}$ recording the intensity of I_2^d at different positions. The data obtained are reported in figure 4.18 and fitted with a peak function to estimate the full width at half maximum, which results $L = (199 \pm 8)\,\mu$m. This value is in good agreement with that found in the previous subsection by computational simulations, and it will be

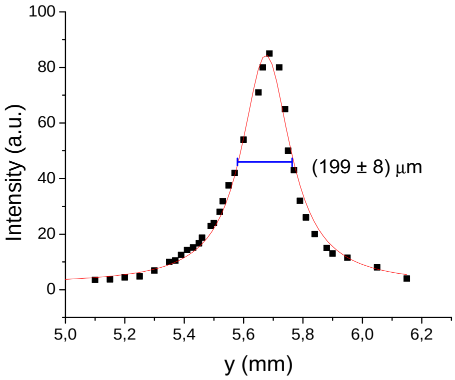

Figure 4.18: *Evaluation of the thickness of the hologramm*

used in eq. (4.49).

Moreover, the maximum intensity used (about 3.5 x 10^5 W/m^2 in the focus of the objective) is not enough low to be sure that the photorefractive one center model still holds but, at the same time, it is not too hight to fall in the two centers model. Thus, initially the one center model was used to study the photorefractive effect in our samples without being sure that it was correct. However successively the validity of this model has been experimentally established, showing a linear dependence between the photoconductivity and the light intensity used, as predicted by the band transport model with one photorefractive center.

In the frame of the one center model the simplified solutions can be used under certain conditions, as described in the subsection 4.3.4. Remembering that the spatial frequency and the period of the grating in this set-up are respectively $K = 1.22 \text{ x } 10^6 \, m^{-1}$ and $\Lambda = 5.15 \text{ x } 10^{-6}$ m and that the maximum iron concentration at the surface of the investigated samples is $N_{Fe^{3+}} \simeq 18 \text{ x } 10^{25} \, m^{-3}$ with a reduction degree $N_{Fe^{2+}}/N_{Fe^{3+}} \simeq 0.04$, the electric fields result

$$E_D \simeq 3 \times 10^5 \, V/m \tag{4.49}$$

$$E_q \simeq 4 \times 10^8 \, V/m \tag{4.50}$$

$$E_q' \simeq 9 \times 10^9 \, V/m \tag{4.51}$$

$$E_{phv} \simeq 8 \times 10^6 \, V/m \tag{4.52}$$

Moreover no external field is applied ($E_0 = 0$) and the pyroelectric effect are negligible for intensity lower than $75 \text{ x } 10^4$ W/m^2[55], so the only fields involved in the photorefractive process are those reported above, which satisfy all the requirements necessary to use the simplified solutions. The exponential equations (4.25-4.26) are hence used to described the time evolution of the space charge field when an holographic grating is recorded or erased.

As example the experimental data shown in fig. 4.17 (c) and (d) are analyzed: the relative values of space charge field are derived and then fitted with exponential func-

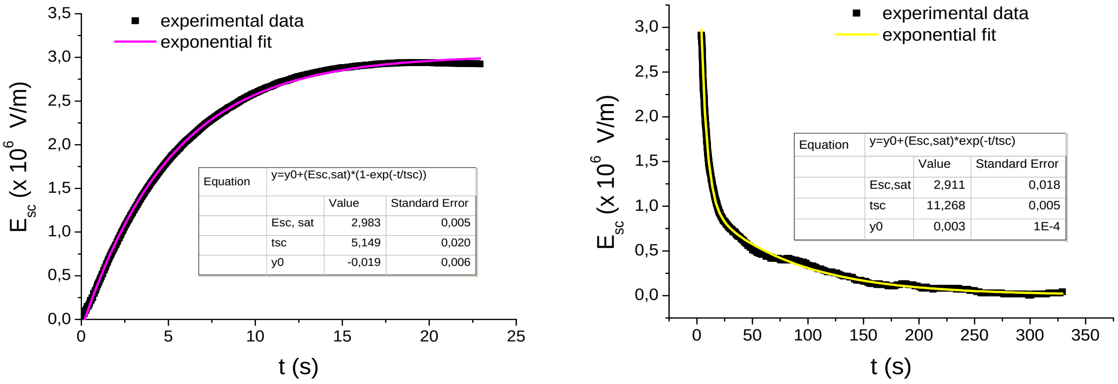

(a) *(b)*

Figure 4.19: *Time evolution of the space charge field during the recording (a) and the erasing (b) of the holographic grating. The data are fitted with exponential functions.*

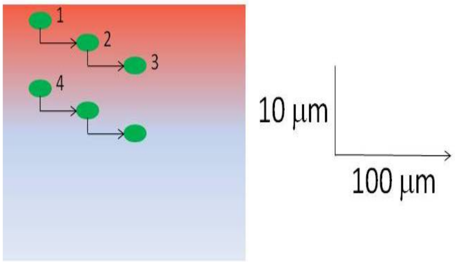

Figure 4.20: *Schematic representation of the sample movement between each measure of a in-depth profile.*

tions, as reported in fig. 4.19, obtaining the saturation value of E_{sc} and the relative time constant. This same analysis has been used to study the experimental data that will be discussed in the next chapter, where in-depth profiles of the saturation space charge field will be presented. Concerning the in-depth profiles, they are realized by performing measurements at different depth from the upper surface of the sample, with steps of $10\,\mu$m. Therefore in order to avoid that an hologram is written over a previously recorded grating, the measurements are not performed along a single vertical line, but for each measure the sample is moved with a *zig-zag* displacement (fig. 4.20), that is a movement of $10\,\mu$m in depth and $100\,\mu$m along the $\hat{z}$ axis.

Chapter 5

Experimental results on photorefractivity and discussion

In this chapter the experimental results of the photorefractive characterization are reported and discussed. In the experiments three different kind of samples are studied: undoped lithium niobate crystals and diffused Fe:LN samples, these latter ones presenting two different reduction degrees, $Fe^{2+}/Fe^{3+} \simeq 0.18\,\%$ and $Fe^{2+}/Fe^{3+} \simeq 4.6\,\%$. The nominally pure lithium niobate crystals are investigated to verify the validity of the experimental data obtained with the new optical set-up, while the Fe-diffused samples are used to study the main physical parameters involved in the photorefractive effect, deriving their in-depth profiles which reveal new important insights on the reduction mechanism in iron diffused lithium niobate samples.

5.1 Fe-diffused samples preparation

In this section they are described the preparation and the main compositional properties of the Fe-diffused samples investigated by mean of holographic measurements.

As reported in [43], in bulk Fe:LiNbO$_3$ the light-induced refractive index change increases linearly with iron concentration up to about 0.05 - 0.06 wt.%, reaching its maximum value at this dopant concentration and saturating for higher iron content. Moreover, the mentioned iron concentration corresponds to about $\mathrm{N}_{Fe} = 18\text{-}20 \times 10^{24}$ at/m^3 (0.1 %mol), which makes valid all the conditions necessary to used the simplified solutions of the one center model, as numerically demonstrated at the end of the previous chapter. For all these reasons it has been decided to realize Fe-diffused lithium niobate samples with a maximum iron concentration at the surface of 0.1% mol. Moreover, being the optical set-up used for holographic measurements completely new, to test its performances it has been also decided to created an iron doped layer with a mean diffusion depth of about only twice the vertical size of the optical probe, that is an iron semi-gaussian profile with HWHM $\simeq 20\mu$m.

In the subsection 2.2.1 it has been already discussed the fact that also by using

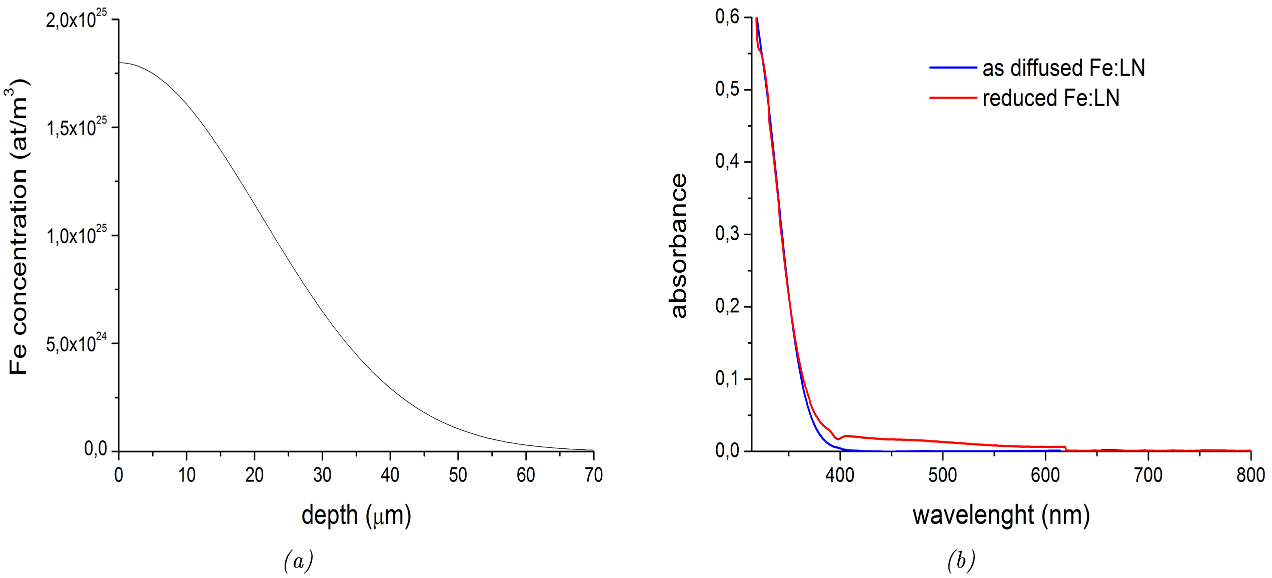

(a) *(b)*

Figure 5.1: *(a) Simulated iron concentration profile after the diffusion of an iron thin film ($t_{dep} = 120s$) at 1100° C for 19.5 h in wet oxygen atmosphere. (b) Optical absorption spectra relative to the as-diffused sample and the reduced one (1h at 500° C in the gas mixture Ar+H_2).*

the thermal diffusion as doping technique it is possible to decide a priori which parameters of the thin film deposition and the thermal treatment have to be used to obtain the desired iron semi-gaussian concentration profile inside the substrate. In particular, to realize the samples we are going to investigate the diffusion temperature of 1100°C was used, whose corresponding diffusion coefficient is $D_{1100°C} = (3.2 \pm 0.1) \cdot 10^{-3}\,\mu m^2\,s^{-1}$. Thus, by using equations 2.2 - 2.3 and remembering that the iron deposition rate is $(4.15 \pm 0.02)\,\mathrm{x}\,10^{14}$ atoms/s cm^2, the deposition and the diffusion times which have to be used to obtain the desired iron concentration profile are calculated. Their respective values are $\mathrm{t}_{dep} = 120\,\mathrm{s}$ and $\mathrm{t}_{diff} = 19.5\,\mathrm{h}$, which, at priori, lead to an HWHM of $\omega_{Fe} = (21.3 \pm 0.5)\,\mu\mathrm{m}$ and a surface concentration of $\mathrm{c}_{sup} = (1.8 \pm 0.04)\,\mathrm{x}\,10^{25}\,\mathrm{at/m}^3$, as reported in fig. 5.1 (a). After the diffusion treatment, the two samples have been cutted into several subsamples, whose final sizes along the $\hat{y}$ and $\hat{z}$ axes are respectively about 4 mm and 20 mm. The latter value derived from geometrical requirements of the polishing machine, while the former one has been kept as small as possible in order to minimize the distance crossed by the incident beams inside the crystal, both to be able to collect the outcoming beams with the 10x objective before they become too divergent and to reduce the presence in the final results of spurious effects due to misalignments of the optical probe with respect to the surfaces of the sample. Subsequently to the cutting each sample was polished on both the $\hat{y}$-faces, which are the light beams input and output sides of the crystal. Finally, to increase the amount of filled traps present in the doped layer, some samples underwent the same reducing annealing in a gax mixture ($\mathrm{Ar} + \mathrm{H}_2$) at 500°C for 1h. In fig. 5.1 (b) the optical absorption spectra relative to the as-diffused samples and the reduced ones are reported, showing a slight increase of the intensity

	A at 342nm	A at 532nm	$[\mathrm{Fe}^{2+}]/[\mathrm{Fe}^{3+}]$
as diffused	0.29 ± 0.02	$(3.6 \pm 2.3)\,\mathrm{x}\,10^{-4}$	$(0.18 \pm 0.12)\,\%$
reduced	0.30 ± 0.02	$(95.6 \pm 57.2)\,\mathrm{x}\,10^{-4}$	$(4.6 \pm 2.9)\,\%$

Table 5.1: *Absorbances relative to the as-diffused and the reduced samples at 342 nm and 532 nm. The derived reduction degrees are reported.*

of the absorption D band in the post-diffusion treated crystals. In table 5.1 they are reported the optical absorbances of the investigated samples, which lead to the reduction degrees of $(0.18 \pm 0.12)\,\%$ and $(4.6 \pm 2.9)\,\%$ for, respectively, the as-diffused and the reduced Fe:LN crystals.

5.2 Nominally-pure congruent LN crystal

Before going on with the discussion of the experimental results, in the following the main physical parameters obtainable from the experimental data are summarized. As already anticipated in the section 4.5.3, from the knowledge of the total intensity of the beam 2, I_2^{tot}, and the measurement of its diffracted part, I_2^d, during the recording of the grating, by using the equation

$$E_{sc}\,(t) \;=\; \arcsin\left(\sqrt{\frac{I_2^t\,(t)}{I_2^{tot}}}\right)\,\frac{\lambda\,\cos\,(\theta)}{\pi\,L\,\left(\frac{1}{2}\,n_e^3\,r_{eff}\right)} \tag{5.1}$$

the time evolution of the space-charge field can be derived. Moreover, remembering that in the case of simplified solutions for the one center model E_{sc} varies exponentially with time (eq. 4.25), then values of the space-charge field can be fitted with the following formula

$$y \;=\; A\,(1 - exp(-t/b)) \tag{5.2}$$

where the variables A and b represent respectively the saturation value of the space-charge field, E_{sc}^{sat}, and the time constant of the recording process, τ_{sc}. Therefore, from these two parameters it is possible to estimate the maximum absolute value of the light-induced refractive index change and the photoconductivity

$$\Delta n \;=\; (1/2)\;n_e^3\,r_{eff}\,E_{sc}^{sat} \tag{5.3}$$

$$\sigma_{ph} \;=\; \frac{\epsilon_{33}\,\epsilon_0}{\tau_{sc}} \tag{5.4}$$

which provide direct informations respectively on the microscopic parameters $[\mathrm{Fe}^{3+}]$ and $[\mathrm{Fe}^{2+}]/[\mathrm{Fe}^{3+}]$ (see eqs. 4.28-4.29). Furthermore, also the photovoltaic current can be calculated, both as the product between the photoconductivity and the space-charge field, $j_{ph} \;=\; \sigma_{ph}\,E_{sc}^{sat}$, and, as an alternative, considering the time derivative of the space-charge field at the beginning of the recording process, that is for $\mathrm{t} \simeq 0$, which results

$$\left.\frac{\partial E_{sc}(t)}{\partial t}\right|_{t\simeq 0} = \frac{E_{sc}^{sat}}{\tau_{sc}} = \frac{E_{sc}^{sat}\,\sigma_{ph}}{\epsilon\,\epsilon_0} = \frac{j_{ph}}{\epsilon\,\epsilon_0} \tag{5.5}$$

In this way also informations on the filled trap concentration [Fe^{2+}] can be obtained, since this parameter is linearly proportional to j_{ph}, which will provide interesting news on the reduction mechanisms of Fe-diffused samples.

In the following subsections a commercial undoped congruent x-cut lithium niobate crystal is used to calibrate the experimental set-up and verify the accuracy and precision of the measurements.

5.2.1 Experimental method

To test the repeatability of the holographic measurements, in different points of a congruent lithium niobate crystal several holographic gratings are written and the time evolution of the diffracted intensity I_2^d is measure during the recording process. Before starting with the experiment the alignment of the sample is checked, both by verifying the position of the beams which are reflected at the surfaces of the crystal, and by testing that the sample is located in the focus of the objective. After the alignment, several time evolutions of the diffracted beam during the built-up of the hologram are recorded (fig. 5.2) and, by fitting the corresponding time evolution of the space-charge field, as described in the previous subsection, the time constant and the saturation value of the electric field are derived: the obtained values are listed in table 5.2 and their means are respectively $\tau_{sc} = (24.66 \pm 2.53)$ s and $E_{sc}^{sat} = (37.34 \pm 5.13) \,\mathrm{x}\, 10^4$ V/m. Since these measurements are performed in a sample obtained by cutting a commercial wafer, reasonably the observed differences between the values of τ_{sc} and E_{sc}^{sat} can not be attributed to compositional variation inside the material, but, as mentioned above, to the presence of scratch or dust on the surfaces or, most probably, to the absence of an active vibration-control system. Thus, to take into account these effects, in the following the relative error derived experimentally by the means of τ_{sc} and E_{sc}^{sat} of undoped commercial lithium niobate

τ_{sc} (s)	E_{sc}^{sat} ($\times 10^4$ V/m)
30,76 ± 0,34	25,01 ± 0,10
17,35 ± 0,19	40,88 ± 0,06
25,87 ± 0,26	59,11 ± 0,08
23,41 ± 0,24	25,90 ± 0,03
35,65 ± 0,29	39,66 ± 0,05
18,09 ± 0,24	33,48 ± 0,07

Table 5.2: *Values of the saturation space-charge field and the time constant obtained by fitting the recording curves shown in fig.5.2.*

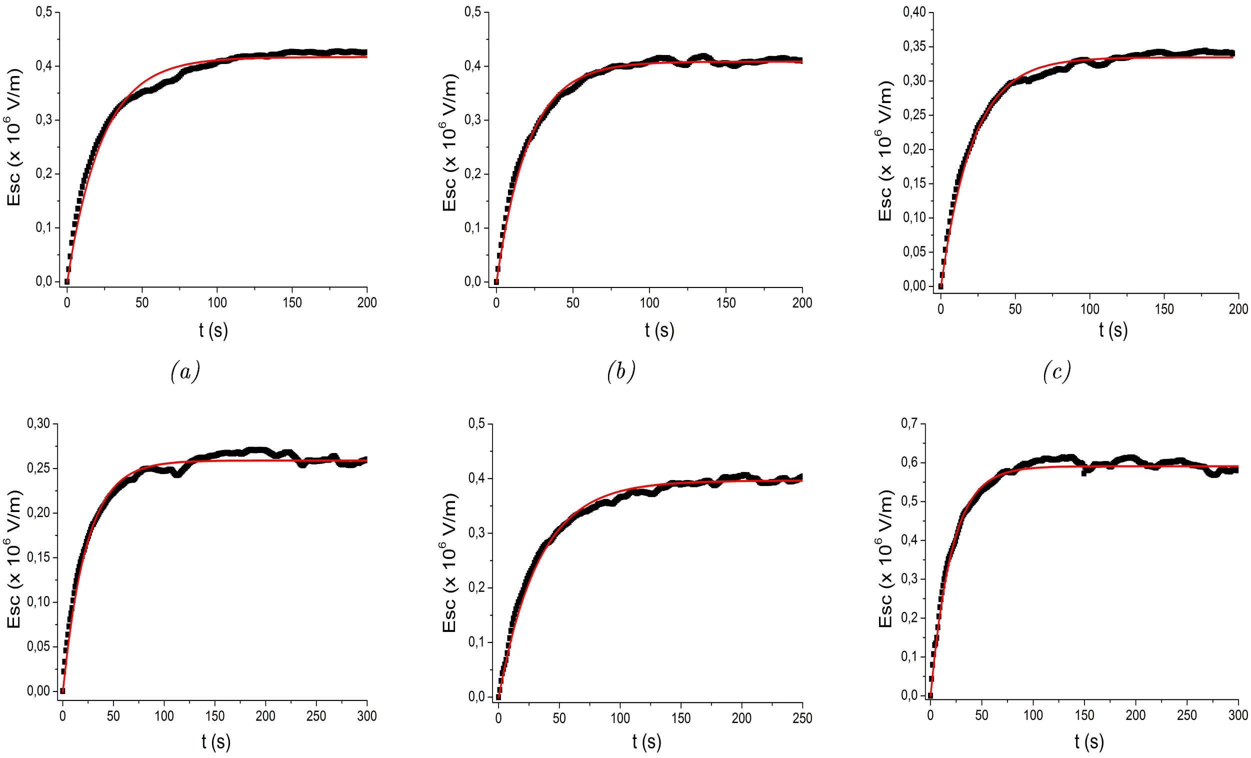

(a) (b) (c)

(d) (e) (f)

Figure 5.2: *Hologram recording curves realized in a congruent lithium niobate crystal and relative fitting curves.*

crystals, which is about 13%, will be attributed to all the parameters obtained by holographic measurements.

5.2.2 In depth profiles

While the photorefractive properties in bulk Fe:LN crystals are well investigated, on the contrary the PR process in nominally-undoped lithium niobate is less clear and only few works [56, 57, 58] deal with it. In these crystals the responsibles for the photorefractive effect are the photorefractive impurity centers, predominantly iron, which are native in the material and whose concentration, in commercial wafers, is about 1-2 ppm. Due to this low concentration, to observe clearly the photorefractive effect in an undoped crystals, intensities larger than 10 W/cm^2 are required, thus in the following experiments the maximum light intensity achievable with this set-up is used, that is 35 W/cm^2.

The calibration and the experimental protocol to perform the best measures is the result of several tests, which have also helped to improve the performance of this optical set-up. In particular, the most critical problem is the sample alignments, therefore special care has been devoted to obtain reproducible measurements.

An in-depth profile is realized by performing several holographic measurements at different depths inside the crystal, as described in the previous chapter. The recorded

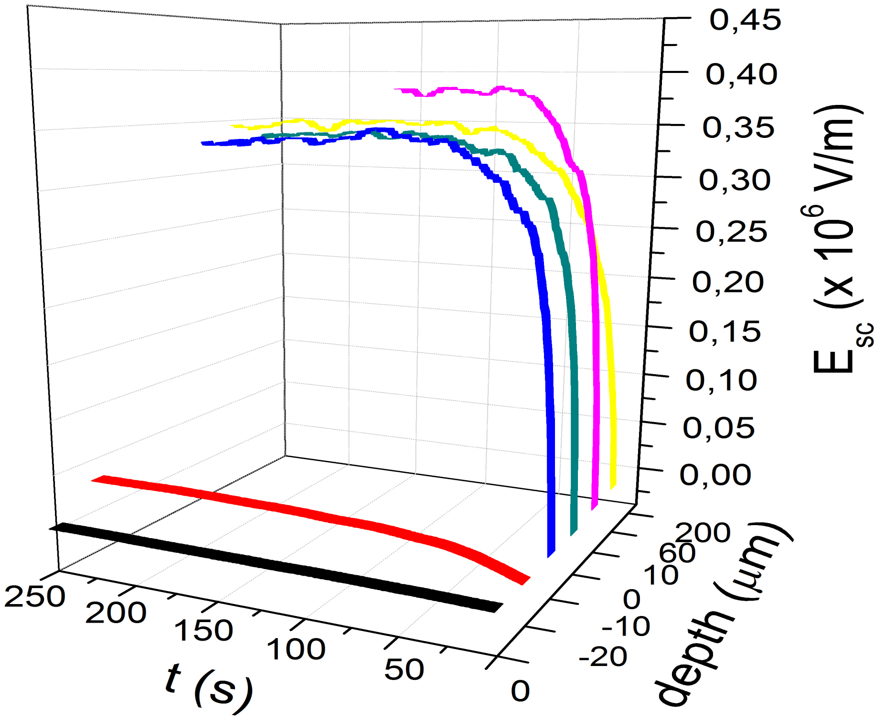

Figure 5.3: *Three-dimensional representation of the time evolution of E_{sc} during the recording of an holographic gratings at different depths inside a nominally-pure Lithium niobate crystal. The intensity used is I = 35 W/cm2.*

intensity I_2^d is subsequently converted to efficiency, and, by using Kogelnik's relation, the space charge field E_{sc} is derived. The experimental curves are illustrated in fig. 5.3, in a three-dimensional representation which clearly shows how the time evolution of E_{sc} and its saturation value change when the probe moves from outside to inside the sample. By plotting the saturation values of the space-charge field as a function of depth, the in-depth profile of figure 5.4 is obtained and the relative values are reported in table 5.3. The negative values of the x axis refer to the area outside the sample, and for distances larger than 20 μm from the crystal surface no I_2^d was detected. Concerning the shape of the profile, the main features are:

- the change of the value of E_{sc}^{sat}, from 0 to about 35×10^6 V/m, is not sharp but

depth (μm)	E_{sc}^{sat} ($\times 10^4$ V/m)	τ_{sc} (s)
-20	0,2 ± 0,1	453,4 ± 68,0
-10	2,9 ± 0,4	46,9 ± 7,0
0	34,3 ± 5,1	19,5 ± 2,9
10	33,9 ± 5,1	18,1 ± 2,7
60	37,6 ± 5,6	19,6 ± 2,9
210	34,5 ± 5,2	20,0 ± 3,0

Table 5.3: *Values of the saturation space-charge field and relative time constant of the in depth profile of fig.5.3. The negative values of the depth refers to the area outside the sample, so that the origin of the x axis corresponds to the doped edge of the crystal.*

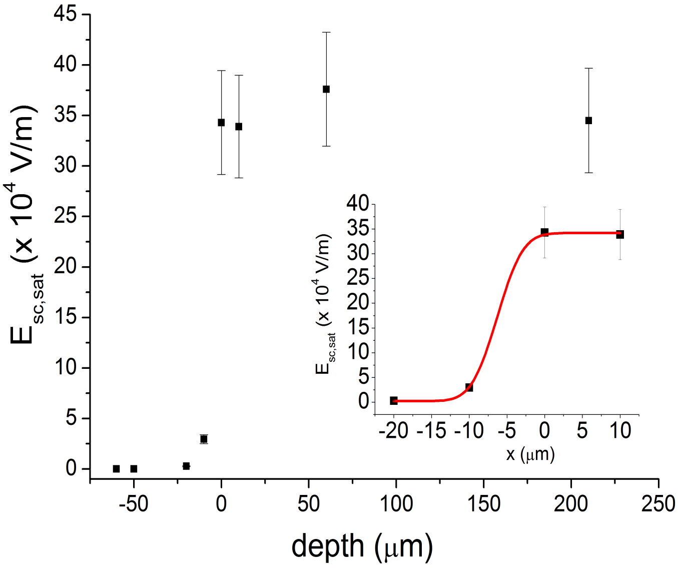

Figure 5.4: *In-depth profile of the saturation value of E_{sc} for an undoped LN crystal, obtained with a light intesity of $I = 35$ W/cm^2. In the in-set the erf fit is reported, with a FWHM of $(5.4 \pm 0.7)\,\mu m$.*

it occurs in about 10-15 μm, as it is possible to see in the in-set of fig. 5.4. This smooth transition is due to the vertical sixe of the probe, whose waist in chapter 4 was estimated to be $(5.1 \pm 0.7)\,\mu$m. To confirm this value, the transition length was estimated by fitting the in-depth profile near the surface of the sample with the error function, obtaining a HWHM $= (5{,}4 \pm 0{,}7)\,\mu$m, which is in good agreement with the size of the probe along the $\hat{x}$ axis. Moreover this result is a check that the sample is correctly aligned respect to the two incident beam. Indeed if there are same sample misalignments, then the in-depth profile presents a smoother shape in the transition from outside to inside the sample (fig. 5.5), affecting also the trend of E_{sc}^{sat} inside the crystal. Summarizing, a good alignment of the sample is crucial for this type of holographic measurements and it can be further checked by how sharp is the transition from the "outside" to the "inside" of the sample.

- inside the sample the values of E_{sc}^{sat} are comparable within the errors and, as expected, they are constant all over the investigated depth, which extends up to 210 μm from the surface of the crystal. This means that the concentration of the native photorefractive centers does not change in the crystal and, above all, that if an in-depth trend of the photorefractive properties will be observed in diffused Fe:LN, it can be only attributed to the incorporation of the dopant, whose diffusion length is well shorter than the 210 μm investigated.

Moreover, remembering the equations (4.22 - 4.24) and that the spatial frequency of the grating is parallel to the $\hat{z}$ axis of the sample, in the frame of the simplified

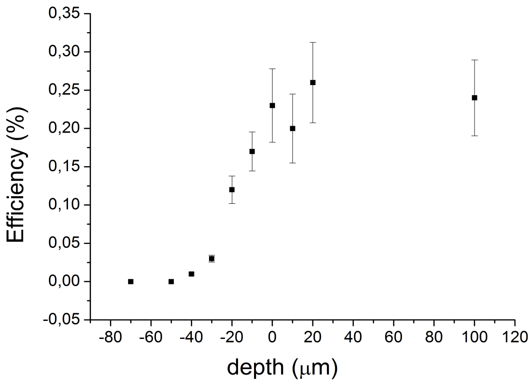

Figure 5.5: *In-depth profile of the efficiency for an undoped LN crystal which is not correctly aligned respect to the incident beams.*

solutions for the one center model it derives

$$\sigma_{ph} \;=\; \frac{\epsilon_{33}\,\epsilon_0}{\tau_{sc}} \tag{5.6}$$

and also the photoconductivity in-depth profile can be obtained. The σ_{ph} trend shown in figure 5.6 presents the same features observed in the E_{sc} profile, that are a very sharp curve near the surface of the sample, and a constant value of photoconductivity inside the material. The mean values of the space charge field and the photoconductivity obtained for this sample are respectively $E_{sc}^{sat} = E_{phv} = (35.1 \pm 0.9)\,\mathrm{x}\,10^4\,\mathrm{V/m}$ and $\sigma_{ph} = (13.4 \pm 0.4)\,\mathrm{x}\,10^{-12}\,\Omega^{-1}\,\mathrm{m}^{-1}$, which agree with the values recently found by Buse et al.[58]. The induced refractive-index change can be estimate by using eq. (4.30),obtaining $\Delta n = (5.7 \pm 0.1)\,\mathrm{x}\,10^{-5}$, which is perfectly comparable with the value measured by Althoff et al.[59].

Moreover, as already mentioned, also the photovoltaic current in the material can be estimated, as

$$j_{phv} \;=\; \sigma_{ph}\,E_{sc}^{sat} \tag{5.7}$$

or by using a linear fit of the first part of the recording curve

$$j_{phv} \;=\; \epsilon_{33}\,\epsilon_0\,\frac{\partial\,E_{sc}(t)}{\partial\,t}\bigg|_{t\simeq 0} \tag{5.8}$$

deriving respectively $(4.7 \pm 0.2)\,\mathrm{x}\,10^{-6}\,\mathrm{A/m^2}$ and $(5.2 \pm 0.8)\,\mathrm{x}\,10^{-6}\,\mathrm{A/m^2}$. This parameter allows to determine the amount of Fe^{2+} present in the sample and its corresponding reduction degree. Indeed $j_{phv} = \beta^*\,c_{Fe^{2+}}\,I$, where for iron concentration up to $10^{25}\,\mathrm{m}^{-3}$ $\beta^* = 6\,\mathrm{x}\,10^{-33}\,\mathrm{A\,m^3\,W^{-1}}$[43], so the Fe^{2+} concentration is estimated to be $N_{Fe^{2+}} = 2.3\,\mathrm{x}\,10^{21}\,\mathrm{m}^{-3}$. Since the crystal used is a commercial one with a declared amount of iron less than $N_{Fe} \approx 2\,\mathrm{ppm} = 4\,\mathrm{x}\,10^{22}\,\mathrm{m}^{-3}$, it derives that the native reduction degree of a nominally-pure lithium niobate crystal is about $\mathrm{Fe}^{2+}/\mathrm{Fe}^{3+} \simeq 6\,\%$.

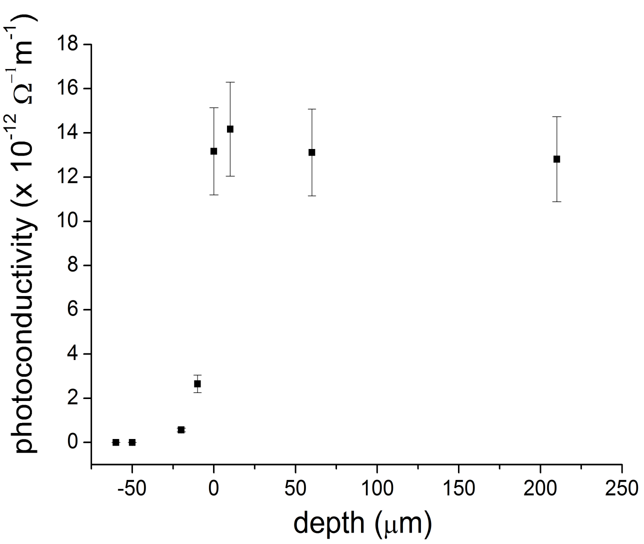

Figure 5.6: *In-depth profile of the photoconductivity realized in an undoped LN crystal, with a light intesity of* $I = 35\ W/cm^2$.

Summarizing, a nominally-pure lithium niobate crystal was measured to test the set-up, verifying that the results obtained with these holographic measurements are in good agreement with those reported in literature. Moreover, several measurements were performed in order to find the best conditions, concerning above all the alignment of the sample and the position of the optical components, to measure the time evolution of the diffracted beam I_2^d. Finally, it was found that photorefractive properties are homogeneous inside the sample, as expected, and an native iron reduction degree of about 6 % was derived.

5.3 As-diffused iron doped lithium niobate sample

In this section an as-diffused iron doped lithium niobate sample is investigated by holographic measurements, discussing the results obtained. Before starting with the analysis, it has to be remembered that, as mentioned in the chapter 2, the diffusion of iron in a substrate of lithium niobate crystal occurs in an oxygen wet atmosphere, so that after the thermal treatment the dopant, except for a small percentage, is in its Fe^{3+} state. In particular the integral reduction degree of the sample considered now is $Fe^{2+}/Fe^{3+} = (0.18 \pm 0.12)\,\%$, as reported at the beginning of this chapter. Moreover, it is important to recall that this value refers to the integral amount of filled traps present in the whole doped layer, without providing any informations on the depth distribution of Fe^{2+}.

As for the undoped sample, also for this crystal the dependence of the photorefractive effect on the depth is studied at the maximum intensity $I = (35 \pm 4)\,x\,10^4\ W/m^2$. As an example, the fig. 5.7 shows the time evolution of the space-charge field E_{sc} inside

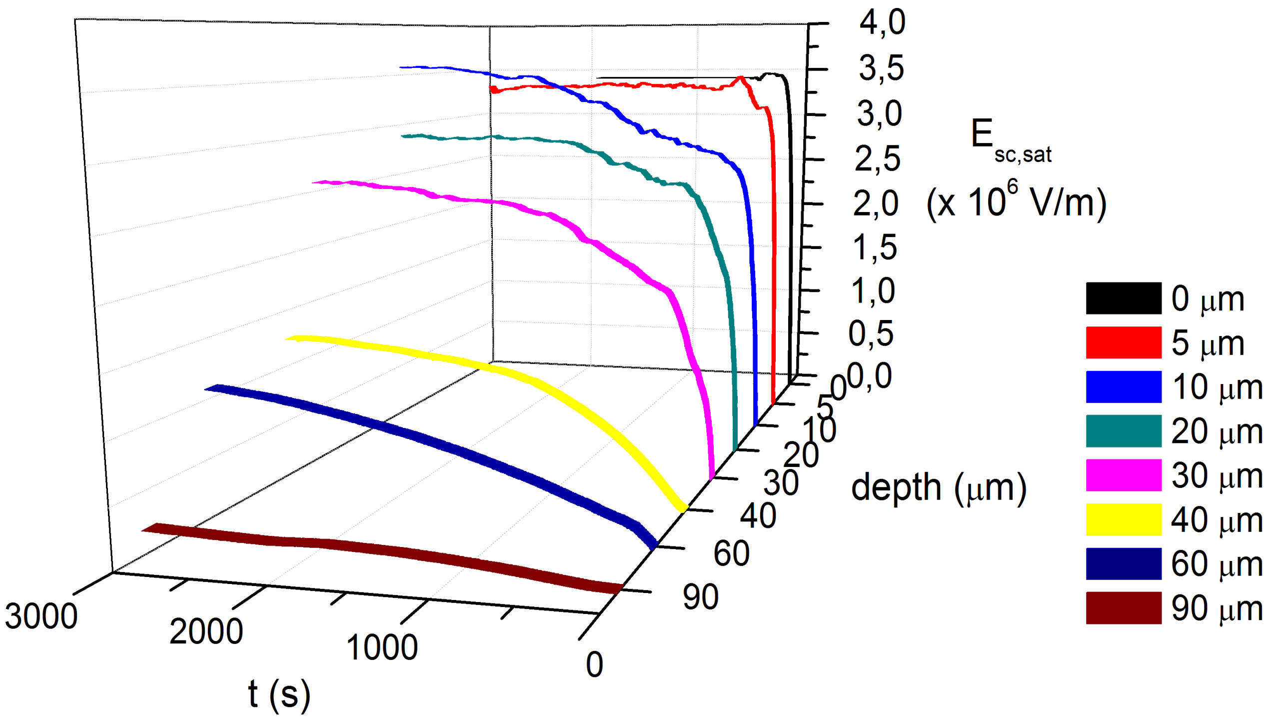

Figure 5.7: *Recording curves of holographic gratings in an as-diffused lithium niobate crystal doped with iron.*

the sample, at different positions along the direction of iron diffusion. The most plain difference with respect to the pure crystal is the progressive decreasing of the saturation value of the space-charge field from the sample surface ($0\,\mu$m) to deeper positions, reaching areas where the dopant is absent (above 60-70 μm). Moreover, as expected, the E_{sc}^{sat} is an order of magnitude larger than that observed in the previous section, since by introducing iron atoms the photorefractive centers of the material are increased, enhancing its photorefractive sensitivity.

Several in-depth profiles have been performed in different zones of the sample, and the mean values of the space-charge fields, as a function of the depth, are reported in figure 5.8 and listed in table 5.4. If the one center model with simplified solutions is applied, the saturation values of the space charge field results the opposite of the photovoltaic one, given by

$$E_{phv} = \frac{j_{ph}}{\sigma_{ph}} = \frac{k_G\,\gamma}{e\,\mu} N_{Fe^{3+}} \tag{5.9}$$

and it derives that E_{sc}^{sat} depends only on the concentration of empty traps. This is confirmed by the experimental data, since it is evident that the space-charge field profile recalls the iron concentration one. Thus the in-depth profiles are fitted with a gaussian function, obtaining as half width at half maximum $\omega_{PR}^{exp} = (24.0 \pm 1.1)\,\mu$m.

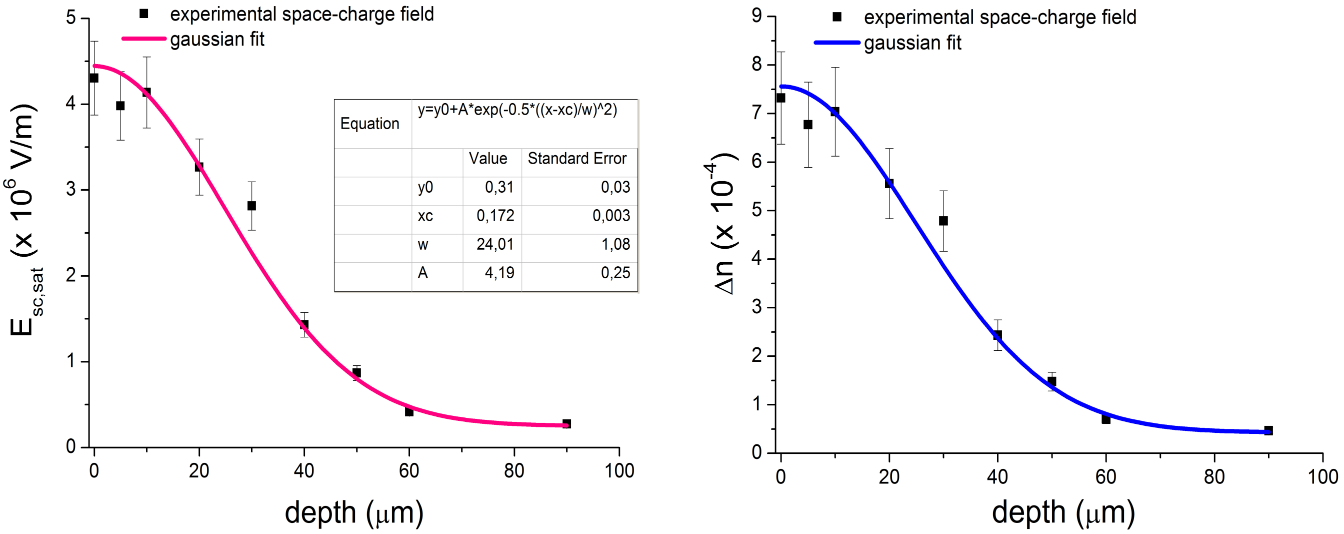

(a) *(b)*

Figure 5.8: *In-depth profiles of the saturation values of the space-charge field (a) and the relative induced refractive index change (b) for an as-diffused Fe:LN sample.*

depth (μm)	E_{sc}^{sat} ($\times 10^6$ V/m)	τ_{sc} (s)	Δn^{sat} ($\times 10^{-4}$)
0	4.3 ± 0.4	33 ± 8	7.3 ± 0.9
5	4.0 ± 0.4	46 ± 5	6.8 ± 0.9
10	4.1 ± 0.4	99 ± 3	7.0 ± 0.9
20	3.3 ± 0.3	159 ± 2	5.6 ± 0.7
30	2.8 ± 0.3	402 ± 1	4.8 ± 0.6
40	1.4 ± 0.1	811 ± 2	2.4 ± 0.3
50	0.9 ± 0.1	1289 ± 3	1.5 ± 0.2
60	0.41 ± 0.04	2547 ± 1	0.7 ± 0.1
90	0.32 ± 0.02	4251 ± 1	0.52 ± 0.03

Table 5.4: *The table reports the mean values of E_{sc}^{sat} and τ_{sc}, obtained by several profiles, along the iron diffusion direction $\hat{x}$.*

As a matter of fact E_{sc}^{sat} has a deeper profile than that one of the dopant concentration ($\omega_{Fe} = (21.3 \pm 0.5)\,\mu$m), but however this direct measure cannot be used to derive informations on the doped layer, since the contribution of the probe size ($\omega^v = (5.1 \pm 0.7)\,\mu$m) must be considered. Indeed the experimental profile has a shape which is the convolution of the experimental parameters, such as the size of the probe, and the real trend of the physical property measured. Thus, considering the convolution theory of two gaussian functions the correct value of ω_{PR}^{exp} is obtained as

$$\begin{aligned} \omega_{PR}^{corr} &= \sqrt{\left(\omega_{PR}^{exp}\right)^2 - \left(\omega^v\right)^2} \\ &= (23.5 \pm 1.3)\,\mu m \end{aligned}$$

which, within the errors[1], is compatible with the theoretical half width at half maximum of the iron concentration profile. Moreover, by exploiting the theory of the electro-optic effect, also the in-depth profile of the induced refractive index change can be derived, as illustrated in fig. 5.8, with a saturation value at the surface of the sample of $\Delta n^{sat} = (7.3 \pm 0.9) \times 10^{-4}$. The linear dependence of Δn^{sat} and E_{sc}^{sat} on the concentration of empty traps N_{Fe3+} is thus verified within the experimental errors, as expected by the band transport model with one photorefractive center, and also the capability of this optical set-up to investigate spatially confined areas of the doped layer is confirmed. Finally, since at 90 μm below the crystal surface the dopant should be absent, it is expected that there the saturation value of the space charge field is the same found in previous section for a nominally pure crystal. This is confirmed by the experimental results, obtaining at that depth $E_{sc}^{sat} = (32 \pm 2) \times 10^4$ V/m and $\Delta n^{sat} = (5.2 \pm 0.3) \times 10^{-5}$. This means that the bulk concentration of Fe^{3+} ions is almost the same in as-diffused and in undoped crystals, as expected. On the other hand, the τ_{sc} in the bulk of as-diffused samples is significatively larger than that of the pure congruent one. This indicates that the reduction degree $[Fe^{2+}]/[Fe^{3+}] \propto \tau_{sc}^{-1}$ is lower in the former case, due to a lower concentration of Fe^{2+} ions ($N_{Fe^{2+}} = \epsilon\,\epsilon_0\,E_{sc}^{sat}/\tau_{sc}\,I\,\beta^* \approx 8.9 \times 10^{18}\,\mathrm{m}^{-3}$ and $[Fe^{2+}]/[Fe^{3+}] \approx 0.02\%$). This effect can be explained taking into account the hight temperature of the thermal treatment (1100°C) and the long diffusion time (10h) which induce the thermal excitation and the subsequent transport of the electrons present in the substrate. These electrons, as demonstrated in [19], travel through the whole material, reaching the areas with an higher amount of iron, that is the doped layer, where they are captured by the Fe^{3+} traps, leaving the undoped part of the sample with a decreased reduction degree.

---

[1] Except for the parameters directly derived from the experimental data, such as E_{sc} and τ_{sc}, whose relative errors are fixed at 13% as discussed at the beginning of this chapter, the errors of all the other quantities presented in this work are calculated by means of the error propagation rule.

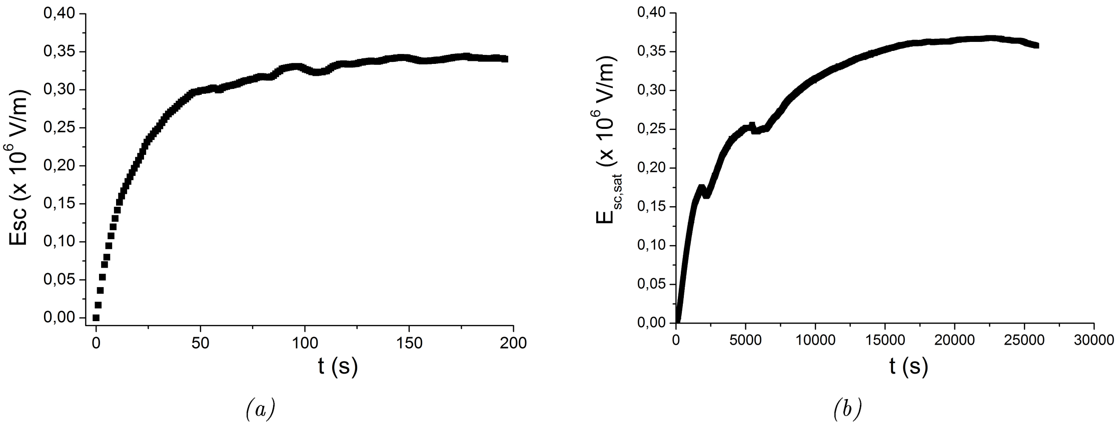

Figure 5.9: *Hologram recording curves realized in a congruent lithium niobate crystal (fig.(a), $\tau_{sc} = (25.9 \pm 0.3)\,s$) and at 90 μm below the surface of an as-diffused Fe:LN sample (fig.(b), $\tau_{sc} = (4251 \pm 1)\,s$).*

Concerning the photoconductivity σ_{ph}, since in the one center model the relation

$$\sigma_{ph} = \frac{e\,\mu\,s}{\gamma} I \frac{[Fe^{2+}]}{[Fe^{3+}]} \tag{5.10}$$

is valid, if the ratio [Fe^{2+}]/[Fe^{3+}] is constant over all the doped layer, as assumed until this moment, the photoconductivity should have the same value in each point along the iron concentration profile. On the contrary, the photoconductivity values, derived by the time constants listed in table 5.4, have a clear in-depth dependence, as shown in fig. 5.10. This finding indicates that Fe^{2+} and Fe^{3+} are distributed along the depth of the doped layer with two different profiles. To have a rough estimate of the half width at half maximum of the curve relative to σ_{ph}, a Lorentz function has been used to fit the experimental data, obtaining $\omega_{ph} = (8.3 \pm 1.2)\,\mu$m, which is very close to the vertical radius of the experimental probe, suggesting that the filled traps present in the doped layer are confined in a small area (some micrometers) near the sample surface. However, this new aspect of the photorefractive effect will be more extensively investigated in the next section, in the case of a reduced iron doped crystal.

The de-convolution[2] of ω_{ph} with ω^{v}_{probe} leads to a photoconductivity HWHM of $\omega^{corr}_{ph} = (3.2 \pm 0.9)\,\mu$m, which suggests that all the Fe^{2+} is distributed in a layer deep less than 5-6 μm. In this way at the surface of the sample a reduction degree of $(1.1 \pm 0.9)\,\%$ is reached, which, due to the high errors deriving from the optical absorption measurements, is consistent with the values obtained experimentally ($(0.18 \pm 0.12)\,\%$). So, knowing the constant $A = e\,\mu\,s/\gamma \approx 1 \times 10^{-14}\,m\,W^{-1}\,\Omega^{-1}$[43] for a moderatly iron doped lithium niobate crystal, it follows that the photoconductivity is $\sigma_{ph} \approx (1.7 \pm 0.9) \times 10^{-11}\,\Omega^{-1}\,m^{-1}$.

Finally, if the photoconductive constant typical of nominally pure lithium niobate

---

[2] The de-convolution rule for lorentzian functions is $\omega^{corr}_{ph} = \omega^{exp}_{ph} - \omega^{v}_{probe}$.

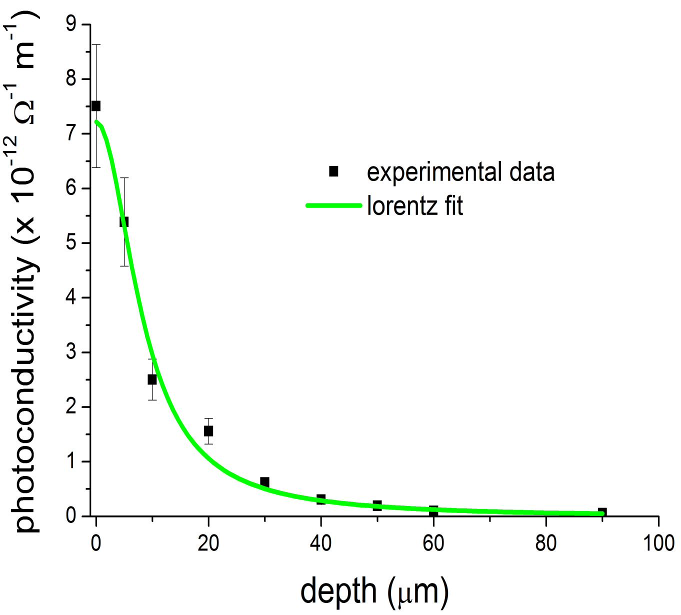

depth (μm)	σ_{ph} (x10^{-12}) $\Omega^{-1}\,\text{m}^{-1}$
0	7.5 ± 1.1
5	5.4,$\pm$0.8
10	2.5 ± 0.4
20	1.6 ± 0.2
30	0.6 ± 0.1
40	0.31 ± 0.05
50	0.19 ± 0.03
60	0.10 ± 0.01
90	0.06 ± 0.01

Figure 5.10: *In-depth profile of the photoconductivity in an as-diffused Fe:LN sample and list of the relative values.*

crystals is taken into account ($A = 8\,\text{x}\,10^{-16}\,\text{m}\,\text{W}^{-1}\,\Omega^{-1}$[58]), the expected photoconductivity in the bulk material should be $5.6\,\text{x}\,10^{-14}\,\Omega^{-1}\,\text{m}^{-1}$ for a reduction degree of 0.02%, once again in agreement with the experimental data.

5.4 Reduced Fe:LN sample

In the following a reduced Fe:LN sample is widely studied, not only investigating the relation between its photorefractive properties and the integral reduction degree, which is $\text{Fe}^{2+}/\text{Fe}^{3+} = (4.6 \pm 2.9)\,\%$, but also verifying the validity of the assumptions used up to now to analyze the experimental results.

5.4.1 Soundness of the one center model

Since, as mentioned above, the intensities used in the present work lies in the range between the one center model and that with two photorefractive centers, a priori it is not possible to know which model is the correct one to analyze the results obtained. Up to now, the one center model was used, due to its simplicity and thanks to the fact that it can be used to compare our results with data available in literature. However, before going on with this analysis it is mandatory to check the soundness of the theory used at the intensities up to $35\,\text{W/cm}^2$. A simply way to discriminate between the two models consists in verifying which type of relation exists between the photoconductivity and the intensity of the light pattern. Indeed, as spelt out in chapter 4, if the one center model is valid σ_{tot} increases linearly with I, whereas in the case of the two centers model there is a quadratic dependence of the

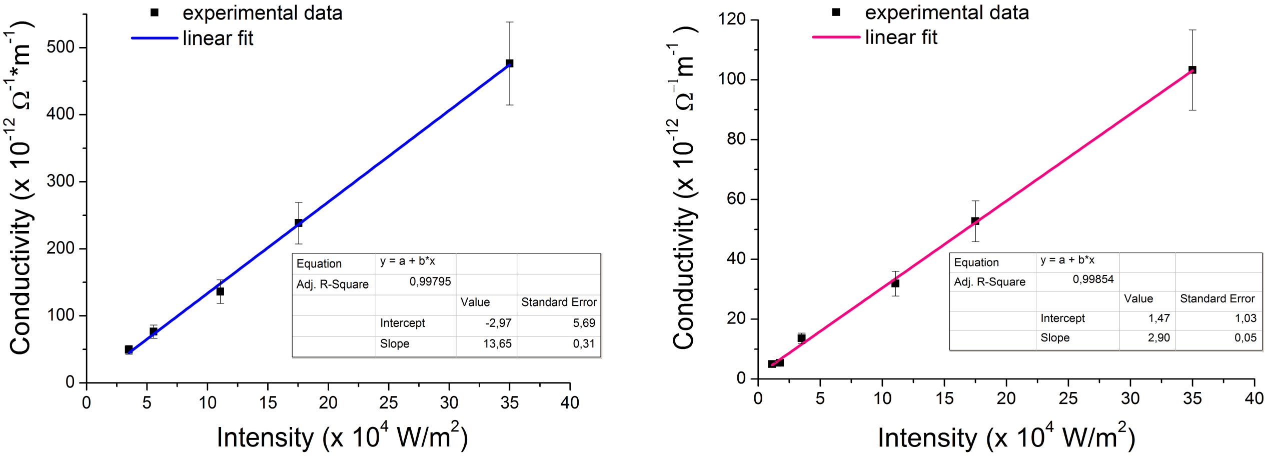

(a) *(b)*

Figure 5.11: *Total photoconductivity as a function of light intensity at 0 μm (a) and 30 μm (b) below the surface of a reduced Fe:LN sample*

photoconductivity on the light intensity. Therefore, several holographic gratings were written at the same depth below the crystal surface but at different light intensities, and the total conductivity was derived by the time evolution of the recording process. In fig. 5.11 the conductivities measured at 0 μm and 30 μm below the surface of the sample are reported as a function of the incident light intensities and, since it is evident that σ_{tot} varies linearly with I, the validity of the one center model is verified. The experimental data are fitted with a linear function and the physical meanings of the intercept and the slope of each curve can be understood considering the equation

$$\sigma_{tot} = \sigma_{ph} + \sigma_{dark} = \alpha\, I + \sigma_{dark} \tag{5.11}$$

$$\alpha = \frac{e\,\mu\, s}{\gamma}\,\frac{[Fe^{2+}]}{[Fe^{3+}]} \tag{5.12}$$

where the intercept is the dark conductivity σ_{dark}, while the slope represents the specific photoconductivity α. In both the cases the intercepts are negligible within the errors ($\sigma_{d,1}$ = (-2,97 ± 5.69) x $10^{-12}\,\Omega^{-1}\mathrm{m}^{-1}$ and $\sigma_{d,2}$ = (1.47 ± 1.03) x $10^{-12}\,\Omega^{-1}\mathrm{m}^{-1}$): this confirms that $\sigma_{dark} \ll \sigma_{ph}$ and, consequently, that the total conductivity can be approximated by the photoconductivity and derived directly from τ_{sc}, as done in the previous sections. However this analysis gives only a rough estimate of σ_{dark}, which will be better measured and discussed subsequently. Concerning the slopes of the straight lines, it is immediately clear that they are not equal (α_1 = (13.65 ± 0.31) x $10^{-16}\,\mathrm{m}\,\Omega^{-1}\mathrm{W}^{-1}$ and α_2 = (2.90 ± 0.05) x $10^{-16}\,\mathrm{m}\,\Omega^{-1}\mathrm{W}^{-1}$), as in the case of the as-diffused samples. This behaviour suggests that one or more parameters involved in eq. 5.12 are not constant along the iron concentration profile as, for instance, the reduction degree of the dopant, as briefly mentioned in the case of the as-diffused sample. However in the following analysis also this aspect will be took into account.

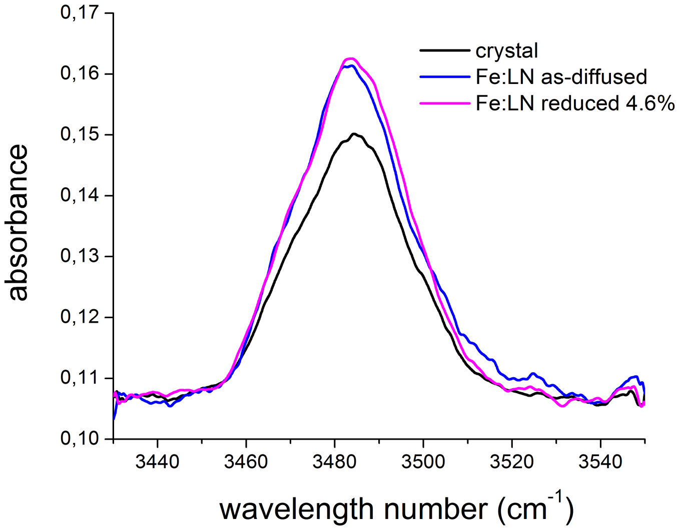

Figure 5.12: *Infrared spectra of the undoped crystal, the as-diffused iron doped lithium niobate sample and the reduced one.*

5.4.2 The dark conductivity

As already anticipated in chapter 4, in lithium niobate crystals with iron doping levels up to about 0.1 % mol, the dark conductivity is dominated by the proton transport, with a time constant which is inversely proportional to the amount of H^+[49]. Since the molecule H_2 present in the reducing gas dissociates into proton and electrons ($H_2 \rightarrow 2\,H^+ + 2\,e^-$) which are both incorporated in the crystal, it was firstly verified whether the content of proton inside the sample was changed by the reducing thermal treatment. A relative estimate of the amount of H^+ in the three samples considered up to now (the undoped crystal, the as-diffused and the reduced ones) has been realized by performing infrared (IR) optical absorption measurements, since the main absorption peak of the OH^- stretching bond, that is about 3482 cm^{-1}, changes it intensity proportionally to the hydrogen content[17]. The results obtained are reported in fig. 5.12, where it is possible to notice that the peaks relative to both the as-diffused and the reduced samples have almost the same intensity, which means that the exposition of the as-diffused sample to an $Ar+H_2$ gas for 1 hour has not increased significantly the amount of proton in the material. Moreover, the increasing of the peak intensity respect to the undoped crystal id due to the water-vapor rich atmosphere already present on the diffusion thermal treatment, since at the surface of the crystal the reaction $H_2O \leftrightarrow H^+ + OH^-$ occurs, leading to the incorporation of both protons and OH^- groups in the sample.
After verifying that the amount of proton is approximatively the same in the as-diffused and the reduced samples, the same approach seen in subsection 5.4.1 was used to obtain informations on the depth dependence of dark conductivity. Indeed by linearly fitting for each depth the photoconductivities measured at the three dif-

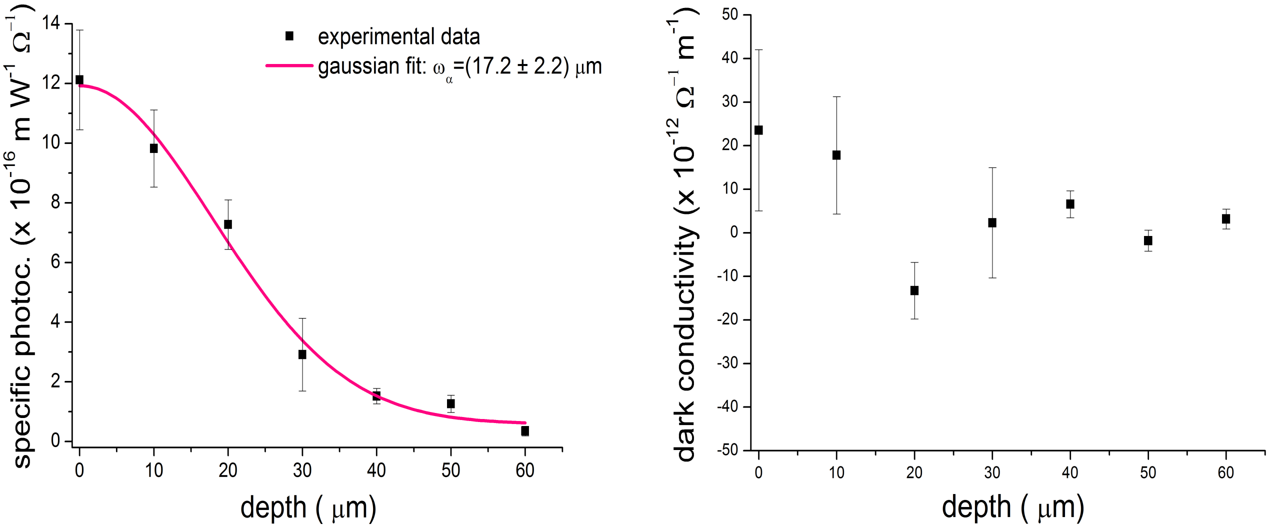

(a) *(b)*

Figure 5.13: *In-depth profiles of the specific photoconductivity (a) an the dark conductivity (b). The HWHM of the specific photoconductivity is reposted and, within the errors, it is comparable with the values obtained in the previous section relative to the photoconductivities realized at different intensities.*

ferent intensities, the in-depth profiles of both the specific photoconductivity α and the dark conductivity σ_{dark} are derived. The obtained results are shown in fig. 5.13 where it is possible to notice that α has the same half width at half maximum of the photoconductivity σ_{ph} (see fig. 5.17), whereas the dark conductivity has not a clear depth dependence and, within the errors, it is always compatible with zero along the whole iron concentration profile.

To obtain a more accurate estimate of the dark conductivity, a direct measurement has been realized, by estimating the time decay of an hologram in absence of light. Since the dark conductivity increases with increasing iron content, to obtain the maximum value of σ_{dark} present in the sample it was measured near the surface of the crystal, where the dopant concentration is higher. Thus, after the recording of an hologram just below the doped edge of the sample, realized by using the maximum intensity $\mathrm{I} = 35\,\mathrm{W/m}^2$, the beam 1 was stopped, while the time evolution of the diffracted beam 2 was investigated, by attenuating the incident beam 2 by a factor 200 and sampling, for few seconds, the intensity of its diffracted component at appropriate time intervals. The time evolution of space-charge field is reported in fig. 5.14, where it is evident that after more than one week the grating is not completely erased and the E_{sc} has not yet reached the zero. Remembering that the erasing process is described by the relation 4.26 where, in this case, $\tau_{sc} \equiv \tau_{dark}$, for $\mathrm{t} \to 0$ the following equation is valid

$$E_{sc} \simeq E_{sc}^{sat}\left(1 - \frac{t}{\tau_{dark}}\right) \tag{5.13}$$

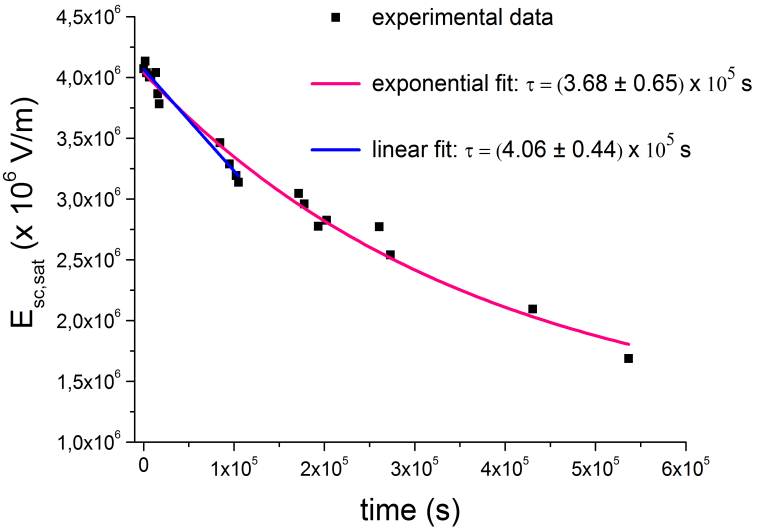

Figure 5.14: *Erasing curve of an hologram in the dark. The time constants derived by a linear fit and an exponential one are reported.*

and thus a linear fit of the first experimental data can be performed. The time constants obtained by this linear interpolation and by fitting all the experimental data with an exponential function are respectively $\tau_{dark,1} = (4.06 \pm 0.44)\,\mathrm{x}\,10^5\,\mathrm{s}$ and $\tau_{dark,2} = (3.68 \pm 0.65)\,\mathrm{x}\,10^5\,\mathrm{s}$. Thus, in the zone of the sample where the iron concentration is higher the decay time constant in the dark is about 4.5 days, which leads to $\sigma_{dark} = (6.4 \pm 1.32)\,\mathrm{x}\,10^{-16}\,\Omega^{-1}\mathrm{m}^{-1}$.

5.4.3 The space charge field

As for the congruent undoped and the as-diffused samples, also for the reduced crystal in-depth profiles of the space charge field E_{sc} are estimated. Furthermore in this sample the dependence of the photorefractive parameters on the light intensity is taken into account and three profiles are determine at different intensities ($35\,\mathrm{W/cm}^2$, $11.1\,\mathrm{W/cm}^2$ and $5.5\,\mathrm{W/cm}^2$), whose results are reported in fig. 5.15. As reported in eq. 5.9, in the one center model with simplified solutions the saturation values of the space charge field depends only on the concentration of empty traps and not on the intensity of the light pattern. This is confirmed by experimental data which show how the space charge field profiles obtained at three different intensities are perfectly comparable within the errors.

Moreover, it is also expected that these profiles have the same HWHM of the iron concentration in-depth one and almost the same values of E_{sc}^{sat} observed in the case of the as-diffused sample, because both temperature of the reducing treatment is too low to allow further diffusion of the dopant inside the crystal[3] and in this sample the

---

[3] See section 2.2.1

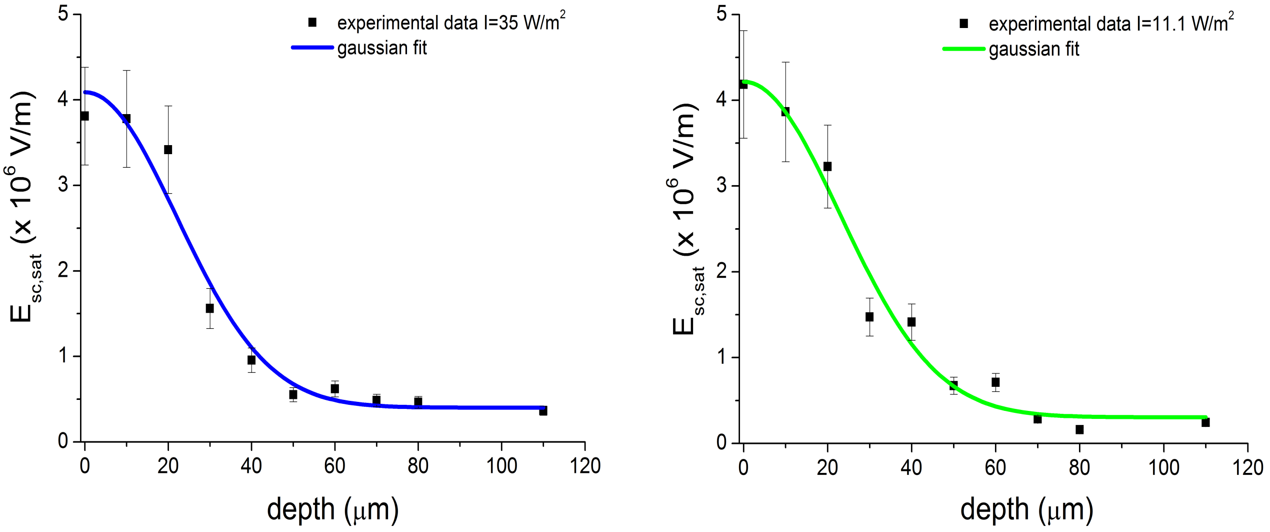

(a) (b)

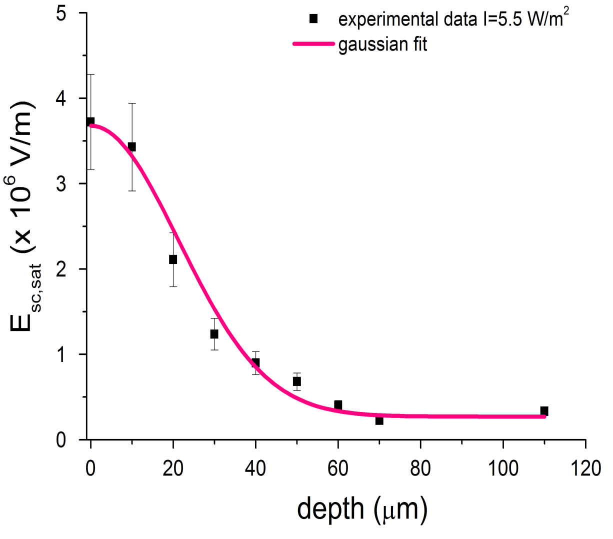

(c)

I (x 10^4 W/m^2)	E$_{sc}^{sat}$ at 0 μm (x 10^6 V/m)	ω_E^{corr} (μm)
35 ± 4	3.8 ± 0.5	22.1 ± 2.0
11.1 ± 1.4	4.2 ± 0.6	22.9 ± 1.8
5.5 ± 0.7	3.7 ± 0.5	21.3 ± 1.4

Figure 5.15: *In-depth profiles of the space charge field at 35 W/cm^2 (a) 11.1 W/cm^2 (b) and 5.5 W/cm^2 (c)*

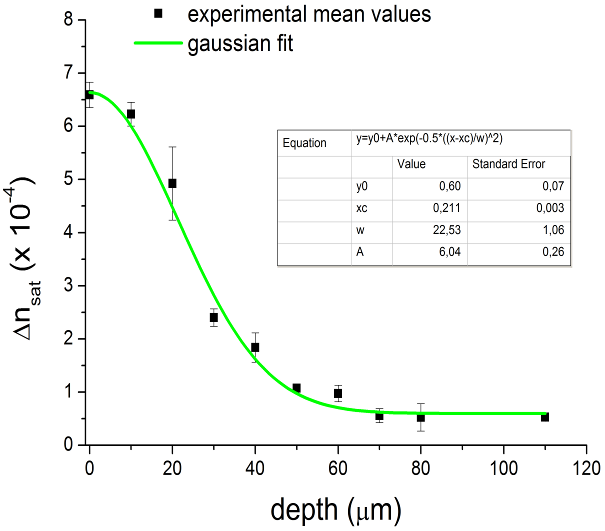

depth (μm)	Δn^{sat} (x10^{-4})
0	6.6 ± 0.2
10	6.2 ± 0.2
20	4.9 ± 0.7
30	2.4 ± 0.1
40	1.8 ± 0.3
50	1.1 ± 0.1
60	0.97 ± 0.16
70	0.56 ± 0.13
80	0.53 ± 0.26
110	0.53 ± 0.06

Figure 5.16: *In-depth profile of the induced refractive index change and relative values obtaining by performing holographic measurements in a reduced Fe:LN sample.*

amount of Fe^{2+} is too small[4] to significatively change the Fe^{3+} in-depth profile with respect to the as-diffused crystal. The HWHM of each profile of E_{sc}^{sat}, corrected by the convolution of the probe size, are reported in fig. 5.15 and the mean value results $(22.1 \pm 1.3)\,\mu$m, which agree with that one relative to the dopant distribution inside the sample. On the contrary, considering the maximum space charge field at the surface of the crystal, its mean values $(3.90 \pm 0.17)\,\mathrm{x}\,10^6\,$V/m is slightly lower than that observed in the as-diffused sample, but in any case it is compatible, within the errors, with the value of E_{sc}^{sat} expected for a reduction degree of $[Fe^{2+}]/[Fe^{3+}] = 4.6\%$, that is $E_{sc}^{sat} = (4.1 \pm 0.4)\,\mathrm{x}\,10^6\,$V/m.

Concerning the induced refractive index change, the means of values obtained at each depth for the three different intensities are reported in fig. 5.16, showing, as in the case of the space charge field, a lower value of Δn_{sat} at the crystal surface respect to the oxidized sample, which can be justified considering a decrease of the Fe^{3+} due to the reducing treatment. Instead, both the value of the space charge field and that of the induced refractive index change measured in the undoped part of the crystal ($110\,\mu$m below the crystal surface) are the same found in the as-diffused sample, showing that in the bulk material the native concentration of the empty traps has not been appreciably changed by the reducing treatment. This fact will be confirmed by the study of the photoconductivity.

5.4.4 The photoconductivity

As already proved at the beginning of this section, the photoconductivity grows linearly with intensity, as expected by the band transport model with one photore-

---

[4] It has to remember that for this sample the optical absorption measurements have demonstrated that $[Fe^{2+}] = 4.6\% \cdot [Fe^{3+}]$.

fractive center and once more confirmed by the photoconductivity profiles performed at 5.5 - 11.1 - 35 $\mathrm{W/m^2}$ (see fig. 5.17). It is immediately evident that also in this sample the photoconductivity is not constant along the iron concentration profile, as previously observed in the as-diffused crystal, confirming that the distribution of Fe^{2+} does not follow that of empty traps. Moreover, it must be underlined that the HWHM obtained by gaussian fits and corrected for the convolution with the probe size (table in fig. 5.17), are significatively larger in the reduced sample than in the as-diffused one. To make a comparison, the values of ω_{pc} measured at 35 $\mathrm{W/m^2}$ in the as-diffused sample and the reduced one can be took into account: they are respectively $(3.2 \pm 0.9)\,\mu$m and $(17.1 \pm 3.0)\,\mu$m, so it is evident that the reducing treatment, performed at 500°C for 1 h, has not only increased the amount of Fe^{2+}, but also changed the $[\mathrm{Fe}^{2+}]/[\mathrm{Fe}^{3+}]$ profile inside the doped layer. Indeed, since the total reduction degree of the sample is too low to induce a remarkable change of Fe^{3+} respect to the total iron concentration profile, the increasing of ω_{ph} in the reduced sample has to be attributed only to a variation of the profile of Fe^{2+}.

Furthermore, it is interesting to notice that the photoconductivity measured with the maximum intensity in the undoped zone of the crystal, at 110 μm below the surface of the sample, is $\sigma_{bulk} = (0.050 \pm 0.005)\,\Omega^{-1}\,\mathrm{m}^{-1}$, that is the same value obtained in the as-diffused sample. Therefore the native photorefractive centers have not been reduced during the thermal treatment in $\mathrm{Ar{+}H_2}$, indicating that the electrons provided by the reducing gas have not reached the undoped crystal, but they stopped before, in the iron doped layer.

Discussion

All these experimental evidences induce to suppose that, at least after a reduction time of 1 hour, the electrons responsible for the reduction of Fe^{3+} into Fe^{2+} do not move inside the material trying to achieve a constant reduction degree over all the sample, but they obey a sort of diffusion law which leads them to be more concentrated in the areas with higher dopant amount.

A further confirmation to this suggestion is that the values of photoconductivity obtained at the beginning and at the end of the doped layer are respectively higher and lower than the expected values. Indeed if the reduction degree of an iron doped lithium niobate sample is $\mathrm{Fe}^{2+}/\mathrm{Fe}^{3+} \simeq 4.6\%$, then the photoconductivity at 35 $\mathrm{W/m^2}$ should be $\sigma_{pc} \simeq 1.6\,\mathrm{x}\,10^{-10}\,\Omega^{-1}\mathrm{m}^{-1}$, whereas the experimental values at 0 and 70 μm from the surface of the sample are $\sigma_{ph,0} = (4.27 \pm 51)\,\mathrm{x}\,10^{-10}\,\Omega^{-1}\mathrm{m}^{-1}$ and $\sigma_{ph,70} = (6.52 \pm 0.65)\,\mathrm{x}\,10^{-12}\,\Omega^{-1}\mathrm{m}^{-1}$, which provide respectively a reduction degree of 12.2% and 0.18%. Thus it seems that the reducing electrons has been mainly captured by Fe^{3+} atoms located near the surface, where iron concentration is higher, while only few of them has traveled up to the end of the dopant region. However, in principle it could be

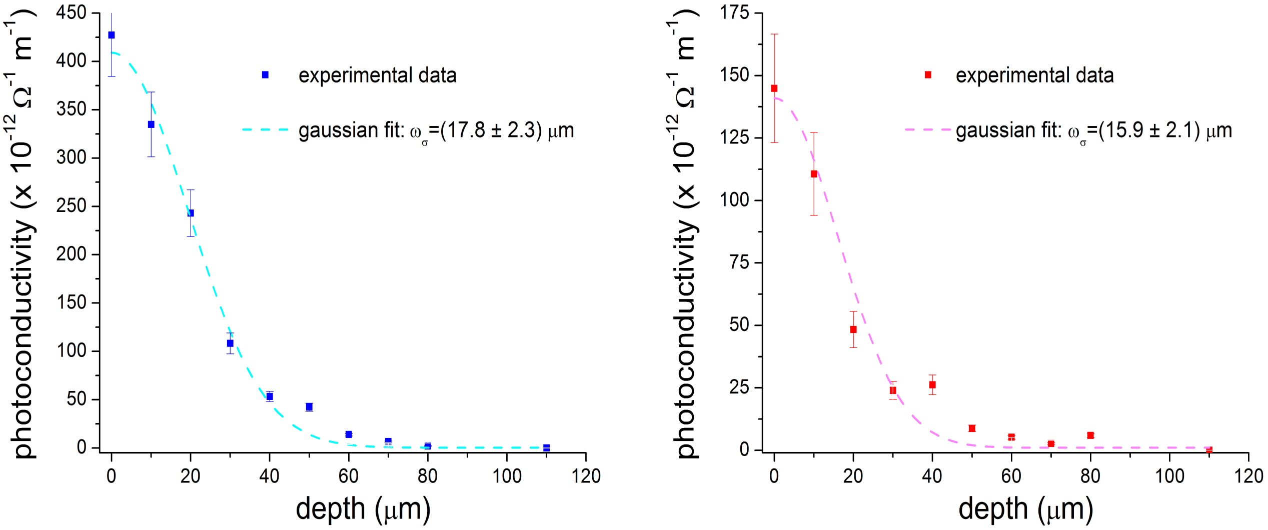

(a) *(b)*

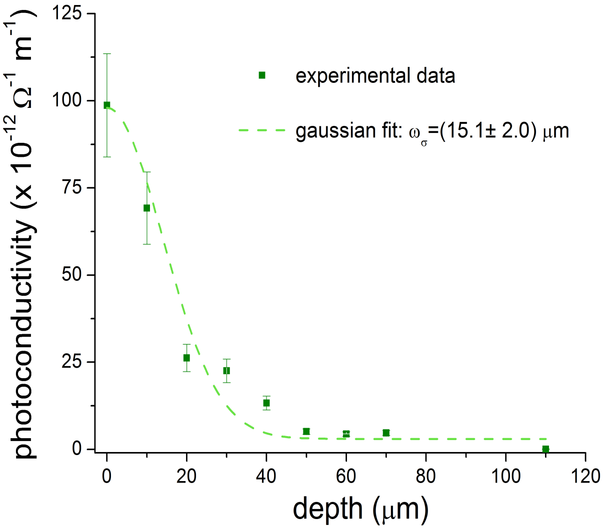

(c)

I (x 10^4 W/m^2)	ω_σ^{corr} (μm)
35 ± 4	17.1 ± 3.0
11.1 ± 1.4	15.1 ± 2.7
5.5 ± 0.7	14.2 ± 2.6

Figure 5.17: *In-depth profiles of the photoconductivity at 35 W/cm^2 (a) 11.1 W/cm^2 (b) and 5.5 W/cm^2 (c) . The HWHM obtained by gaussian fits are listed in the table.*

also possible that the increase of the measured photoconductivity near the surface of the sample is caused by an anomalous increase of the dark conductivity, so that the relation $\sigma_{tot} = \epsilon\,\epsilon_0/\tau_{sc} \simeq \sigma_{ph}$ is no more valid and to obtain the correct photoconductivity the value of σ_{dark} has to be taken into account, subtracting it to σ_{tot}. However, this is not our case, since, as previously discussed in subsection 5.4.2, in our samples the measured value of the dark conductivity is $\sigma_{dark} = (6.4 \pm 1.32)\,\mathrm{x}\,10^{-16}\,\Omega^{-1}\mathrm{m}^{-1}$, which is significatively smaller than the value of σ_{ph}. Thus the approximation $\sigma_{tot} \simeq \sigma_{ph}$ is experimentally verified and only the distribution of Fe^{2+} can be considered the responsible for the behavior observed in the in-depth profile of the photoconductivity.

5.4.5 The photovoltaic current

In the subsection 5.4.2 it was shown that the dark conductivity is negligible with respect to the photoconductivity, thus to understand the in-depth profile of σ_{ph}, the $[\mathrm{Fe}^{2+}]$ profile has to be taken into account.
As already mentioned in the fourth chapter, the photovoltaic current j_{ph} is directly proportional to the concentration of filled traps $\mathrm{N}_{Fe^{2+}}$, according to the following equation

$$j_{pv} = k_G\, s_{Fe}\, N_{Fe^{2+}}\, I \tag{5.14}$$

Thus to obtain information on the Fe^{2+} profile inside the reduced sample, the photovoltaic current was investigated, trying in a second time to relate the new results with those previously discussed.
As reported in eq. 5.8 the photovoltaic current can be estimated by the time derivative of space-charge field at the beginning of the recording process, thus the initial part of each experimental curve was fitted with the linear function $\mathrm{y} = \mathrm{m\,t}$, deriving j_{ph} from the slope m of the line ($j_{ph} = \mathrm{m}\,\epsilon_{33}\,\epsilon_0$). The experimental results are shown in fig. 5.18 where, as expected by eq. 5.14, the photovoltaic current increases with the intensity of the incident beams. Moreover it is immediately evident that the half width at half maximum of the profile of j_{phv} is smaller than those relative to the photoconductivities and to the dopant concentration, confirming the assumption that the profile of Fe^{2+} differs from that of Fe^{3+}. When the equilibrium state is reached the relation $\mathrm{E}_{sc}^{sat} = -\,\mathrm{E}_{phv}$, so the absolute value of the photovoltaic current can be also derived by exploiting the Ohm's law, $\mathrm{j}_{phv} = \sigma_{ph}\,\mathrm{E}_{sc}^{sat}$, comparing the obtained values with those previously derived by eq. 5.8. As it is possible to notice in fig. 5.19, the profiles achieved with these two independent methods are perfectly in agreement and by fitting them with a guassian function the HWHM is derived for each curve, verifying that it is the same at each intensity used. Remembering the linear relation between the photovoltaic current and the concentration of filled traps, it follows that the in-depth dependence of j_{phv} can be exploited to obtain the profile of

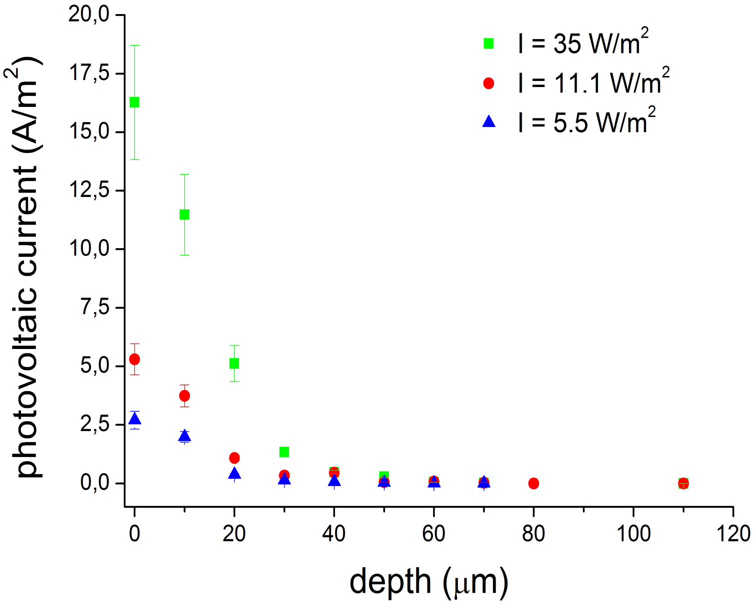

Figure 5.18: *In-depth profiles of the photovoltaic current obtained at 35 - 11.1 - 5.5 W/m^2.*

the concentration of Fe^{2+} inside the sample. Indeed, if a gaussian distribution of Fe^{2+} atoms is assumed, the concentration of filled traps at each depth can be simulated by knowing the half width at half maximum of the gaussian function and the total amount of Fe^{2+} inside the doped layer, corresponding to the integral of the Fe^{2+} profile. As HWHM the average of the values listed in fig. 5.19 can be used ($\omega_j = (10.8 \pm 1.6)$), while the total number of filled traps is provided by the optical absorption measurement ($[_{Fe^{2+}}] \simeq 2.4\,\mathrm{x}\,10^7\,\mu\mathrm{m}^{-2}$). The simulated profile of the filled traps concentration [Fe^{2+}] is reported in fig. 5.20 (a), where they are also shown the total dopant concentration distribution and the [Fe^{3+}] one, derived as difference between [Fe$_{tot}$] and [Fe^{2+}]. The distribution of Fe^{2+} atoms is very narrow and at only 20 μm from the crystal surface the filled traps are practically absent, while its surface concentration is $(1.66 \pm 1.0)\,\mathrm{x}\,10^{24}\,\mathrm{m}^{-3}$, leading to a reduction degree of $(9.88 \pm 5.94)\,\%$. Moreover, by plotting the ratio between the simulated distributions of filled and empty traps, the reduction degree profile [Fe^{2+}]/[Fe^{3+}] is obtained (fig. 5.20 (b)), whose HWHM, derived by a gaussian fit, is (13.50 ± 0.01), in agreement with the values of HWHM relative to the photoconductivity profile. Considering the equations (5.10 - 5.14), from the experimental values of the photovoltaic current and the photoconductivity the reduction degrees at the surface of the sample (respectively named rd$_1$ and rd$_2$) can be derived. The obtained values are listed in table 5.5 and it is possible to notice that they are mutually consistent and, above all, comparable with the reduction degree derived by the simulation of the [Fe^{2+}] profile. Thus the increasing of the photoconductivity at the surface of the crystal and its

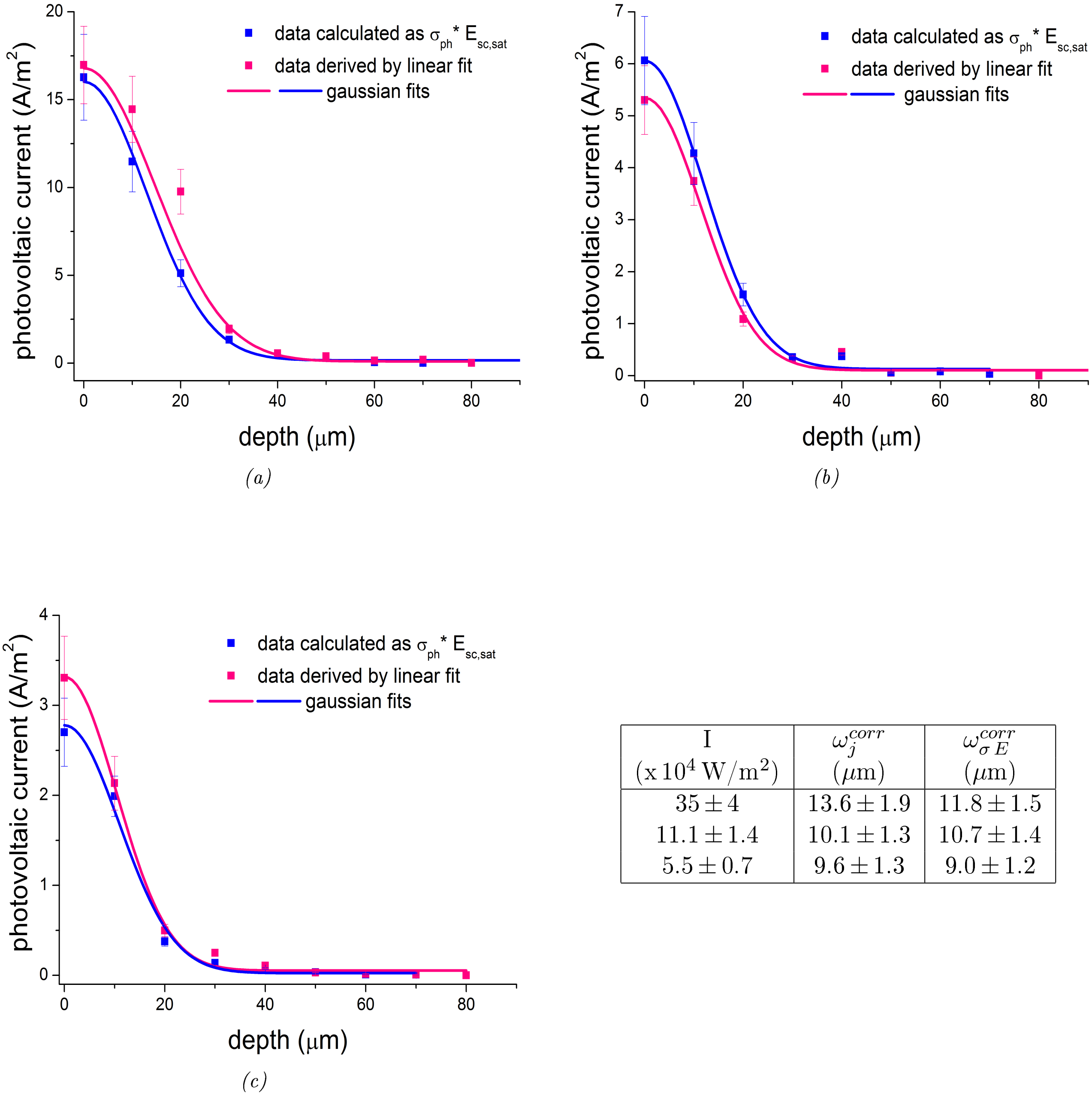

(a)

(b)

(c)

I (x 10^4 W/m^2)	ω_j^{corr} (μm)	$\omega_{\sigma E}^{corr}$ (μm)
35 ± 4	13.6 ± 1.9	11.8 ± 1.5
11.1 ± 1.4	10.1 ± 1.3	10.7 ± 1.4
5.5 ± 0.7	9.6 ± 1.3	9.0 ± 1.2

Figure 5.19: *In-depth profiles of the photovoltaic current at 35 W/cm^2 (a) 11.1 W/cm^2 (b) and 5.5 W/cm^2 (c). The valued of j_{ph} are derived by using two independent methods: by linearly fitting the first part of the recording curve and by exploiting the Ohm's law at the equilibrium state.*

non constant profile inside the sample are completely justify by a filled traps distribution which does not follow that of empty traps, but it is more confined near the external surface of the material.

Finally, in fig. 5.20 it is evident that the HWHM relative to Fe^{3+} is the same of the distribution of Fe$_{tot}$, as confirmed by the in-depth profiles of the space-charge field discussed previously. However, due to the confinement of Fe^{2+}

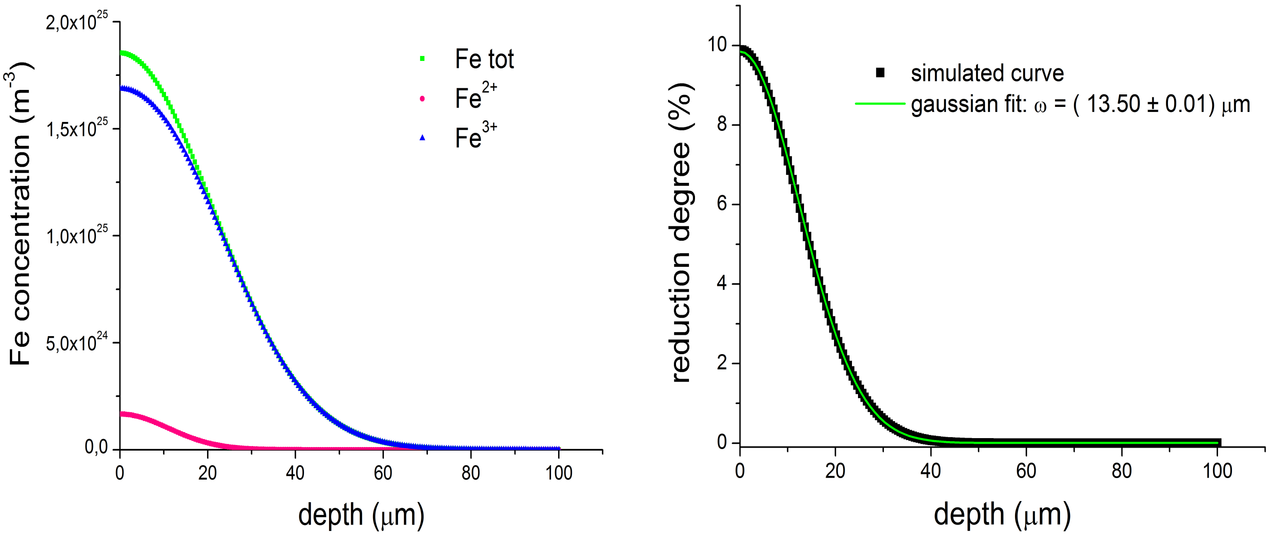

(a) *(b)*

Figure 5.20: *In-depth profiles relative to [Fe^{2+}], [Fe^{3+}] and [Fe$_{tot}$] (a) and to the corresponding reduction degree [Fe^{2+}]/ [Fe^{3+}] (b).*

I (x10^4 W/m^2)	reduction degree rd$_1$(%)	reduction degree rd$_2$ (%)
35 ± 4	9.6 ± 1.8	12.2 ± 2.3
11.1 ± 1.4	9.9 ± 1.9	13.9 ± 2.5
5.5 ± 0.7	10.7 ± 2.0	17.7 ± 3.4

Table 5.5: *Surface reduction degrees calculated by the photovoltaic currents j_{phv} (rd$_1$) and by the photoconductivity σ_{ph} (rd$_2$).*

near the sample surface, it is expected that the concentration of Fe^{3+} is quite different respect to that of Fe$_{tot}$ in the first micrometers below the surface of the crystal, leading to a decreasing of E$_{sc}^{sat}$ which is directly proportional to the amount of acceptor centers. Indeed if the maximum saturation value of the space-charge field in the as-diffused sample is (4.3 ± 0.4) x 10^6 V/m, considering a reduction degree of 9.88% at the surface of the material the corresponding E$_{sc}^{sat}$ should be (3.9 ± 0.4) x 10^6 V/m which is exactly the same mean value experimentally observed in the reduced sample ((3.9 ± 0.2) x 10^6 V/m). The same estimate can be performed considering the induced refractive index change, that, with [Fe^{2+}]/[Fe^{3+}] = 9.88%, should be about 6.58 x 10^{-4}, once again in agreement with the value found experimentally ((6.6 ± 0.2) x 10^{-4}).

Conclusions

In summary, the photorefractive characterization of an as-diffused Fe:LN sample and a reduced one has pointed out that the reduction degree $[\mathrm{Fe}^{2+}]/[\mathrm{Fe}^{3+}]$ is not constant along the iron concentration profile, contrary to what was assumed up to now in the literature concerning iron doped lithium niobate crystals realized by thermal diffusion. Indeed the profile of the photoconductivity both in the as-diffused sample and in the reduced one has an in-depth dependence which can be explained considering a Fe^{2+} distribution which is not the same of the empty traps. Moreover the increasing of the HWHM of the filled traps after the reducing treatment suggests that the incorporation of the reducing electrons in the sample occurs obeying a sort of diffusion law, which induces a larger concentration of e^- (and thus of Fe^{2+}) near the surface of the sample, where the electrons are provided by the H_2 molecules present in the annealing gas. This diffusion process is confirmed by another technique which is independent by the holographic one: recent and preliminary studies realized on the same samples by performing Raman spectroscopy measurements are briefly presented in appendix B and show how with longer reducing treatments the "diffusion depth" of $[\mathrm{Fe}^{2+}]$ increases, reaching after some hours the same depth of the dopant concentration profile. Further investigations will be performed exploiting this technique, in order to verify the validity of the experimental results obtained by holographic measurements.

Chapter 6

Conclusion and perspectives

The photorefractive effect is currently under intense investigations thanks to its potential for application in optical integrated system and in particular for the development of optical memories and holographic recording substartes. Thus, the work developed in this thesis is aimed to study the structural and photorefractive properties of congruent $LiNbO_3$ doped with Fe by thermal diffusion, which is one of the most promising materials for the realization of photorefractive stages in integrated optoeletronic devices.
In the first part of this work the structure of the diffused Fe:$LiNbO_3$ samples have been investigated, both during the entire diffusion process and in the completely diffused crystals. Concerning the diffusion mechanisms, the High Resolution X-Ray Diffraction (HR-XRD) technique has definitely demonstrated the formation of an intermediate crystallographic phase during the iron incorporation process in the lithium niobate substrate, which acts as source of Fe atoms for the underlying structure. Moreover, the chemical composition of this interlayer has been finally clarified, establishing that it is an iron niobate layer ($FeNbO_4$) which belongs to the Fe_2O_3 - Nb_2O_5 system. Thus this result answers to a question that was not clear in the literature. Furthermore, it has been investigated the iron site occupation in the lithium niobate matrix, because a precise knowledge of the dopant lattice site is essential for tuning and understanding the photorefractive properties of the material. Even if the lattice position of iron in bulk Fe:LN samples is well known, this study on diffused sample has been never done before and it appears mandatory, due to the complete different dopant incorporation mechanism with respect to the bulk samples. By means of ion beam analysis we have definitively demonstrated that also in diffused sample, for dopant concentrations up to 1 % mol (about 1.8×10^{26} at/m^3), iron locates at the lithium site, regardless of its valence state. In addition micro-raman spectroscopy and polaron luminescence have pointed out that when Fe atoms are incorporated in the lithium position, they push away the niobium antisites to their regular site, leading to a decrease of the

concentration of Nb_{Li} in the doped layer. Finally a linear relation between the reduction degree and the perpendicular mismatch at the surface of Fe-diffused samples has been found, showing that the cristallographic structure of the lithium niobate is more affected by Fe^{3+} than Fe^{2+}, probably due to the fact that the charge difference between the dopant ions and the Li^{+} ones is higher in the former case than in the latter one.

In the second part of this thesis a great attention was paid to the investigation of the photorefractive properties of diffused iron-doped lithium niobate crystals. In the past Fe-diffused $LiNbO_3$ samples have been study in a waveguide fashion, deriving only informations averaged over the entire channel depth. On the contrary a detailed investigation of the photorefractive properties along the iron concentration profile has never realized before and this study is certainly fundamental to achieve the knowledges necessary to properly exploit this material as a photorefractive optical device. Since depth resolved techniques to measure the photorefractive properties have not been published yet, a new optical set-up has been designed and built-up. After several improvements and relative characterizations of the whole optical circuit, a light probe with a vertical waist of $(5.1 \pm 0.7)\mu$m has been achieved, which allows to perform holographic measurements only in a limited area of the iron doped layer. In this way it has been possible to probe photorefractive properties in different regions of the doped area, deriving for the first time in depth-profiles of the main parameters involved in the photorefractive effect. First of all, the validity of this study have been proved by comparing the results obtained on congruent nominally pure lithium niobate crystals with those reported in literature, which are mutually consistent. Then, after demonstrating the plausibility of the band transport model with one photorefractive center for intensities up to $35\,\mathrm{W/cm^2}$, the corresponding theory has been used to examine the photorefractive response of Fe-diffused samples with two different reduction degree $[Fe^{2+}]/[Fe^{3+}]$, respectively $(0.18 \pm 0.12)\,\%$ and $(4.6 \pm 2.9)\,\%$. The potential of this technique lies in the possibility to directly correlate at each depth the iron concentration distribution inside the sample with the corresponding holographic measurement results, so that by properly tuning the parameters of the sample preparation procedure, in the future it will be possible to obtained the desired light-induced refractive index change profile. Moreover, this innovative depth-resolved study paves the way for local studies of other important physical properties of the diffused layer. For instance, new interesting insights on the reduction mechanism used to increase the content of filled traps Fe^{2+} present in the samples have been pointed out in this work. Indeed, despite of the optical absorption techniques where the mean values of of the filled and empty traps concentrations over all the doped layer are given, by mean of this new depth-resolved characterization significant informations on the Fe^{2+} concentration profile have been derived.

Being the photovoltaic current proportional to the concentration of Fe^{2+}, its depth dependence can be directly related to the distribution inside the crystal of reducing electrons provided by the post-diffusion thermal annealing in $Ar + H_2$. The appealing result is that after one hour at 500°C in a reducing gas mixture the electrons are not homogeneously distributed over the entire doped layer, but they are confined in a area about $10\,\mu$m deep below the crystal surface. This means that in this reduced layer the reduction degree is higher than the mean values obtained by the optical absorption method, as confirmed by the photovoltaic current profile, whose surface values are larger than the awaited ones. Besides the photovoltaic current, also the photoconductivity σ_{ph} values support the above mentioned results, because they are not constant along the doped layer, presenting on the contrary an in-depth dependence, due to the non uniform reduction degree along the iron concentration distribution. In particular, the reduction degree at the surface of the sample have been estimated to be about $12\,\%$, that is three times the measured mean value. Moreover, it has been observed that after the diffusion process the undoped substrate presents a smaller content of filled traps than before the iron incorporation, an effect which is probably due to the movement, during the high temperature annealing, of electrons from the native Fe^{2+} centers towards regions characterized by an higher iron concentration, that is the doped layer. Furthermore, after the reducing thermal annealing, which leaves unchanged the dopant distribution inside the crystal, the photovoltaic current not only presents higher values at the surface, as expected due to the increase of Fe^{2+}, but also a deeper profile with respect to the as-diffused samples. All the above mentioned results suggest that the reduction mechanism of our Fe:LN samples occurs as a diffusion process of reducing electrons, which at the beginning accumulate near the surface, where they are provided by the H_2 molecules present in the annealing gas and the iron concentration is larger. Other experimental evidences, by means of Raman spectroscopy and optical absorption techniques, support this hypothesis, showing both that the amount of electrons incorporated in the doped layer during the reducing thermal treatment depends significatively on the iron concentration profile and that the HWHM of the final filled traps distribution progressively increases with longer reducing annealing. After this interesting preliminary results, the physical mechanism underlying the reduction process should be further investigated by performing systematic in-depth holographic measurements on a set of diffused Fe:$LiNbO_3$ samples characterized by both different dopant profiles and different parameters (time and temperature) of the reduction thermal treatment.

Besides the mentioned investigations, the described depth-resolved analysis method could allow to obtain new results concerning the structural and photorefractive properties of the doped layer. In particular, by exploiting the linear

relation between the vertical mismatch and the reduction degree presented in this work and by knowing the total iron concentration profile and the Fe^{2+} one, respectively obtained by SIMS and holographic measurements, in principle it is possible to derive the in-depth vertical mismatch profile of our Fe:LN crystals, achieving in this way a complete knowledge of the structural properties at each depth along the doped layer.
Moreover, as far as the application of iron doped substrates is concerned, an integrated optical devices is also constituted by waveguides, which allow to transmit the signal from an optical component to another one of the system. In particular, in diffused Fe:LN crystals planar waveguides are usually created by performing ion implantation with C, O, Cl or other elements, followed by a subsequent recovering thermal treatment. This preparation procedure may affect both the iron concentration profile and its reduction degree, thus the new in-depth measurements discussed in this work could be used to investigate the structural and compositional changes caused by the ion implantation technique. Finally, by using higher light intensities, at which the band transport model with two photorefractive centers is involved, the in-depth holographic measurements will be used to study the distribution of the niobium antisite, Nb_{Li}, in the doped layer and how their concentration profile can affect the structural properties of the samples.

Concerning the employment of diffused $Fe:LiNBO_3$ crystal as optical photorefractive device, such as holographic memories, reflection Bragg grating, interference filters and so on, a fundamental requirement is the permanence of the written holographic grating. Indeed a developed hologram is erased by the dark conductivity with dark storage times which range from months to minutes, depending on both the iron concentration and the amount of hydrogen in the crystal. In particular in Fe:LN samples with an iron concentration up to about 0.1 %mol, as it is our case, the proton compensation dominates the dark decay process, with a time constant which is inversely proportional to the H^+ content of the material. Holographic measurements performed on our reduced samples have pointed out a dark time constant of about 4 - 5 days, which underlines the necessity to further improve the samples preparation in order to decrease the dark conductivity in the case that permanent memories are needed. For spatial applications, instead, these times are compatible with the typical ones necessary to recover the data, especially when the device is put inside a launched probe in the stratosphere. For instance, the concentration of the mobile ions can reduced by suitable thermal annealing, as reported in [18], where thermal treatments at 400°C in dry atmosphere are proposed to remove hydrogen from the substrate. However, the best permanence of the holographic gratings is achieved by thermal fixing, which allows to obtain lifetimes of the order of year[60, 61]. In the thermal fixing the samples are heated, during or after illumination, to a temperature of typically 180°C. At this temperature ions become mobile and they can drift in the space-charge field, compensating the electronic charge pattern. Then, when the crystal are cooled to room temperature, the ion mobility is significatively reduced and the ionic pattern results stable for many years. Therefore, it is mandatory to improve the quality of our photorefractive Fe-diffused lithium niobate samples by including in the sample preparation procedure the thermal fixing process, with consequent detailed investigations of the final achieved structural and, above all, photorefractive properties of the material.

Appendix A

The gaussian beam

In the present appendix, the basic knowledges on gaussian beams are presented, in order to help the reader to better understand the set-up characterization and the final size of the probe discussed in chapter 4. However for deeper informations the book of Saleh and Teich[54] is recommended.
A wave is said to be paraxial if its wavefronts normals are paraxial rays, that is they make a small angle with respect to the optical axis of the system, and lie closed to the axis throughout the system. The complex amplitude of a paraxial wave is

$$U(\mathbf{r}) \, = \, A(\mathbf{r}) exp\,(-j\,k\,z) \tag{A.1}$$

where $exp\,(-j\,k\,z)$ is a plane wave and $A(\mathbf{r})$ is a slowly varying function of the position. The complex envelope of the paraxial wave $A(\mathbf{r})$ has to satisfy the paraxial Helmholtz equation $\partial^2 A/\partial x^2 \, + \, \partial^2 A/\partial y^2 \, - \, j\,2\,k\partial A/\partial z \, = \, 0$ and the derived solutions are the paraboloidal wave and the ***Gaussian beam***. The complex envelope of the gaussian beam is given by

$$A(\mathbf{r}) = \frac{A_1}{q(z)} \mathtt{exp} \left[-jk\frac{\rho^2}{2q(z)} \right] , \qquad q(z) \, = \, z + jz_0 \tag{A.2}$$

where the parameter z_0 is known as ***Rayleigh range***. To obtain the amplitude and the phase of this complex envelope, the complex function $1/\mathrm{q(z)} = 1/(\mathrm{z} + \mathrm{j}\,\mathrm{z}_0)$ can be written as a sum of a real and an imaginary part, defining the new real function R(z) and W(z)

$$\frac{1}{q(z)} = \frac{1}{R(z)} - j\frac{\lambda}{\pi W^2(z)} \tag{A.3}$$

which represent respectively the wavefront radius of curvature and the beam width. Substituting the equation A.3 into A.2 the complex amplitude $U(\mathbf{r})$ of the gaussian beam is obtained

$$U(\mathbf{r}) = A_0 \frac{W_0}{W(z)} \mathtt{exp}\left[-\frac{\rho^2}{W^2(z)}\right] \mathtt{exp}\left[-jkz - jk\frac{\rho^2}{2R(z)} + j\zeta(z)\right] \tag{A.4}$$

with

$$W(z) = W_0 \left[1 + \left(\frac{z}{z_0}\right)^2\right]^{1/2} \tag{A.5}$$

$$R(z) = z\left[1 + \left(\frac{z_0}{z}\right)^2\right] \tag{A.6}$$

$$\zeta(z) = \mathtt{tan}^{-1}\left(\frac{z}{z_0}\right) \tag{A.7}$$

$$W_0 = \left(\frac{\lambda z_0}{\pi}\right)^{1/2} \tag{A.8}$$

$$A_0 = \left(\frac{A_1}{j\, z_0}\right) \tag{A.9}$$

The intensity of the beam is defined as $I(\mathbf{r}) = |U(\mathbf{r})|^2$ and thus it is a function of the axial and radial distances z and $\rho = (x^2 + y^2)^{1/2}$

$$I(\rho, z) = I_0 \left[\frac{W_0}{W(z)}\right]^2 \mathtt{exp}\left[-\frac{2\rho^2}{W^2(z)}\right] \tag{A.10}$$

On the beam axis ($\rho = 0$) the intensity has its maximum value I_0 for z=0 and drops gradually for increasing z, reaching half of I_0 for z=$\pm z_0$.

The axial dependence of the beam width is governed by the eq. A.5 and it assumes its minimum values W_0 at the plane z=0. W_0 is defined as the *beam radius*, thus the *spot size* is $2W_0$, and it increases gradually with z, reaching the value $\sqrt{2}W_0$ at the Rayleigh range z_0. The axial distance within which the beam radius is smaller than $\sqrt{2}W_0$ is defined as *depth of focus*, and thus it is twice the Rayleigh range

$$2z_0 = \frac{2\pi W_0^2}{\lambda} \tag{A.11}$$

Thus when a gaussian beam is focused to a small spot size, the depth of focus is short and the plane of focus must be located with greater accuracy. Moreover a small beam size and a long depth of focus can not be achieved simultaneously, unless the wavelength of light is enough short.
Far from the beam center, at $z \gg z_0$, the beam radius grows approximatively linearly with z, defining a cone with an half-angle θ (fig. A.1), within which the

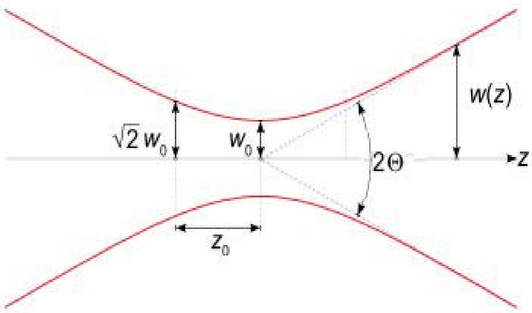

Figure A.1: *Schematic representation of a gaussian beam and its main feature: the beam radius* W_0*, the Rayleigh range* z_0*, the angular divergence* θ*.*

86% of the beam power is confined. The angular divergence is defined as

$$\theta = \frac{2}{\pi}\frac{\lambda}{2\,W_0} \tag{A.12}$$

thus more the beam is squeezed, more is the increase of the divergence.

A lens, or a sequence of lens, can be used to reshape a gaussian beam without changing its gaussian nature. If a lens is placed at the waist of the gaussian beam, as shown in fig. A.2, the transmitted beam is focused at the distance z' with a new waist radius W'$_0$, given by the following relations

$$W_0' = \frac{W_0}{\left[1+(z_0/f)^2\right]^{1/2}} \tag{A.13}$$

$$z' = \frac{f}{1+(f/z_0)^2} \tag{A.14}$$

In particular if the depth focus of the incident beam is longer than the focal length f of the lens, then the above equations become

$$W_0' \simeq \frac{\lambda}{\pi\,W_0} f \qquad z' \sim f \tag{A.15}$$

and the transmitted beam is focused at the focal length of the lens, as in the case of incident parallel rays. This occurs because at its waist the gaussian beam is approximatively a plane wave, an important feature which has been also exploited in this Ph.D. work to analyze the experimental data discussed in chapter 5. Finally, considering an incident beam whose spot size is large as the diameter of the lens, if a focused beam spot as small as possible is desidered,

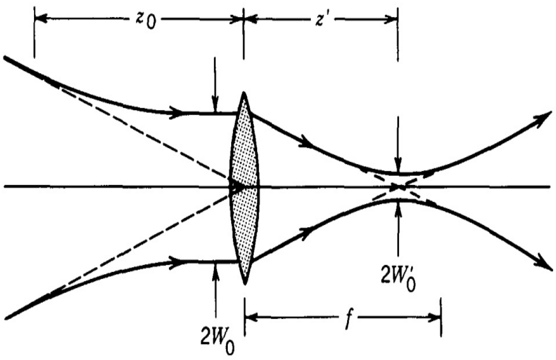

Figure A.2: *Schematic representation of the focusing of a gaussian beam at its beam waist.*

then the following relation has to be kept in mind

$$2W_0' \approx \frac{4}{\pi}\lambda F_*, \qquad F_* = \frac{f}{D} \tag{A.16}$$

and the lens with the proper F-number F_* has to be chosen.

Bibliography

[1] K. Buse. Appl. Phys. B 64, p.273 , 1997.

[2] K. Buse. Appl. Phys. B 64, p.391 , 1997.

[3] P. Günter and J.P.Huignard. *Photorefractive Materials and Their Application 1.* Springer, 2007.

[4] P. Günter and J.P.Huignard. *Photorefractive Materials and Their Application 2.* Springer, 2007.

[5] D. Kip. Appl. Phys. B 67, p.131, 1998.

[6] R.S. Wais and T.K. Gaylord. J. Chem. Phys. 59(12), p.6209, 1973.

[7] U. Schlarb and K. Betzler. Phys. Rev. B 48, 1993.

[8] M. Luennemann, U. Hartwig, G. Panotopoulos and K. Buse. Appl. Phys. B 76, p.403, 2003.

[9] R.S. Weis and T.K. Gaylord. Appl. Phys. A 37, p.191, 1985.

[10] A. Rauber. *Current Topics in Material Science 1.* 1978.

[11] E. Bernal, G. D. Chen and T.C. Lee. Phys. Lett. 21, p.259, 1966.

[12] D.N. Nikogosyan. *Nonlinear Optical Crystals: A Complete Survey.* Springer.

[13] P. Lerner, C. Legras and J.P. Dumas. J. Cryst. Growth 3, p.231, 1968.

[14] F. Abdi, M. D. Fontana, M. Aillerie and P. Bourson . Appl. Phys. A 83, p.427, 2006.

[15] H. Donnerberg, S.M. Tomlinson, C.R.A. Catlow and O.F. Schirmer. Phys. Rev. B 40, p.11909, 1989.

[16] O.F. Schirmer, S. Juppe and J. Koppitz. Crystal Lattice Defects and Amorphous Materials 16, p.353, 1987.

[17] T. Volk and M. Whölecke. *Lithium niobate. Defects, photorefraction and ferro- electric switching.* Springer, 2008.

[18] J. M. Cabrera, J. Olivares, M. Carrascosa, J. Rams, R. Mller, and E. Diguez. , Advances in Physics 45(5), p.349, 1996.

[19] M.V. Ciampolillo. *Diffusion of iron in lithium niobate for application in integrated optical device.* Ph.D. Thesis, 2010.

[20] M.G. Clark, F.J. Di Salvo, A.M. Glass and G.E. Peterson. Appl. Phys. A 37, p.191, 1985.

[21] B. Dischler, J.R. Herrington, A. Rauber and H. Kurz. Solid State Communications 14, p.1233, 1974.

[22] D. Berben, K. Buse, S. Wevering, P. Herth, M. Imlau and Th. Woike. , J. Appl. Phys. 87, p.1034, 2000.

[23] M.V. Ciampolillo, A. Zaltron, M. Bazzan, N. Argiolas and Cinzia Sada. , Applied Spectroscopy 65(2), p.216, 2010.

[24] M.N. Armenise, C. Canali, M. De Sario, A. Carnera, P. Mazzoldi and G. Celotti. IEEE Transactions on Components, Hybrids and Manufacturing Technology, chmt-5, p.212, 1982.

[25] M.A. McCoy, S.A. Dregia and W.E Lee. J. Mater. Res. 9, p.2040, 1994.

[26] R.S Roth and J.L Waring. The American Mineralogist 49, p.242, 1964.

[27] K.I. Gnanasekar, V. Jayarama, E. Prabhu, T. Gnanasekaran and G. Periaswami. Sensor and Actuators B 55, p.170, 1998.

[28] T. Vitova, J. Hormes, M. Falk and K. Buse. Juornal of applied Physics 105, 2009.

[29] T Gog, P. Schotters, J. Falta, G. Mterlik and M. Grodzicki. J. Phys.: Condens. Matter 7, p. 6971, 1995.

[30] L. Rebouta, M.F. Da Silva, J. C. Soares, M. Hage-Ali, J.P. Stoquert, P. Siffert, J.A. Sanz-García, E. Di*guêze* and F. Agulló-López. Sensor and Actuators B 55, p.170, 1998.

[31] J. F. Ziegler. Journal of Applied Physics 85 (3), p. 1249, 1999.

[32] C. R. Kroger. Nuclear Instrument Methods, B 136-138, p. 196, 1998.

[33] B.L. Henke, E.M. Gullikson, and J.C. Davis . Atomic Data and Nuclear Data Tables Vol. 54(2), p 181, 1993.

[34] L. Rebouta, P.J.M. Smulders, D.O. Boerma, F. Agulló-Lopez, M.F.da Silva and J.C. Soares. Physical Review B (Condensed Matter) 48, p. 3600, 1993.

[35] A. Ridah, P. Bourson, M. D. Fontana, and G. Malovichko. J. Phys.: Condens. Matter 9, p. 9867, 1997.

[36] S. Mignoni, M.D. Fontana, M. Bazzan, M.V. Ciampolillo, A. Zaltron, N. Argiolas and C. Sada. Appl Phys B 101 (3), p. 541, 2010.

[37] Y. Zhang, L. guilbert and P. Bourson. Appl Phys B 78, p. 355, 2004.

[38] A. Ashkin, G. D. Boyd, J. M. Dziedzic, R. G. Smith, A. A. Ballman, J. J. Levinstein, and K. Nassau. Applied Physics Letters 9, pp 72-74, 1966.

[39] F.S. Chen. Journal of Applied Physics 40, pp. 3389-3396, 1969.

[40] A.M. Glass, D. von der Linde, T. J. Negran. Applied Physics Letters 25, p. 233, 1974.

[41] J. Feinberg, D. Heiman, A. R. Tanguay, and R. W. Hellwarth. Journal of Applied Physics 51, pp. 1297-1305, 1980.

[42] V.L. Vinetskii and N.V. Kukhtarev. Sov. Phys. Solid State 16, p. 2414, 1975.

[43] K.Peithmann, A. Wiebrock and K. Buse. Applied Physics B 68, pp. 777-784, 1999.

[44] R. Orlowski and E. Kr*ä*tzing. Solid State Comm. 27, p. 1351, 1978.

[45] E. Kr*ä*tzing and R. Orlowski. Applied Physics 15, p. 133, 1978.

[46] D. Kip, J. Hukriede and E. Krätzing. Phys. Status Solidi A 168, R3, 1998.

[47] I. Nee, M. M*üller*, K. Buse and E. Kr*ä*tzing. Journal of Applied Physics 88 (7), p. 4282, 2000.

[48] J.R. Herrington, B. Bischler, A. R*ä*uber, J. Schneider. Solid State Commun. 12, p. 352, 1973.

[49] Y. Yang, I. Nee, K. Buse and D. Psaltis. Applied Physics Letters 78(26), p. 4076, 2001.

[50] N.V. Kukhtarev . Sov. Tech. Phys. Lett. 2, p. 438, 1976.

[51] N.V. Kukhtarev, V.B. Markov, S.G. Odulov, M.S. Soskin and V.L. Vinetskii. Ferroelectrics 22, p. 949, 1979.

[52] F. Jermann and J. Otten. J. Opt. Soc Am. B 10, p.2085, 1993.

[53] H. Kogelnik. Bell Syst. Tech. J. 48, p.2909, 1969.

[54] B. E. A. Saleh and M. C. Teich. *Fundamentals of Photonics.* Wiley-Interscienze, 2007.

[55] K. Peithmann, A. Wiebrock, K. Buse and E. Krätzig. J. Opt. Soc. Am. B 17, p.586, 2000.

[56] O. Althoff, A. Erdmann, L. Wiskott and P. Hertel. Phys. Stat. Sol. A 128, K41, 1991.

[57] F. Jermann, M. Simon and E. Krätzig. J. Opt. Soc. Am. B 12, p. 2066, 1995.

[58] M. Kösters, C. Becher, D. Haertle, B. Sturman and K. Buse. Appl. Phys. B 97, p. 811, 2009.

[59] O. Althoff and E. Krätzig. SPIE vol. 1273 Nonlinear Optical Materials III, 1990.

[60] L. Arizmendi, E.M. deMiguel-Sanz, M. Carrascosa. Opt. Lett. 23, p.960, 1998.

[61] J.J. Amodei, D.L. Staebler. Appl. Phys. Lett. 18, p.540, 1971.